UNIVERSITÀ DEGLI STUDI DELLA TUSCIA DI VITERBO

DIPARTIMENTO DI SCIENZE DELL'AMBIENTE FORESTALE E DELLE SUE RISORSE

CORSO DI DOTTORATO DI RICERCA IN
ECOLOGIA FORESTALE - XIX CICLO

A NOVEL APPROACH TO STUDY THE DYNAMICS OF MINERAL DUST EMISSION FROM THE GOBI DESERT OF NORTHERN CHINA BY EDDY COVARIANCE AND TO EVALUATE THE IMPACT OF VEGETATION IN MITIGATING DESERTIFICATION PROCESSES

AGR-05

UNA NUOVA METODOLOGIA PER LO STUDIO DELLE DINAMICHE DI EMISSIONE DI POLVERI MINERALI DAL DESERTO DEL GOBI (CINA SETTENTRIONALE) MEDIANTE *EDDY COVARIANCE* E PER LA VALUTAZIONE DELL'IMPATTO DELLA VEGETAZIONE NELLA MITIGAZIONE DEI PROCESSI DI DESERTIFICAZIONE

coordinatore: prof. Paolo De Angelis
firma

tutori: prof. Riccardo Valentini
firma

dr. Paolo Ciccioli
firma

dottorando: Gerardo Fratini
firma

ABSTRACT

In this thesis we address a new methodology for studying wind erosion, with particular reference to the development of a new instrumentation for measuring dust emissions. The instrumentation, called EOLO and based on the eddy covariance approach, was optimized for measuring vertical fluxes of mineral dust during intense erosion events and specifically designed to serve as a model validation tool. The system makes use of a 3D sonic anemometer and of an optical particle counter and provides size-segregated number fluxes on a 30-minutes base. Surface, volume and mass fluxes are also estimated.

EOLO was firstly applied in two monitoring campaigns in Northern China, in the framework of the WinDust project. It has been used to evaluate emission fluxes during a dust storm in the Gobi desert, and to investigate the relation between such fluxes and friction velocity. The effects of natural vegetation on the emissions during this event is addressed and analyzed; results are also compared with simulations from a wind erosion model. Although limited by the number of events recorded, results obtained provide useful information to parameterize the emission process during both dust storms and intense emission events.

EOLO has been also used to evaluate the potentialities of emission reduction of mitigation interventions, such as large scale, air-sowing reforestation and field scale implementations of conservative agricultural practice. First results show that reductions can vary from 40% in the case of conservative agriculture, to 99% in the case of air-sowing. However, further research is needed to assess the quality of the measurements, to quantify biases and uncertainties related to the measuring chain and to strengthen reliability of results.

RIASSUNTO

In questa tesi viene presentata una nuova metodologia per lo studio dell'erosione eolica. In particolare l'attenzione è focalizzata sullo sviluppo di uno strumento per la misura di flussi di particolato minerale a seguito di erosione. Lo strumento, ottimizzato per misurare in condizioni di intesa emissione, è stato progettato con lo scopo di fornire uno strumento di riferimento per la validazione di modelli di erosione eolica.

Lo strumento, chiamato EOLO e basato sulla teoria dell'*eddy covariance*, fa uso di un anemometro sonico e di un contatore ottico di particolato, dando in uscita i flussi di particolato, in termini di numero, superficie, volume e massa.

EOLO è stato utilizzato per la prima volta in due campagne di monitoraggio nella Cina Settentrionale, nell'ambito del progetto WinDust. I risultati presentati riguardano i dati di emissione durante una tempesta di sabbia verificatasi nel deserto del Gobi. Questi dati sono stati utilizzati per valutare la dipendenza delle emissioni da alcuni parametri chiave, quali la velocità di frizione, la direzione del vento rispetto alla vegetazione e l'umidità. Gli stessi dati sono stati utilizzati per la valutazione critica di un modello di erosione eolica, contribuendo ad evidenziarne le potenzialità descrittive e i punti deboli nella schematizzazione della fisica del problema.

EOLO è stato poi utilizzato per stimare la riduzione delle emissioni a seguito di interventi di mitigazione, quali riforestazione con semina da aereo in aree desertiche e l'implementazione di tecniche di agricoltura conservativa. I primi risultati delineando riduzioni che vanno dal 40% nel caso dell'agricoltura conservativa fino a 99% nel caso della semina da aereo.

Linee di sviluppo future riguardano soprattutto l'ottimizzazione del sistema in termini di qualità del campionamento e degli errori di misura, nonché l'estensione allo studio dei flussi di particolato di origine non eolica.

TABLE OF CONTENTS

1
INTRODUCTION

1.1 Desertification and wind erosion

Desertification may be considered as "*the ultimate step of land degradation, the point when land becomes irreversibly sterile in human terms and with respect to reasonable economic limitations*" (UNCOD, 1978). Specific desertification descriptors include: deterioration and impoverishment of ecosystems, degradation of vegetation, destruction of biological potential, intensification of desert conditions (Dunjo Denti (2004) and references therein). Historical evidences during the last few centuries show three main epicentres of desertification: the Mediterranean region, Mesopotamia and the semi-arid areas of northern China (Dregne, 1976). Today, about 1.9 billions hectares of land worldwide are affected by desertification at various degrees, affecting livelihood to more than 900 million people in some 100 countries (El Beltagy, 2000). Main desertification processes include (FAO, 1984): soil erosion by wind and water, soil degradation via chemical, physical and biological impoverishment, degradation of the vegetative cover in terms of mechanic and biological properties, and impoverishment of the landscape functions of soils, the most important being the hydrologic balance (Lal, 1990). Some general classes of causes of desertification can be identified, that are relevant on a global scale. We can broadly distinguish between direct and indirect causes. Within the first group, we can further distinguish between natural causes, such as climatic conditions, natural hazards, soil conditions, vegetation cover, and anthropogenic causes, e.g. overgrazing, inappropriate agricultural practices, deforestation, fires, industrial activities and urban expansion. On the other hand, indirect causes are mainly human-induced: land use patterns and changes, population increase, tourism activities etc. (Lal, 1990). Climate change, both natural and human-driven, is also accounted as a major cause of desertification.

In this thesis we focus on wind erosion, ranked as the main process of desertification (El Beltagy, 2000; Lal, 2001). Semi-arid and arid lands are obviously more susceptible to the wind action because soils tend to be dry, poorly structured and sparsely covered by vegetation (Middleton and Thomas, 1997). Low and unreliable rainfall in these regions are inadequate to sustain a stable and protective land cover. It has been recognized (Mainguet and Da Silva, 1998) that wind erosion assumes threatening proportions especially in those regions that are subject to intense human disturbances. Wind erosion interacts with other desertification processes such as degradation of vegetation and biophysical degradation of soil (Poesen and Nearing, 1993). Anthropogenic activities expose and disrupt the topsoil, enhancing dust emissions from the surface (Tegen and Fung, 1994). As the soil is disturbed, organic matter is reduced (eventually dropping to irreversibly low values), aggregates become less stable and hence the soil more susceptible to wind erosion (Dunjo Denti, 2004). As erosion of a soil occurs, it is often chemically degraded because of selective removal of organic matter and changes in accompanying soil chemical factors (Nicholson et al., 2000).

A spectacular manifestation of wind erosion is observed during dust and sand storms. These extreme meteorological events originate at the fringes of the largest desert areas of the world and are characterized by huge amounts of high-concentration sand/dust particles transported at high speed by winds. Sand and dusts plague lands, burying agricultural and rangelands as well as water courses, thereby enhancing desertification, particularly in lands already threaten by intense human activities. On the local scale, a major problem is related to the dune shifting, that can lead to a displacement of several meters per day. Dunes invade roads, threat buildings and infrastructures, and cover entire vegetated and croplands, thereby further enhancing desertification.

Another mechanism of desertification caused by wind erosion is related to the atmospheric physics. Indeed, dust entrained in the atmosphere tends to suppress or delay precipitations (Rosenfeld, 2000; Rosenfeld et al., 2001). It returns in lower precipitations and intensified droughts in the areas subject to wind erosion - another desertification factor - and intensified rainfall in regions already prone to floods and heavy rains. Although this indirect effect of wind erosion is not well-known yet, it is believed to play a major role in the desertification process.

Among the strategies to combat wind erosion and desertification, those implying the use of vegetation are perhaps the most widely used. Shelterbelts are often used at the paddock scale to protect agricultural sites from the direct action of the wind; trees and shrubs are

also used to inhibit dune shifting and sand-seas encroachment. On larger scales, afforestation/reforestation programmes in arid and semi-arid regions can provide a sufficiently homogeneous and dense soil coverage to inhibit wind erosion. Promotion of re-establishment of natural vegetation is often attempted by limiting over-grazing and wood overexploitation by local populations, eventually introducing alterative energies (renewable energies), suitable agricultural practices and alternative source of income. Conservative agricultural practices (such as limited or no-tillage) can limit soil erodibility by avoiding its disruption and maximizing soil cover by non-erodible elements (crop residues, mulching, etc.).

Although there are general evidences that mitigation interventions implying the use of vegetation can help limiting the human causes of desertification and wind erosion acceleration, a quantification of such effects, and of their cost-effectiveness, has seldom being attempted. Moreover, Institutions and researchers dealing with air quality and long-range dust transport acknowledge the lack of reliable data about actual emissions of dusts by wind erosion (Shao, 2000).

1.2 Aim and specific objectives of the thesis

In this framework, the main aim of our work was to develop a methodology to quantify dust emission during intense wind erosion events and dust storms, both in natural (desert) and human-driven (agricultural) environments. It also aimed at assessing the effects of mitigation interventions in terms of dust emission reduction. The overall idea is to develop a system for direct measurements of dust fluxes at the field scale, independent from any assumption about wind erosion physics, and to use it to evaluate and eventually tune a wind erosion model. The model can then be used to upscale measured dust fluxes at the larger scales. This thesis focuses on the measuring instrument, its development, validation and first applications to both desert lands and agricultural fields. A detailed comparison with a selected wind erosion model is addressed to discuss the effects of natural vegetation in the desert environment. The first achievements in assessing the effects on mitigation intervention are presented in the last sections of the thesis.

In Chapter 2 we review the role of mineral dust in the atmospheric physics, with emphasis on its potential role in enhancing desertification. We also provide a general introduction to wind erosion by a global perspective, as one of the main desertification mechanisms. Following, we focus on wind erosion and dust storms in Northern China, one of the most

relevant dust origin areas of the world and the one concerned in this thesis. In Chapter 3 we provide an overview of the theoretical and mathematical background underlying wind erosion processes; we review existing measuring instruments, highlighting the need for a new tool to study wind erosion. In Chapter 4, we address a new formulation of the eddy covariance technique developed within this thesis with the aim of application to heavy particle fluxes. Following, we describe the system developed to realize such measures, the selected wind erosion model and the monitoring campaigns carried out in the framework of the WinDust project. Chapter 5 is devoted to the presentation of first results obtained in the monitoring campaigns. We present dust fluxes during a dust storm in a Chinese desert and a detailed comparison with model results. This shows how direct measurements with EOLO can be used to detect lacks of parameterizations and to highlight the effects of physics that are seldom taken into due account. Chapter 5 also deals with some preliminary attempts to assess dust emission reduction due to mitigation interventions; in particular, it focuses on a large scale afforestation project and a small scale conservation tillage implementation. In Chapter 6 some conclusions are drawn; hints on further potential applications of EOLO both in the framework of wind erosion and in other research fields are also given in this Chapter.

2

ATMOSPHERIC DUST AND WIND EROSION: IMPACTS AND COUNTERMEASURES

2.1 Atmospheric dust: features, origin and climatic impacts

Particles relevant to atmospheric physics and chemistry may have diameter ranging between ~ 0.002 and ~ 100 μm. Aerosol particles, and in particular those of mineral dust, have been shown to present strongly varying shapes (Gillette and Walker, 1977). To overcome the difficulty of associating a size to a non-spherical particle, several *equivalent dimensions* have been introduced, with the aim of characterizing particles with respect to their physical behaviour. As far as wind erosion is concerned, one commonly used is the aerodynamic diameter, d_a, defined as the diameter of a sphere of unit density (1 g cm^{-3}) that has the same terminal falling velocity in air as the particle under consideration. Such diameter is related to the geometrical diameter d_g by the relation:

$$d_a \propto d_g \rho_p^{1/2} \tag{2.1}$$

where ρ_p is the particle density. This equivalent diameter is useful because it determines the residence time in air and reflects the various region of the respiratory system in which particles of different size deposit. The proportionality factor implied in Eq. (2.1) is called the *shape factor*. In the standard definition of particulate matter, diameters are intended as aerodynamic, i.e. PM_x is used to designate all particulate matter with aerodynamic diameter less than x μm. Other common equivalent diameters are the *Stokes diameter* and the *optical diameter*; the latter will be introduced and used later in this thesis.

Basing on number, surface and volume distributions, we can roughly identify three groups of particles in the atmosphere (Withby and Sverdrup, 1980): *i.* the *coarse range*, including particles with diameters ranging between 2.5 and 100 μm; *ii.* the *accumulation range*, with diameters in the range 0.08 to 1-2 μm; *iii.* the *Aitken nuclei range*, with diameters ranging

between 0.01 and 0.08 μm. The Aitken and the accumulation ranges together constitute the so-called *fine range*. Particles smaller than 0.01 μm are known as *ultrafine particles*. Mineral dust particles fall in the finer fraction of the *coarse range* and cover great part of the *accumulation range*. Figure 2.1 shows these groups and main interactions within and among the various groups.

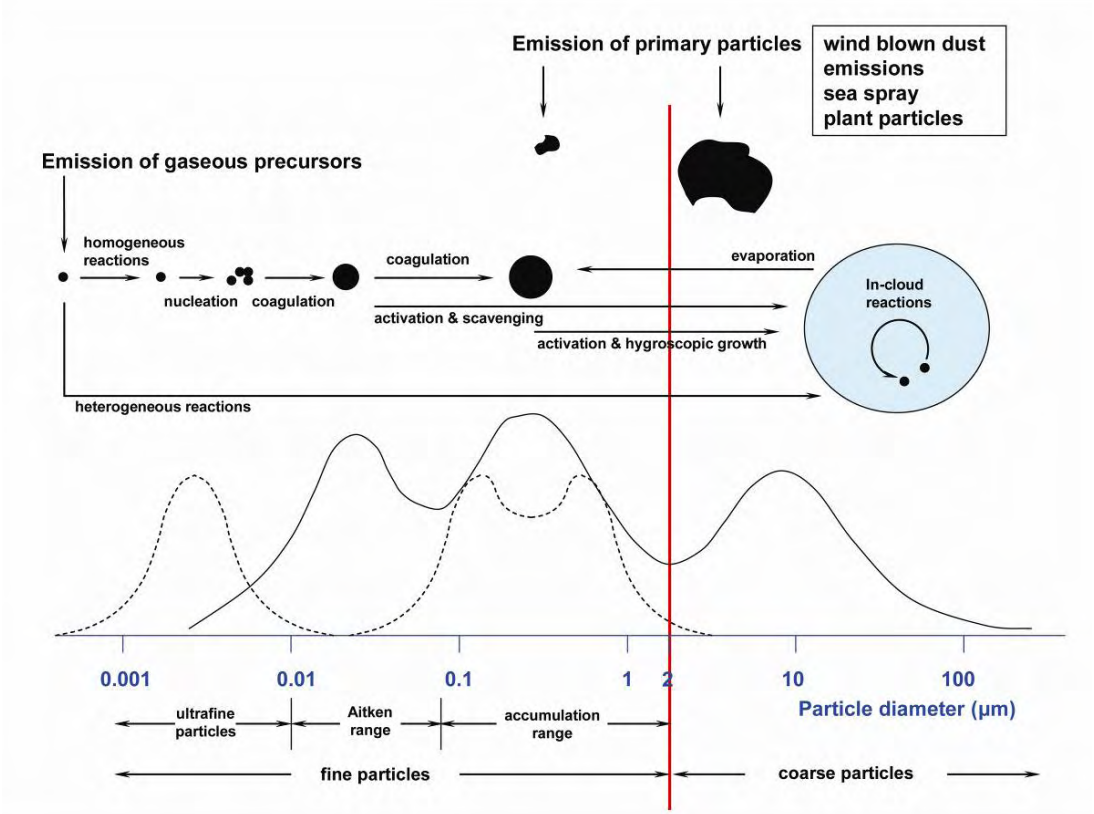

Figure 2.1. Atmospheric aerosol modes, main ranges, main mechanisms of formation and interactions (redrawn after Finlayson Pitts and Pitts (2000) and Heintzenberger et al. (2003))

Particles in the coarse range are produced mainly by mechanical processes, such as wind erosion. The largest portion of these particles tends to fall out quite quickly by sedimentation, but the smaller fraction (up to 10-20 μm), that also contains the bulk of its number concentration, can resident in the troposphere for long times (days), and be transported over very long distances (thousands of kilometres). Measurements of atmospheric particle size distributions made at distances of few hundred kilometres or more from the sources show that the mass median diameter rapidly shifts to sizes under 10 μm; over the oceans, where the mass median diameter is typically several micrometers (Duce, 1995). Coarser particles have also been observed to travel long distances (up to the regional scale), if strong convection conditions occur (Bonasoni et al., 2004; Dentener et al., 1996;

Duce, 1995; Prospero et al., 1981; Prospero and Nees, 1977; Zhang et al., 1997). Chemically, coarse particles include mostly silt, ultra-fine sand, pulverized coal and sea salt. Particles in the coarse range are generally thought to be only weakly correlated with smaller particles (Finlayson Pitts and Pitts, 2000). In this study we show that, during intense dust emission by wind erosion, number concentration of particles in the accumulation range dominates over coarse particles (Sect. 5.1.1), and that a clear increase also occurs for volume (and mass) concentration of such particles: the two ranges appear as strongly correlated. Particle in the accumulation range constitute a significant portion of the total aerosol mass (up to 50%). Due to their size, these particles can remain in the atmosphere for very long time also under usual conditions.

Particles in the Aitken range arise mainly from gas-to-particle conversion at ambient temperature as well as from combustion processes. These particles easily constitute condensation nuclei for low-volatility vapours. This range contains by far the larger portion of the number concentration of aerosol, and the smaller fraction of the mass concentration.

2.1.1 Natural and anthropogenic sources of atmospheric dust and other aerosols

Aerosol particles have a multitude of sources. They derive from primary sources, involving direct emission of particles, and from secondary processes, i.e. reactions of gaseous precursors in the atmosphere, to form particles (Heintzenberger et al., 2003). Some of the natural processes leading to particle production and the anthropogenic processes leading to changes in natural aerosol are summarized in Table 2.1.

species	Natural processes	anthropogenic processes	present-day particle burden compared to pre-industrial time	elements of climate change potentially affecting emissions
MINERAL DUST	wind erosion	Land use change, industrial dust emission	increased dust	changing winds and precipitations
SEA SALT	Wind	-	-	changing winds
BIOLOGICAL PARTICLES	wind, biochemical processes	agriculture	?	changing winds
CARBONACEOUS PARTICLES	vegetation fires	fossil fuel, biomass burning	increased carbonaceous particles	changing precipitation (droughts)
VOLATILE ORGANIC COMPOUNDS	emission from vegetation	increased oxidising capacity, industrial processes	increased organic aerosol	-

Table 2.1 Main aerosol classes: formation processes, trends at the present day and possible interaction with climate change (after Heintzenberger et al. (2003))

Soil dust and sea salt are by far the most relevant aerosol components in terms of mass load in the atmosphere. Globally, it is estimated that between 1000 and 3000 Tg/yr are emitted into the atmosphere, primarily in the Northern Hemisphere from the Sahara, the Arabian peninsula and Central Asia (Duce, 1995; Penner et al., 2001). Shao (2000) reports that the global mean column dust load is approximately 65 mg/m^2, more than 9 times that of the second-largest aerosol source, the sea salt (about 7 mg/m^2). Dust source regions are mainly deserts, dry lake beds, and semi-arid desert fringes, but also areas in drier regions where vegetation has been reduced or soil surfaces have been disturbed by human activities.

Major dust sources are found in the desert regions of the Northern Hemisphere, while dust emissions in the Southern Hemisphere are relatively small. It has been estimated that up to 50% of the current atmospheric dust load originates from disturbed soil surfaces, and should therefore be considered anthropogenic in origin (Tegen and Fung, 1995), but this estimate must be considered highly uncertain.

Mineral dust aerosols comprise mainly fine particles of crustal origin, advected from arid regions and consisting primarily of silica and silicate minerals. Zhang et al. (2003) showed that Asian aerosols are dominated by crustal elements entrained by wind erosion. Indeed, aerosol sampled during the intensive ACE-Asia experiment at several monitoring stations in northern China, were especially rich in Al, Ca, Fe, K, Mg, Mn, Si, and Ti, by far the major mineral dust elements. The percentage of Asian dust in the total suspended aerosol ranked between 45 and 82% for the monitoring stations of Northern China, including Beijing. Aerosol studies carried out over the past several decades have documented the temporal and spatial variability of dust transport over the oceans (Duce, 1995; Prospero, 1996a; Prospero, 1996b). Satellite imageries clearly show that dust aerosols often cover very large ocean areas. Dust plumes cover much larger areas, are more persistent, and occur more frequently than those associated with pollutant aerosols (Husar et al., 1997).

Sea salt aerosols are generated by various physical processes, especially the bursting of entrained air bubbles during whitecap formation (Blanchard, 1983). For the present-day climate, the total sea salt flux from ocean to atmosphere is estimated to be 3300 Tg/yr (Penner et al., 2001).

Emissions of primary anthropogenic aerosols such as industrial dust are estimated to range from about 100 Tg/yr (Andreae, 1995) to about 200 Tg/yr (Wolf and Hidy, 1997). These aerosol sources are responsible for the most conspicuous impact of anthropogenic aerosols on environmental quality, and have been widely monitored and regulated. As a result, their emissions have been reduced significantly, particularly in developed countries.

All together, carbonaceous aerosols (formed directly during biomass and fossil fuel burning and indirectly by atmospheric oxidation of biogenic and anthropogenic volatile organic compounds) and secondary aerosols from the atmospheric oxidation of hydrocarbons are estimated to contribute for about 90-380 Tg/yr (Andreae and Crutzen, 1997; Scholes and Andreae, 2000). This particles are mainly fund in the micron and sub-micron fractions.

2.1.2 Climatic impacts of atmospheric dust

Aerosol particles affect the climate system via the following physical mechanisms: firstly, they scatter and absorb solar radiation; secondly, they scatter, absorb and emit thermal radiation; thirdly, they act as cloud condensation nuclei (CCN) and ice nuclei (IN). The first two mechanisms are referred to as *direct effects*. The last one is referred to as *indirect effect*; other indirect effects are related to the influence on other atmospheric properties (e.g. semi-direct effect, suppression of convection).

Scattering and absorption of solar radiation by atmospheric aerosols exert a substantial influence on the Earth's radiation budget (Bates et al (2006) and references therein). By increasing aerosol and cloud optical depth, emissions of aerosols and their precursors cause a reduction of solar radiation at the surface ("solar dimming"). In order for the surface energy balance to reach a new equilibrium state, the surface energy budget has to adjust:

$$F_{sw} \approx F_{lw} + H + LE \tag{2.2}$$

where F_{sw} is the net shortwave radiation available at the surface, that has to be balanced by the net outgoing long-wave radiation (F_{lw}), the latent heat flux (H), the sensible heat flux (LE). The conductive flux from below the surface has been neglected here. As shown by model simulations by Feichter et al. (2004), the decrease in solar radiation at the surface resulting from the increases in aerosol optical depth may be more important for controlling the surface energy budget than the greenhouse gases-induced increase in surface temperature. The three components of the surface energy budget on the right-hand side of Eq. (2.2) decrease in response to the reduced input of solar radiation. As evaporation has to equal precipitation on the global scale, a reduction in the latent heat flux leads to a reduction in precipitation. Moreover, aerosols may change the occurrence and frequency of convection and thus could be responsible for droughts and flood simultaneously.

Indirect effects of aerosols on liquid water clouds are referred to as the cloud albedo effect, or Twomey effect (first indirect effect) and the cloud lifetime effect (second indirect effect). The Twomey effect refers to the enhanced reflection of solar radiation due to the more but smaller cloud droplets in a cloud whose liquid water content remains constant (Twomey,

1959). The IPCC Third Assessment Report concluded that the Twomey effect of anthropogenic aerosol particles amounts to 0 to -2 Wm^{-2} in the global mean (Ramaswamy et al., 2001). The more but smaller cloud droplets reduce precipitation efficiency and therefore enhance the cloud lifetime and hence the cloud reflectivity, which is referred to as the cloud lifetime effect (Albrecht, 1989). This effect is estimated to be roughly as large as the Twomey effect. Absorption of solar radiation by aerosols leads to a heating of the air, which can result in an evaporation of cloud droplets. It is referred to as semi-direct effect (Graßl, 1979; Hansen et al., 1997). The overall enhancement of clouds albedo, expected as the ultimate first effect of aerosols, can be traced by the correlation between clouds optical thickness and droplets effective radius. This correlation is negative, as anticipated by (Twomey, 1977) if only cases of comparable values of geometrical thickness are considered. On the other hand, if the most polluted cases are also accounted for, the trend suggests a positive correlation. Observations by Peng and co-workers (2002) did find the expected overall enhancement in cloud albedo in polluted clouds as compared to clean clouds by analyzing data taken from different Canadian field studies. In their dataset, the slope between optical thickness and effective radius is positive for polluted clouds due to the increase in liquid water content and absence of drizzle size drops and vice versa for clean clouds. Model estimates of indirect aerosol effects assessed the Twomey effect at the order of -1.3 Wm^{-2} (Lohmann and Feichter, 2004). Twomey effect has been estimated to be four times as important as the cloud lifetime effect by (Kristjansson, 2002), whereas Lohmann et al. (2000) simulated a cloud lifetime effect that is larger than the Twomey effect. Large uncertainties affect model results, that reflect large uncertainties in the parameterization of clouds physics and multi-phase interactions.

Generally, only anthropogenic pollutants and smoke were considered as cloud condensation nuclei (CCN), able to suppress precipitations by the formation of more but smaller droplets. Recently, aircraft and laboratory observations by Rosenfeld and co-workers (Rosenfeld, 2000; Rosenfeld et al., 2001) showed that also mineral dust can suppress precipitation. Saharan desert dust provides very large concentrations of CCN, mostly in the small size range. These lead to formation of clouds that are dominated by small droplets, leading to little coalescence and suppressed precipitation. Basing on this observations, they argued that the higher dust frequency is not necessarily a result of the decreased rainfall, but rather its cause. Due to the large spatial and temporal extent of desert dust in the atmosphere, the interactions of desert dust with clouds can have substantial climatic impacts.

Partially offsetting those negative effects in terms of desertification enhancement, dust-sized aerosol can have beneficial effects on mixed-phase clouds. If temperature in liquid water clouds is too warm for the homogeneous freezing to occur, ice formation requires aerosol surfaces to initiate. Aerosols can act as ice forming nuclei by coming into contact with super-cooled cloud droplets (contact freezing), or by initiating freezing from within a cloud droplet by immersion or condensation freezing, or by acting as deposition nuclei. Ice nuclei are generally insoluble particles, such as mineral dusts, soot, as well as some biological materials (Levin and Yankofsky, 1983). However, these processes are not yet well-known to predict their overall sign.

2.2 Wind erosion as a driver for atmospheric dust and desertification

The main mechanism of dust entrainment in the atmosphere is wind erosion. Wind erosion can give raise to several types of dust events. These have been classified by Goudie and Middleton (1992) as follows:

1) *Dust storms*, which are the result of strong turbulent wind systems entraining particles of dust into the air, so that the visibility is reduced to 1000 m and below.

2) *Dust haze*, which consists of aeolian dust particles homogenously suspended in the air. These are not actively entrained, but have been raised from the ground by a dust event that occurred prior to the time of observation or from a considerable distance. Visibility may sometimes be reduced to less than 10 000 m.

3) *Blowing dust*, which is the state where dust is raised above the ground locally through strong winds. The horizontal visibility may be reduced to 1000–10 000 m.

4) *Dust devils* or *dust whirls*, which are local, spatially limited, columns of dust that neither travel far nor last long.

Dust emitted by wind erosion has impacts that extend far beyond its climatic effects. It poses several risks to public utilities. Dust deposition blocks traffic, suspended dust reduces visibility, and dust-related air pollution causes health hazards (Lu, 2000). Many contaminants that pose significant risks to human health are found or associated with dust, including metals, pesticides, dioxins and radionuclide (Shao, 2000). In the short-range, intense wind erosion events, such as severe sand/dust storms, may threaten human lives and cause important economic damages (Dregne, 1995; Finlayson Pitts and Pitts, 2000), such as crop destruction by sandblasting.

Of course, wind erosion is a natural phenomenon; nonetheless, there are raising evidences that anthropogenic disturbances to the natural environment are leading to an increase of

wind erosion events and dust storms, in terms of intensity, frequency and affected areas. Clearance of natural vegetation, overgrazing, water over-exploitation and inadequate agricultural practices in semi-arid and arid regions increased wind erosion in many parts of the world. In human-disturbed regions, wind erosion rate can be many times that over natural environments. By this point of view, wind erosion and dust storms are a symptom of the desertification, but they are a cause of desertification as well. Indeed, sand transported at high speed by winds plagues the lands, burying agricultural and range-lands as well as water courses. During wind erosion, finer soil components are blown away; these comprise soil nutrients and organic matter. Thus, wind erosion leaves a coarse and less fertile soil behind. This results in enhancement of land degradation, in a positive-feedback desertification loop. An extraordinary example of such interaction between natural processes and anthropogenic disturbance was given by the dramatic increase in wind erosion registered during the 1930s in the Great Plains of the United States, known as the dust bowl. More recent examples are given by the quick desertification of Northern China (Inner Mongolia), that is to be related with the increase of agriculture in those regions and, often, with the sudden degradation and abandonment of huge areas. In Australia, recent dust storms originated in agricultural areas, where native vegetation has been cleared in the centuries (Shao, 2000).

2.2.1 Wind erosion by a global perspective

Although a comprehensive understanding of wind erosion at the global scale has not been reached yet, remotely sensed optical thickness, visibility analysis, meteorological observations and computational modelling helped sketching a picture of the most frequent, stable and intense wind erosion patterns. Large areas affected by wind erosion are present all over the globe and at all low and mid latitudes; nonetheless they are quite scattered geographically. This scattering is mainly concerned with the climatic patterns at the global scale.

Wind erosion can occur both in natural deserts and in human-disturbed lands. However, disturbed lands subject to wind erosion are only those found in arid and semi-arid regions. Here, human-induced effects can be direct, such as human over-exploitation of natural vegetation and poor agricultural practices, or indirect through climate change as is the case, for instance, with the Sahelian region (Shao, 2000). Great part of the drylands are found in the subtropical region (20°-30° N and S), with the notable exception of the arid regions of Northwest China, that extend around 40° N. Overall, drylands occupy ca. 60.9 millions of square kilometres (about one third of the Earth’s land surface), with about 6.6% being

classified as hyper-arid, 15.7% as arid and 22.6% as semi-arid and 12.8% as dry sub-humid (Safriel et al., 2000). Deserts dominate hyper-arid and arid regions, while main broad biome in semi-arid regions are grasslands. The latter are homelands to some 2 billions of people (35% of the world population), experiencing living standards far behind the rest of the world (Safriel et al., 2000). Most part of the sand seas are found in hyper-arid regions with precipitation seldom beyond 150 mm/yr.

Wind erosion over disturbed soils can be much stronger than over natural surfaces. This is because freshly disrupted soil contains far more erodible particles than natural soils, where erodible particles are likely to have been already removed; furthermore, mechanically loosed soils need lower threshold wind speed to initiate the erosion process. By means of model calculations, Tegen and Fung (1994) showed that 30 to 50% of the total dust emission may derive from erosion of disturbed soil surfaces. The risk of wind erosion is maximum in the semi-arid regions at the fringes of the deserts (Figure 2.2), where increasing human activities lead to land degradation and increased susceptibility. The percentage of total area subject to potential wind erosion vary across the continents, spamming from 14.5% in Europe to 69% in Oceania (Shao, 2000).

2.2.2 Environmental characterization of dust sources

In their work, Prospero and co-workers (2002) using TOMS (Total Ozone Mapping Spectrometer) products and by means of an *ad hoc* aerosol index, were able to identify what they called the “global dust belt”, a region of stable dust emission that extend from North Africa, through Middle East into Central Asia and China. Other areas considered to be stable dust sources have been detected in Australia, Western and South-Eastern US and South America. Most emissions are registered during winter and spring, autumn being the season of minimum dust activity. In Asia, dust activity peaks in spring. Data show that the most active dust sources are associated with topographic lows or they are situated in close proximity to mountains and highlands (Prospero et al., 2002). In mountainous regions (e.g., Afghanistan, Iran, Pakistan, and China), strong dust sources are often found in closed intermountain basins. This suggests that weathering processes and runoff from the mountains play an important role in providing fine soil material that can be mobilized as dust.

Another major result of the work by Prospero et al. (2002), further confirmed by other researchers, is that there is no evidence that the major dune systems and sand seas are persistent sources of dust, although they may be important sources on a sporadic basis. The size of particles in sand dunes and sand seas is on the order of tens to several hundred

micrometers (Lancaster, 1995); particles of this size have a very high settling velocity in air and, consequently, they will not be carried far by winds.

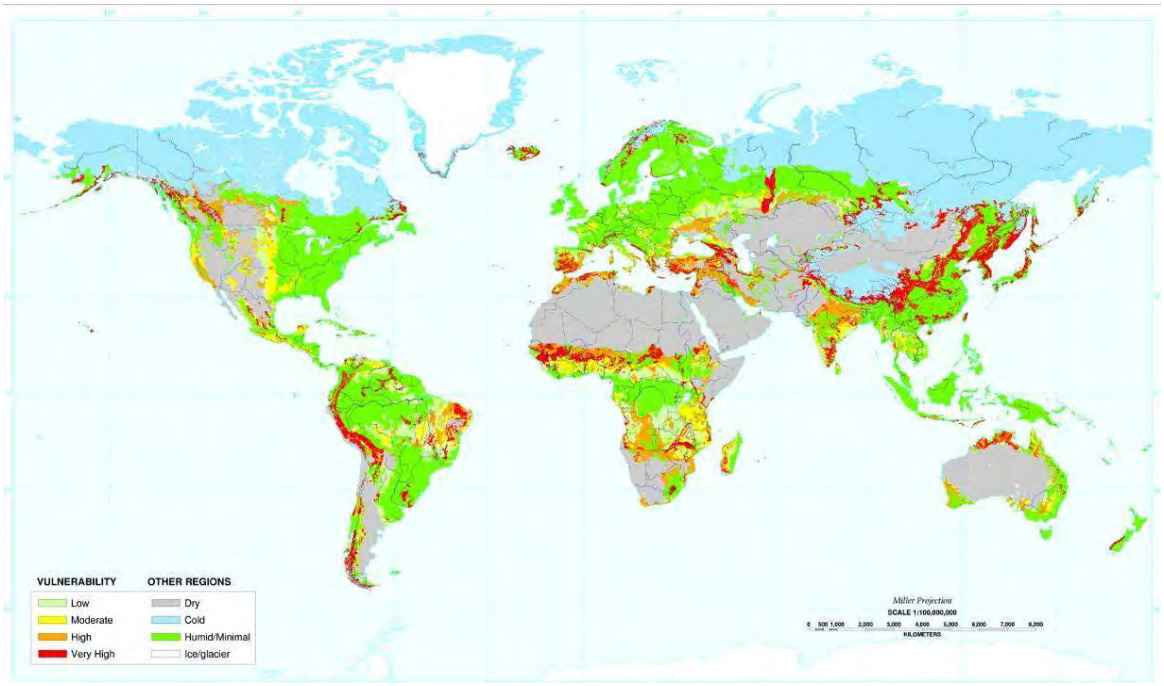

Figure 2.2. World map of vulnerability to wind erosion

Although sand particles themselves cannot be transported great distances, they play an important role in the dust generation process. As we will extensively see in the following (Sect. 3.1.5), because of the aerodynamic properties of smooth, fine-grained soil surfaces, dust is not readily mobilized unless the soil surface is disrupted (Gillette, 1999). Instead, the bombardment of the surface by wind-driven sand particles is a highly effective mechanism for grinding and shattering large particles into smaller particles and for ejecting fine particles into the atmosphere. Thus the juxtaposition of playas and fluvial deposits with sand sources may have the effect of enhancing the output of fine dust particles.

It has been further noted that many of the intense sources are associated with regions where there are extensive alluvial deposits (Middleton et al., 1986; Pye, 1989; Reheis and Kihl, 1995). Through fluvial action, small particles are separated from the soil and rock matrix and carried to depositional basins or alluvial plains where, after drying, they are subject to deflation by wind. Many of the most active sources were flooded during the Pleistocene. The prime example is the Lake Chad Basin, the largest source of long-range dust in North Africa. As we will see in Chapter 5, the most western area of Inner Mongolia (China), that represents one of the strongest dust sources in central Asia, is the result of an ancient

alluvial basin. In Oman, present-day fluvial action seems to play a major role in providing dust source material. Similarly, the Tarim Basin in Xinjiang (China) receives considerable run off from the surrounding mountains; as a result, the basin floor is covered with a several hundred meters thick layer of alluvial deposits. This further suggests that an important consideration with regard to precipitation is not only the amounts received in the source area itself but also the amounts received on the surrounding highlands where rainfall could be much greater. Example are the runoff from the Tibesti and Ahaggar mountains in central North Africa, and runoff from the Himalayas and the Tian Shan into the Tarim Basin (Prospero et al. 2002).

As far as the precipitation in the very source area is considered, larger source regions are arid: the Great Basin in the United States receives 120 mm or less annually; the Great Artesian Basin in Australia (Lake Eyre Basin) receives 125 mm; the Tarim Basin receives 50–100 mm; and Patagonia receives 100–180 mm. The relationship between dust activity and rainfall is most clearly demonstrated by the distribution of dust sources in North Africa; the southern boundary of these sources closely matches the 200–250 mm isohyets. Goudie (1983), in his study of global dust sources, noted that dust storm frequency peaks in areas where annual rainfall is between 100 and 200 mm. TOMS products show that the upper limit of large-scale sources is 200–250 mm. In Central-North Africa the board of the emissive areas also closely follows the 200–250 mm isohyets of rainfall (Mortimore, 1998). This is observed to be true in many parts of the world, in a broad regional sense: we should not expect to see strong dust sources in regions where rainfall is above 200–250 mm. The association of the dust source boundary with the 200–250 mm isohyets is also consistent with the occurrence of vegetation coverage as measured by satellite-derived vegetation indices (Nicholson et al., 1998), which suggests that higher rainfall amounts enable the growth of vegetation that stabilizes soils against deflation (Marticorena et al., 1997).

2.3 Mitigation interventions from field to regional scale

Among the strategies developed to combat wind erosion and to mitigate the effects on dust storms, those implying vegetation are perhaps the most commonly used, because of their efficiency and cost-effectiveness. Figure 2.3a shows schematically how vegetation can act as to mitigate wind erosion. It absorbs momentum and reduces the wind stress (proportional to the wind profile gradient) at the ground, thereby reducing wind *erosivity*. Shrubs or trees also provide a wake area downwind, with approximately null mean velocity; this “shelterbelt” effect can inhibit erosion for a distance that is 5-20 times the height of the

plants. There are several multipurpose trees which are useful for establishing shelterbelts; among others, *Robinia, Caragana, Tamarix, Populus, Salix and Acacia* spp. Lal (2001) highlights how ground cover in drylands comprises two well-defined zones: the area under the shrub and the inter-shrub, without any vegetative cover. He concludes that vegetative cover leads to diminished soil erodibility under the shrubs with respect to bare inter-shrub areas. Indeed, the bare inter-shrub area is characterized with sealed surfaces that are quite impermeable and absorb very little rain. In contrast, soil under vegetated cover is generally more porous, more organically rich, with a high infiltration rate.

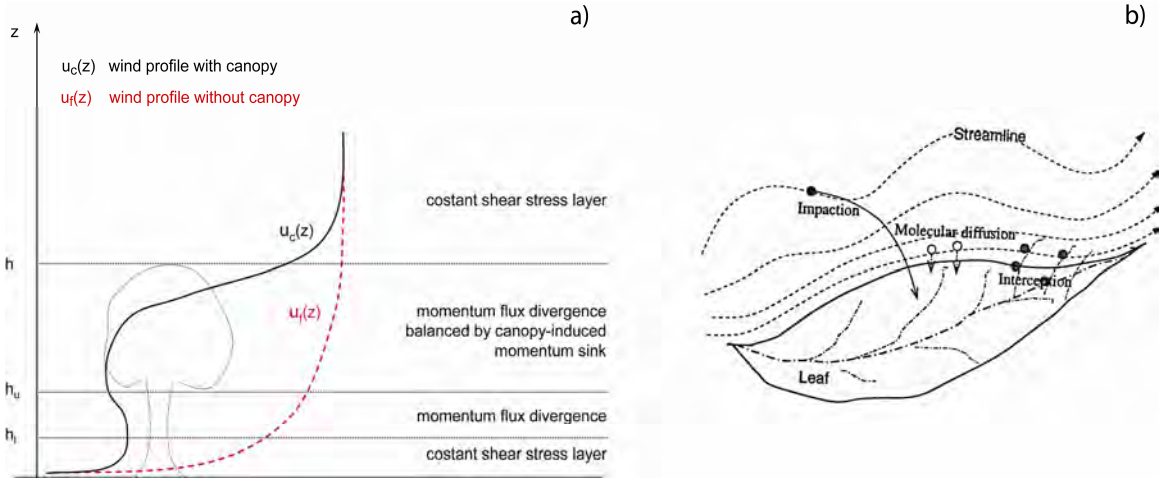

Figure 2.3. a) Wind profile close to the Earth surface in absence (red dashed line) and presence (black solid line) of a canopy. Also shown are the sub-layers that emerge above and below the canopy due to the presence of vegetation. b) mechanisms of particle deposition over leaves (adapter from Shao, 2000)

Vegetation provides a surface where dust can deposit. Hence, in vegetation rich areas, part of the emitted particles deposit quickly and do not contribute to the overall emission fluxes. Particles mainly deposit on the leaves via direct impaction, molecular diffusion and interception (Figure 2.3b). In particular, dust-sized particles tend to be captured by interception, occurring mainly due to trapping by the fine hairs on vegetation elements or to electrostatic forces (Shao, 2000).

Widespread deforestation for fuel wood and other domestic uses accentuates the impact of harsh dry environments. Deforestation for fuel wood has led to denudation of landscape and exacerbated risks of erosion and desertification (Boahene, 1998). Therefore, afforestation is an important strategy to restore vegetative cover, restore degraded ecosystems and grow household fuel. There are several multi-purpose trees which can grow under the harsh environments of drylands, protect the soil from erosion, improve soil quality (albeit slowly) and produce fuel wood. Some promising species for fuel wood production, soil quality

improvement and desertification control include *Tamarix, Eucalyptus, Leucaena, Cupressus, Casuarina, Capparis, Prosopis, Azadirachta, Acacia, Tectona, Cassia, Dalbergia, Khaya, Albizia, Parkia, Terminalia, Pongamia, Sesbania, Morus* and *Populus.* The most impressive example of afforestation to combat wind erosion and desertification is probably the 3N (Northeast, North, Northwest) Shelterbelt project – also known as the Great Green Wall – established in China since 1978 and lasting some 73 years until 2050. Wang and Zhou (2003) showed that the benefits of such a large afforestation intervention go beyond the direct inhibition of wind and water erosion, increasing precipitations and humidity and reducing wind speed in the arid and semi-arid regions concerned.

Excessive stocking rates and uncontrolled grazing are important factors that accentuate risks of desertification by wind erosion. In semi-arid regions of northern China, overgrazing is considered one of the primary causes of desertification, both increasing surface albedo and reducing surface roughness, thereby increasing soil erodibility (Sheng et al., 2000). In the Horqin sandy grassland of northern China, Su et al. (2005) observed that continuous grazing and livestock exclusion can lead to improved soil properties and reduced erodibility in 5-10 years. They address these practices as an alternative to afforestation intervention to restore natural vegetation in that area. In the Kalahari Desert, Wiggs et al. (1994) observed that denudation by over-grazing, burning or drought led to a 3-fold increase in dune movement and wind erosion.

In their experiments at the Texas Experimental Ranch, Pluhar et al. (1987) observed that water infiltration capacity increased as vegetal cover increased, soil bulk density decreased, and soil organic matter content increased. Grazing caused a significant decline in infiltration capacity by reducing the protective vegetal cover and increasing the surface area of the bare ground.

Decreasing water losses by runoff and evaporation is critical to reduce soil erodibility. Beneficial effects of establishing stone bunds on the contour in decreasing losses by runoff have been documented in sub-Saharan Africa and in Algeria by the use of appropriate crop rotations and sylvo-pastoral systems (Lal, 1990). Residue management and choice of appropriate tillage methods are also important to increase water use efficiency. Experiments in Niger reported that application of 2 Mg ha^{-1} of crop residue mulch decreased soil erosion by about 50% and that surface application of millet residue mulch at 2 Mg ha^{-1} significantly reduced wind erosion (Lal, 1990). An additional benefit of erosion control by mulching is decreased loss of water by runoff and evaporation. Residue mulch decreases soil temperature which contributes to a reduction in evaporation. Beneficial effects of crop

residue mulch on the soil quality of drylands have been reported from Burkina Faso, Niger, southern India and China (Lal, 1990; Li et al., 1994). Importance of crop rotations in reversing soil degradative trends is even more prominent in harsh arid and semi-arid environments than in humid eco-regions. Choice of an appropriate rotation is also critical to adoption of a conservation tillage system, whose effectiveness in soil and water conservation in arid and semi-arid regions depends on the amount of surface area covered by crop residue mulch.

According to researches carried out in several soil and climate conditions all around the world in the last decades, conservation tillage techniques, in particular no tillage (sod seeding) and ridge tillage (limited to large inter-row crops) have been shown to increase soil organic matter, increase soil water content and reduce water and wind erosion (Holland, 2004; Lo Cascio et al., 1997; Lo Cascio and Cereti, 1995).

2.4 Wind Erosion and dust storms in China

2.4.1 Location of dust storm source areas

Desert areas occupy about 13% of China's land surface and are ranked as the most intense sources of Asian dust (Liu, 1985). Deserts in China are found in the most inner regions of the Eurasian continent, that are far from large moisture sources. Atmospheric moisture transport by the Indian monsoon is prevented by the Himalayan chain. During winter, these regions are dominated by the Siberian high pressure system, that is extremely dry and cold. As a consequence of these factors, arid and hyper-arid regions of China are by far the largest at the temperate latitudes (Goudie and Middleton, 1992; Middleton, 1989). Strong winds here mobilize a lot of dust, that is carried easterly through China, Japan and Korea (Prospero et al., 2002; Zhang et al., 1997). Asian dust is routinely observed in relatively high concentrations at stations in the central North Pacific, and it has been occasionally detected over North America. Most of the dust storms in China occur during springs, with 30% to 50% of the yearly sum occurring in April (Liu, 1985). Dust storms in China are mainly caused by cold frontal systems breaking through the *East-Asian Through*, that is an upper-atmospheric layer of relatively stable warmer air. Typically, the cold fronts move southeast, behind which an high-pressure centre of cold air passes over the north part of the Tarim Basin system. Two low-pressure patterns, the 'Warm Low' over the Taklimakan Desert and the Mongolian Cyclonic Depression over the Mongolian Plateau, are often observed (Sun et al., 2001). Both kinds of low-level convergence lift up dust to a few kilometres so as to form the long distance transport of dust plumes.

Climatologically, there are four maximum axes of rainfall in far Northwest China (80°–90°E), the upper reaches of the Yellow and Yangtze Rivers (100°–105°E), East coastland (115°–120°E), and Northeast China, near 125°E for summer. Between them, relatively dry zones can be found in the desert region over Northwest China, the mid-reaches of the Yellow River, and the west part of Northeast China. These dry zones are the background not only to dust storm formation but also to dust transport at the long-range (Qian et al., 2002).

Data expressed in percent of observations

Terrain	Spring	Summer	Autumn	Winter
Around Taklimakan Desert	53,42	34,05	6,95	5,57
Hexi Corridor	53,64	26,45	5,05	14,86
West Inner Mongolia Plateau	50,74	24,52	6,60	18,15
Tibet Plateau	41,34	30,18	9,60	18,87
Northeast China	65,12	9,41	3,47	22,00
All other regions	52,97	25,60	6,23	15,20

Table 2.2. Seasonal changes of dust storm occurrences for several regions of China (redrawn from Wang et al. 2004)

Xinjiang, Inner Mongolia and Gansu, along with upper reach of the Yellow River are the regions most affected by wind erosion (Dong et al., 2000; Qian et al., 2002; Wang et al., 2004; Xuan et al., 2004). The highest frequency of dust storms was found by Qian and co-workers in the Tarim Basin and the second highest is located in the central-western part of Inner Mongolia (Prospero et al., 2002; Xuan et al., 2004; Zhang et al., 2003), that is mainly a ground surface of Gobi, alluvial and lacustrine sediments (see also Table 2.2). Gobi is widely present in central and western North China. The Gobi is a stony desert; as such, it is not normally expect to be a particularly strong source of dust (Dong et al., 2000) in comparison to the other sources. Nonetheless, the Gobi is clearly a major source: Xuan and co-workers (as quoted in Prospero et al. (2002)) suggest that the central Gobi is the second source in China, after the Taklimakan, in terms of emission intensity. SeaWiFS images of dust storms in the Gobi often show that large dust clouds are comprised of many well-defined plumes that emerge from “point” sources. These might have characteristics that differ from the Gobi at large. They could be topographical lows, or they could be areas of

the Gobi where the stony cover has been removed through human activities and agricultural development (Dong et al., 2000).

Indeed, there is evidence that wind erosion has increased in China over the past several decades, as a consequence of human impact. Dong et al. (2004) point out that many of the erosion centres are located on the Gobi desert and that "hardly any erosion occurs on the original deflation plane except when disturbed". They argue that much of the erosion in these regions is due to rapid population growth, land reclamation, and agricultural development. Later in this work, we will address the hypothesis that "natural" Gobi can be an important source of dust, under certain circumstances. These conditions, that include presence of sparse vegetation as punctual sinks of blowing sand, are widely common in large areas of the westernmost Alashan Gobi.

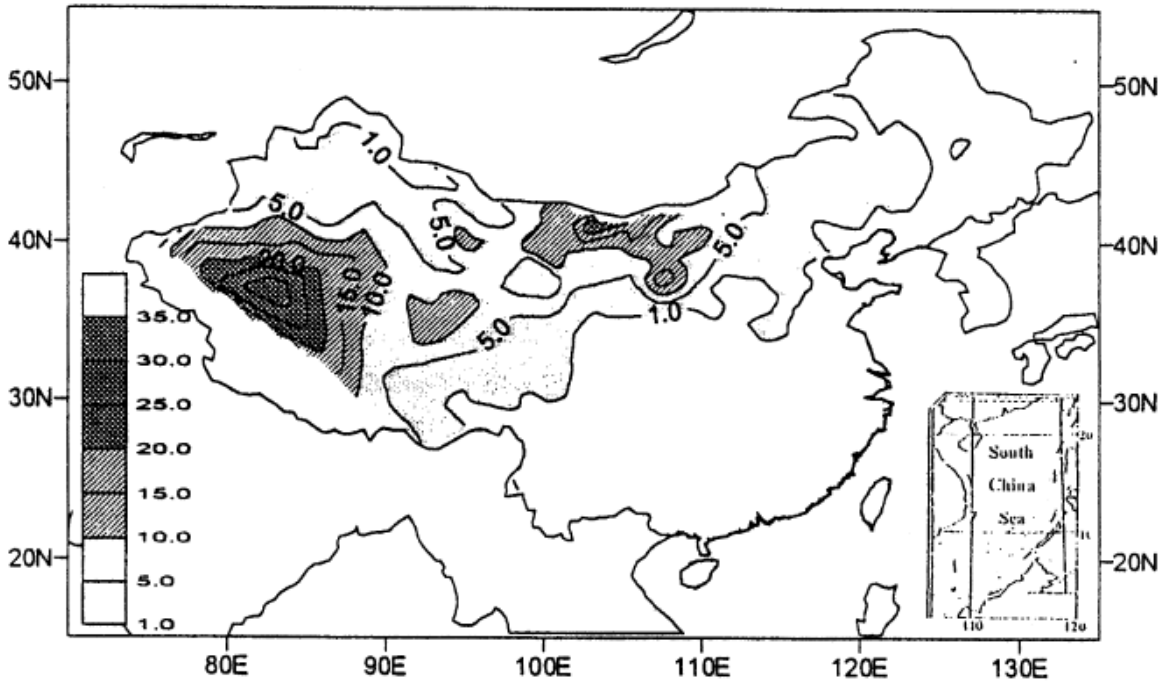

Figure 2.4. Yearly mean distributions (days) of dust storms averaged from 1954 to 1998. Dashed lines indicate the maximum of dust weather frequency (source: Qian et al. 2002)

Using the datasets of dust storms and dust weather from 338 stations for 1954–98, Qian et al. (2002) derived an yearly mean distribution of dust storms and dust weather as shown in Figure 2.4. The areas with more than one day of dust storms per year are located in Northwest China and North China, except Heilongjiang Province in the northeast. The high-frequency centre with more than 30 days of dust storm per year can be found in the Taklimakan desert region, while more than 15–20 days were registered in the central-

western Inner-Mongolia region (Alashan desert). Wang et al. (2004) detected the same two areas as the most plagued by wind erosion in China, but they acknowledge the Inner Mongolia Plateau as the most important in terms of far-reaching dust storms source, while storms raising in the Taklimakan are therein believed to have only local effects. Prospero et al. (2002) found that Tarim Basin is the most intense and persistent dust source in China.
In addition to these two main regions, Dong et al. (2000) identify three other regions, all located north of the Yellow River, as major dust sources, namely the Junggar Basin, the Northern Inner Mongolian Plateau and the Horqin Steppe on the Ordos plateau. Significant dust activity has been recorded over the Loess Plateau, which lies north of the Qin Ling Mountains and the Wei River (Zhang et al., 1997). The Loess Plateau is a huge area (30.000 km^2) covered with loess, a wind-deposited soil (Pye, 1987), whose depths range from typically 30–60 m to as much as 200m. The Loess Plateau has long been suggested as a major dust source. These soils are now susceptible to enhanced deflation because of the intense agricultural activity in this region (Dong et al., 2000).

2.4.2 Chinese programmes to combat desertification driven by wind erosion

Chinese Government has launched a series of 10 years lasting (2001-2010) forest ecological programmes aiming at improving ecological environment and combating desertification driven by wind and water erosion. Among those concerning with wind erosion, the *Desertification combating programme on the origin of sand and wind in Beijing and Tianjin Municipalities*, the *4th phase of the Three North shelterbelt programme*, the *Natural vegetation protection programme*, the *Grassland protection and management in the upper and middle reaches of the Yellow River*. These projects focus on Provinces, Municipalities and Autonomous Regions seriously affected by desertification and wind erosion of northern China, namely: Inner Mongolia, Xinjiang, Shanxi, Gansu, Qinghai, Ningxia, Hebei, Beijing Municipality. The strategies depicted in the projects include a fair number of countermeasures: protection of forest and grass vegetations, tree-planting, aerial seeding, development of farmland and grassland shelterbelt network by establishment of wind-breaking and sand-fixing shelterbelts; natural regeneration of grasslands, afforestation and grassland establishment on barren land and hills, seed and seedling bases construction, rodent and pest control, pasture land improvement and construction of water-saving and irrigation systems to facilitate implementation of the crop rotation, etc. (Tu et al., 2002).
In particular, *the 4th phase of the Three North shelterbelt programme* involves 590 counties of 13 provinces in the Northwest, North and Northeast China, of which 240 counties, with a total land area of 2.9225 million km^2, are seriously under the threat of wind erosion, taking

72% of the total programme area. The total wind-eroded land area included in the programme amounts to 1.3 million km^2. Main aim of the programme is to reverse the expansion of 8 big deserts in the provinces concerned and the degradation and die-out of natural *Populus diversifolia, Tamarix ramosissima.* and *Haloxylon ammodendron* in certain parts of west Alashan Plateau and the lower reaches of Talim River, as well as to rehabilitate forest stands to form a regional shelterbelt system so as to reduce windy and sandy weather and improve the eco-environment in these areas.

Popularization of conservation tillage (CT) in China has made dramatic achievements, and is under good circumstances to develop. In recent years, the Chinese Central Government, the State Council and the relative departments have paid much attention on conservation tillage development. CT was listed as a key work for speeding up the construction of economical society. In "The Determination of Further Strengthen the Combating Desertification by the State Council", CT was liaised as one of the major measures of combating desertification. By the end of 2005, the Agricultural Ministry of China had set up 100 CT project counties on national level and 251 CT demonstration counties on provincial level in 13 northern provinces and regions. The total demonstration area in the national level project counties are above 580,000ha, with 1.5 million farmers involved.

2.4.3 The WinDust project

Although a number of Programmes has been designed and are under development to fight against wind erosion and dust storms, a clear identification of the actual, major source areas of sand/dust storms and dust emission has not been reached yet, as widely recognized by the scientific community (Shao, 2000; Westphal et al., 1988). Quantification of dust emission during strong wind erosion events and quantification of the effects of mitigation efforts are even further achievements. Nonetheless, it is of major importance both in the assessment of the direct effects of wind erosion in terms of soil impoverishment and in the quantification of dust entrainment into the atmosphere.

With the aim of studying the origin and propose specific countermeasures against dust storms affecting Beijing, the Italian Ministry of Environment and Territory of Italian Government (IMET) and the Environmental Protection Bureau of Beijing Municipality (BMEPB) launched in 2004 the WinDust project. The project is part of the Sino-Italian cooperation program (www.sinoitaenvironment.org), established in 2000 among IMET, the State Environmental Protection Administration of China (SEPA), the Ministry of Science and Technology (MOST) of China, the Chinese Academy of Social Sciences (CASS) and Beijing and Shanghai Municipal Governments. Main aim of WinDust is to study the

desertification factors leading to the increase, in frequency and intensity, of the “dust events” over the Beijing Municipality and to propose a general action plan of intervention. To this end, the project focuses in the western Inner Mongolia Plateau (Alashan desert) and in the Beijing suburban areas as “remote” and “local” dust sources, respectively. The Alashan desert is considered one of the most important sources for both dust storms and Asian atmospheric dust (Sect. 2.4.1), although the exact location of dust sources is not yet known. Punctual sources in the surroundings of Beijing, tough not relevant on a global scale, are considered to be major causes of the dust load over the Capital.

Of course, estimating dust emissions on a regional (or global) scale is a task that involves modelling and GIS-oriented approaches. Nonetheless, dust emission starts at the field scale, thus it requires field scale models, that need to be evaluated against direct measurements before they can be used confidently. Accordingly, within WinDust the study of dust storms is addressed at different scales: direct measurements and modelling of wind erosion to quantify dust entrainment in the atmosphere, long-range dust transport modelling to assess the relative importance of “local” and “remote” sources of dust over Beijing and multi-temporal land cover analysis to detect the areas mainly subject to desertification and likely to become future dust sources. The overall goal is to create a model for the whole dust cycle, from the emission to the deposition, based on field measurements of actual emissions from most relevant sources. Specific objective of the project is also to implement and evaluate mitigation actions. To this aim, pilot projects of conservation tillage were implemented in agricultural areas of Beijing Municipality. WinDust also supported the continuation of the air-sowing reforestation activity within the 3N Shelterbelt Programme. Assessment of emission reduction due to these interventions would allow to simulate the overall reduction of the dust load over Beijing deriving from a large scale mitigation action plan.

In the framework of the WinDust project, our work was devoted to the development of a methodology to assess dust emission by wind erosion from natural and human-disturbed environments, and to quantify the emission reductions due to mitigation interventions. The methodology relies on a new technology developed to measure emission fluxes of mineral dust, that was used to evaluate and tune a wind erosion model, intended to upscale field measurements. The work presented in this thesis focuses on the development of the instrumentation, called EOLO. This is based on the eddy covariance approach. Here we establish the mathematical basis underlying its design and delineate its limits of

applicability. We present the first applications of EOLO within the WinDust project, and critically discuss the comparison with a wind erosion model. Finally, preliminary results concerning the assessment of emission reductions due to mitigation intervention are provided, as a work in progress, in the final part of the thesis.

3
WIND EROSION: BASIC CONCEPTS, MEASUREMENT AND MODELING

3.1 Basic concepts of wind erosion processes

3.1.1 The climatic background for wind erosion and dust storms

Winds in the free atmosphere are dominated by the Coriolis force and the pressure gradients (mainly resulting from the uneven distribution of the energy balance at the surface between high and low latitudes). These winds form the geostrophic current patterns. Close to the Earth surface winds are instead strongly influenced by friction with lands and oceans. Thus, the interaction of the free atmosphere climatic patterns, that present high levels of regularity, and the uneven distribution of the continents give rise to the scattered geographical locations of arid and semi-arid regions. The tropical, mid-latitude and polar circulations give rise to three wind belts in each hemisphere. This general circulation patterns has major implications of the distribution of precipitations, temperature and, hence, wind erosion (Shao, 2000). Wind erosion seasonal and super-seasonal patterns in Asia - notably India and China - are mostly dominated by the monsoon cycle. In particular, during spring and early summer, the summer monsoon that produces heavy rainfalls cannot penetrate within North and Northwest China, mainly because of the barrier constituted by the Tibet Plateau. This results in heavy drought periods in these regions. The strong surface winds accompanying the polar front travelling from NW to SE in that low-pressure mid-latitude region, can create suitable conditions for strong and frequent dust storms and diffuse wind erosion. Qian et al. (2002) highlighted the strong correlation of dust storms frequency in China with the occurrence of the Mongolian cyclone and acknowledged that the circumpolar vortex disturbances observed in Northern China (the Northeast China cyclone and the Yellow River cyclone), are important for dust storm activity in China.

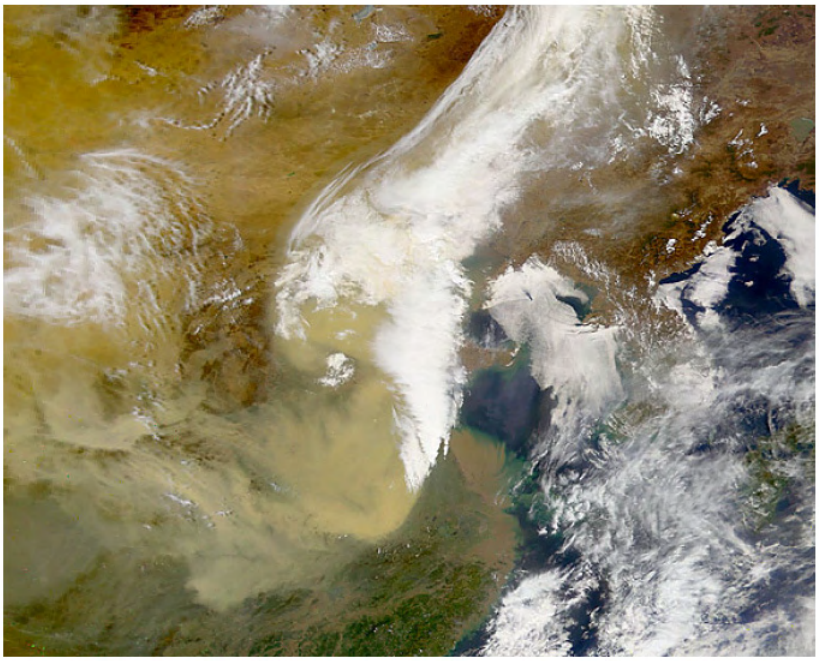

Figure 3.1. Satellite image of the dust storm originating in the Taklimakan desert of northwest China on 14 April 1998. The image, taken two days later, shows the dust clouds behind the cold front and near the centre of the Storm (SeaWiFS image produced by Norman Kuring, NASA GSFC)

Cold Fronts

Wind erosion can occur whenever intense winds insist on bare lands, both natural (deserts) or human-disturbed (rangelands, agricultural fields). However, formation of intense dust storms needs the simultaneous presence of several conditions, including: *i.* strong near surface winds, able to lift sand and dust materials; *ii.* strong convection to disperse particles deeply into the air; *iii.* strong winds to transport particles long distances horizontally; *iv.* atmospheric gravity currents to confine particles within the cooler air flowing under the warmer atmosphere. Strong horizontal winds can occur because of a gravity current. Gravity currents are horizontal flows of cool air that doesn't mix significantly with surrounding air. This cool air is denser than the surrounding, thus the winds tend to be horizontal and stable, flowing below a layer of warmer air. Figure 3.1 shows a cold front that generated a dust storm in Northwest China. Cold fronts consist of an advancing wedge of cooler air into the warmer air mass ahead. Propagation speed of the cold fronts can be as high as 15 ms^{-1} (Figure 3.2).

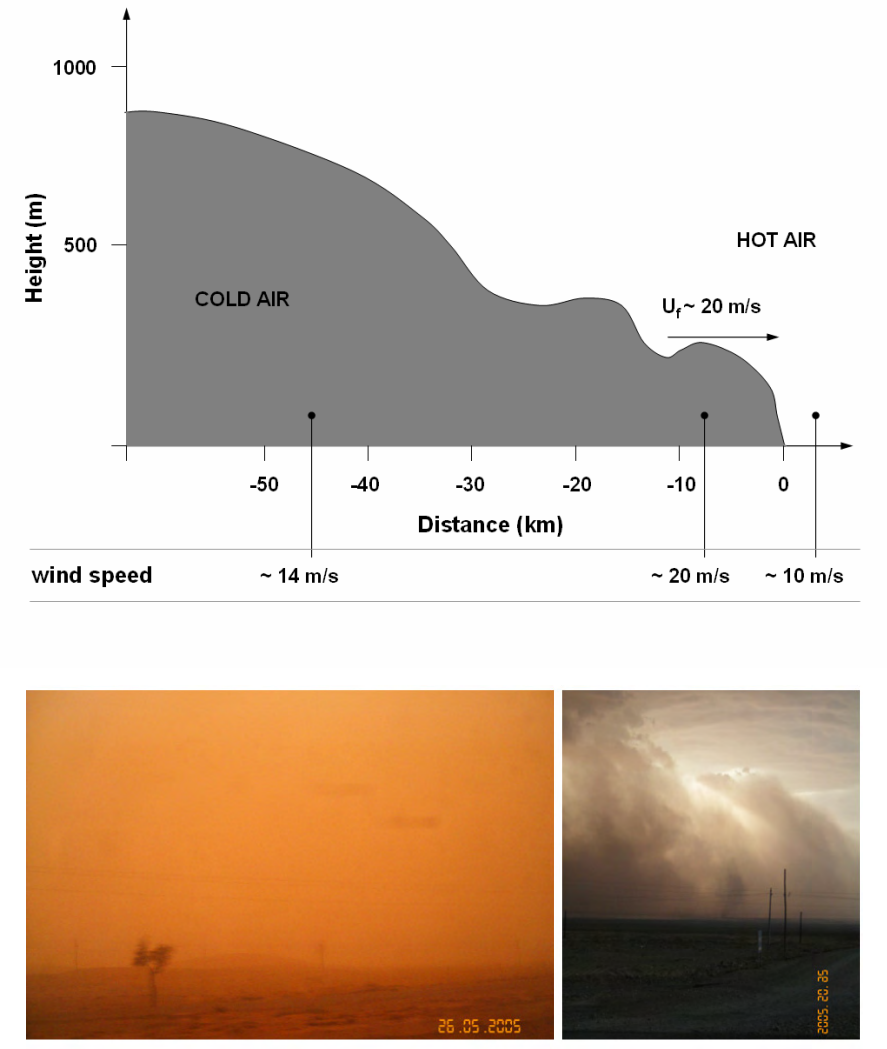

Figure 3.2. Transect through the cool change along an axis normal to the front showing the height of advancing wedge of cold (redrawn from Shao, 2000; photo: Sara Da Canal)

Winds at the sharp interface between cooler and warmer air can reach values of 20 ms^{-1} (Garrat, 1984; Garrat et al., 1989). The depth of the front can be as high as 300 m at the interface, reaching 1000 m in the rear part. If the cold front passes over an unprotected soil, it can cause strong dust emission and hence a dust storm. In these cases, the interface is marked by a spectacular wall of dust.

Squall lines

The formation of dust storms can also be due to strong convection events following atmospheric dynamic instability. With reference to Figure 3.3(top), warm air raises ahead of the storm, because of buoyancy effects. As it is uplifted, air is cooled beyond its condensation level, hence it produces heavy rains that follow the storm front. Air reaching the storm from the rear is cooled down by evaporation of droplets and is subject to a

downward movement. This air reaches the ground and is partially moved toward the storm front, generating very strong winds (squall lines) that can reach 50 ms^{-1}. These winds give raise to very intense and destroying wind erosion.

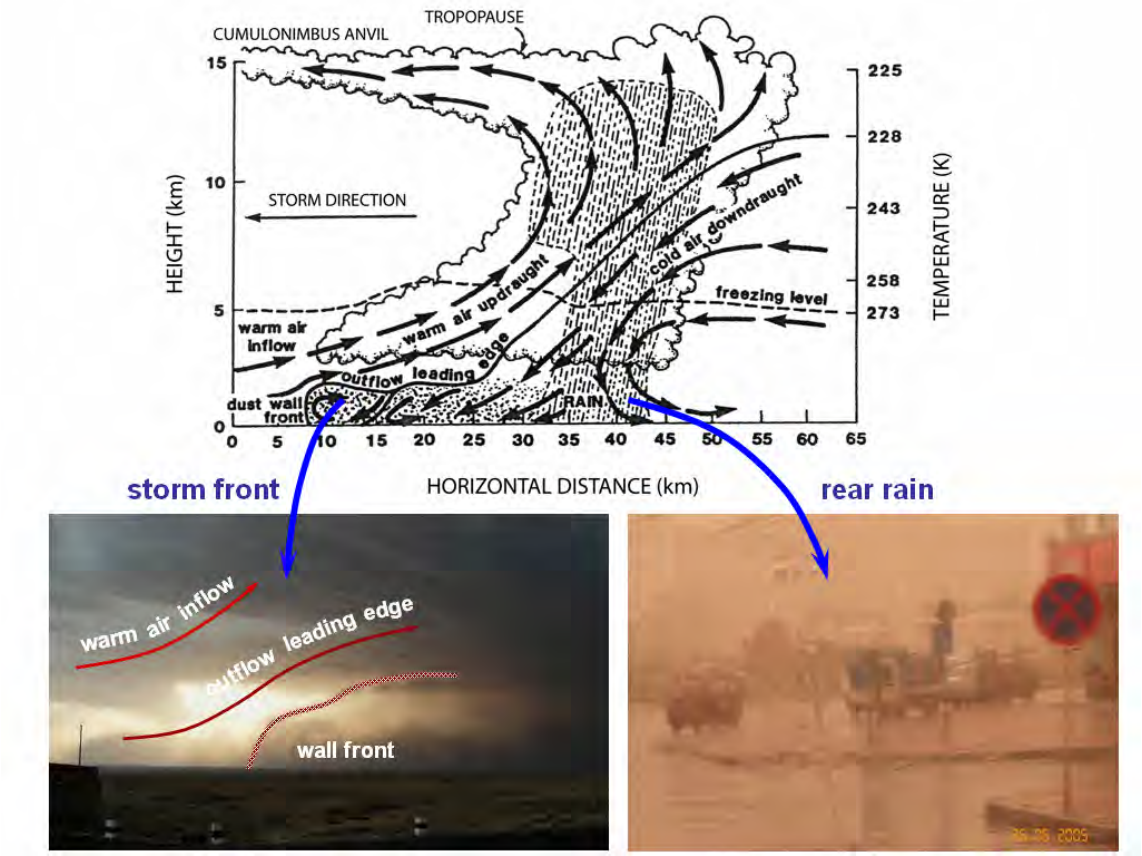

Figure 3.3. (top) Formation of a dust storm depicted in a thunderstorm structure. (bottom) Corresponding pictures taken during a dust storm in the Alashan desert during May 2005 (photo: Sara Da Canal)

This kind of sand/dust storms are short in duration (several hours) and relatively confined in space. Figure 3.3(bottom) shows the front of such a storm experienced during the field experiment in the Alashan region of Inner Mongolia (China), during May, 2005. The right-hand picture shows the heavy rain following the front of the storm.

3.1.2 Forces acting on an airborne particle

By a Lagrangian point of view, main forces acting on an airborne particle are the gravity force ($\boldsymbol{F_g}$), aerodynamic drag ($\boldsymbol{F_d}$), aerodynamic lift ($\boldsymbol{F_l}$) and the Magnus force due to particle rotation ($\boldsymbol{F_m}$); as vectors, forces are here indicated in bold characters. Buoyancy can be neglected for particles, hence $\boldsymbol{F_g}$ is only given by particle weight. The other forces are illustrated in Figure 3.4. Drag force $\boldsymbol{F_d}$ arises because a body immersed in a flow field

causes a pressure difference between the front and the wake regions, that in turn forces the body to move in the flow direction (Figure 3.4a). The total drug is given by the integral of the momentum transfer from the fluid to the particle, extended over the whole particle surface. $\boldsymbol{F_d}$ is mainly determined by the particle-to-air relative velocity, the cross-flow particle area and its drag coefficient C_d. The drag coefficient depends on the flow pattern through the particle Reynolds number, $\mathrm{Re}_p = u_r d / \nu$.

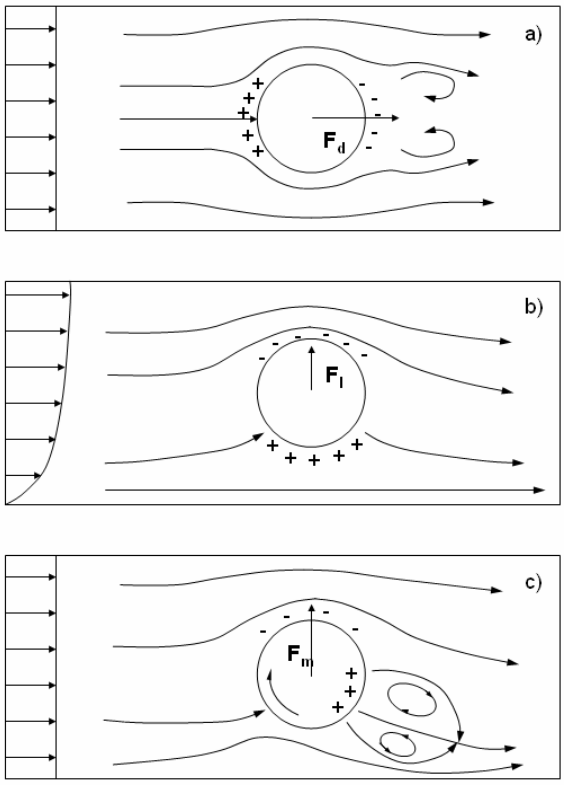

Figure 3.4. An illustration of drag, lift and Magnus forces acting on a spherical particle. Higher pressure is indicated with "+", while lower pressure with "-". a) aerodynamic drag due to viscous effects, flow separation and turbulence in the wake region of the particle. b) Aerodynamic lift due to the Bernoulli effect. C) Magnus force due to the combination of Bernoulli and viscous effects on a spinning particle. (Redrawn from Shao 2000).

Here, u_r is the particle-to-air relative velocity, d is the particle diameter (or an equivalent diameter) and ν is the air viscosity (approximately $1.46*10^{-5}$ m^2s^{-1}). Generally speaking, the Reynolds number is a measure of the relative importance of inertial (turbulent) to viscous forces; the higher the *Re*, the stronger the turbulent effects, with respect to viscosity effects. It arises any time an asymmetry in the flow field with respect to the body occurs. The lift origin is showed in

Figure 3.4b in the case of a spherical particle immersed in a shear flow. Through the Bernoulli law, it can be shown that a force in the direction of the velocity gradient arises in

such conditions. The lift force become important either for spherical particles in strongly sheared flows, or for particles with very low sphericity.

Finally, the Magnus force arises because of the rotation of the particle with respect to the fluid. It is perpendicular to both the rotation axis and the direction of motion. It can be explained similarly to the lift force: it arises because of a velocity gradient between the side of the particle that spins in the same direction of the fluid (higher relative velocity) and that spinning in opposite direction (lower relative velocity), in a rotating particles (Figure 3.4c).

3.1.3 Particle terminal velocity

Among the four forces, $\boldsymbol{F_l}$ can be neglected without introducing major errors in the prediction of particle motion (Shao, 2000) and in the interpretation of wind erosion phenomena. If we also neglect the Magnus force (although it can be relevant in certain circumstances, as underlined by White and Schulz (1977)), particle dynamic is only affected by gravity and drag forces. In this conditions, the material derivative of the i^{th} component of the particle absolute velocity $\boldsymbol{u_p}$ can be written as:

$$\frac{du_{pi}}{dt} = -\frac{u_{ri}}{\tau} - \delta_{i3} g \ . \tag{3.1}$$

The first term on the right-hand side of Eq. 3.1 is the force (per unit mass) due to drag (τ is the particle response time, a function of C_d, d, $\boldsymbol{u_r}$ and the particle-to-air density ratio σ_p) and the second term is the gravity (δ_{ij} is the Kröenecker delta).

Whether a particle remains airborne or it is deposited on the surface, depends basically on the balance of these two forces. It is of fundamental importance to distinguish particles that tend to remain suspended to those that are likely to fall because their weight. To this aim, the particle terminal velocity (w_t) is introduced. It is defined as the particle-to-air relative velocity at which particles experience zero acceleration. Starting from Eq. 3.1 and assuming the analytical expression for $C_d(Re_p)=24/Re_p$ - valid for small Re_p, (Durst et al., 1984; Kundu, 1990) - we can derive an analytical expression for the terminal velocity (details can be found, e.g., in Shao, (2000)):

$$w_t = -\frac{\sigma_p g d^2}{18\nu} \tag{3.2}$$

Thus, the absolute particle vertical velocity is $w_p = w + w_t$, where w is the air vertical velocity. If $w_p > 0$ the particle tends to remain airborne, otherwise it is deposited back to the surface. In Sect. 4.1.2 we will make use of the concept of terminal velocity to evaluate the influence of gravitational settling in the total fluxes of dust during intense wind erosion.

3.1.4 Friction velocity

To study the dynamics of wind erosion, the equations of air and particle motion are derived from the schematization of the Atmospheric Boundary-Layer (ABL); for a comprehensive description of the ABL theory refer to, e.g., Stull (1988). In the lower layer of the ABL, the so-called surface layer, the flow is mainly driven by the vertical gradients of mean quantities, thus the mechanisms leading to turbulent fluxes are analogous to those governing molecular diffusion in a laminar flow. Basing on this analogy, turbulent fluxes in the surface layer are expressed as a function of the gradients of relevant variables. For instance, the (turbulent) momentum vertical flux is:

$$\tau_t = K_m \rho \frac{\partial U(z)}{\partial z}. \tag{3.3}$$

Here, K_m is the turbulent exchange coefficient ($m^2 s^{-1}$), ρ is the air density (kg m^{-3}), $U(z)$ is the horizontal mean wind profile (ms^{-1}) and τ_t has units (N m^{-2}). The transfer of momentum is obviously the ultimate driver of wind erosion. It is worth notice, however, that very close to surface, in the so-called viscous sub-layer, the turbulent component of the momentum flux is overcame by the viscous shear stress (τ_v). This latter component, on the contrary, looses importance quickly as we move out of the surface. An important feature of the surface layer is that total momentum flux ($\tau = \tau_t + \tau_v$) remains fairly constant with z (Stull, 1988). In the surface layer we can thus introduce a scaling velocity, that turns out to be one of the most important variables, determining dynamics of the surface layer. This is the *friction velocity*, defined as:

$$u_* = \sqrt{\tau / \rho} \tag{3.4}$$

Friction velocity, as a representation of the force exerted by the wind on the surface, emerges as one of the most important quantities also in the description of wind erosion. It is a property of the whole surface layer, and is not a velocity associated to a certain quote.

K_m is commonly expressed as a function of u_*, as $K_m = \kappa u_* z$. With this assumption, wind profile above a rough surface (with aerodynamic roughness length z_0) can be derived by the ABL theory and expressed as a function of the friction velocity and of the quote above the surface as:

$$U(z) = \frac{u_*}{\kappa} \ln\left(\frac{z}{z_0}\right). \tag{3.5}$$

where κ is the Von Kármán constant ($\kappa \cong 0.4$).

At $z = z_0$ the mean wind vanishes, when extrapolated downward according to Eq. 3.5: this is an indirect definition of z_0. For a given mean wind speed at z, larger z_0 implies larger u_*, i.e. larger downward momentum flux. In this sense, z_0 describes how efficiently the surface absorbs momentum; it is thus of major importance in wind erosion studies (Marticorena and Bergametti, 1995). As a first approximation, z_0 is about 1/30 the height of the roughness elements. In wind erosion studies, both u_* and z_0 are usually derived indirectly by fitting wind profile measurements. However, is this work we calculate both variables directly: friction velocity is calculated by wind turbulent fluctuation measurements outside the viscous sub-layer; roughness length is estimated by means of roughness elements characterization.

3.1.5 Forces acting on surface particles: threshold friction velocity

Friction velocity is a property of the flow field, and in a sense describes its potentiality to cause erosion, or its *erosivity*: the higher the friction velocity, the higher the momentum flux, and hence the higher the erosivity of the wind field. It is natural, therefore, to characterize the surface susceptibility to wind erosion, or its *erodibility*, again in terms of a characteristic velocity, to be compared with u_*. Basing on this, the concept of the *threshold wind friction velocity* (u_{*_t}) was firstly introduced in the early work by Bagnold (Bagnold, 1941). This is defined as the minimum friction velocity required for the aerodynamic forces to overcome the "retarding forces", namely gravity and the inter-particle cohesive force, and to initialise the movement of soil particles.

The inter-particle cohesive force ($\boldsymbol{F_i}$) arises for particles resting on the surface, and it was not mentioned for airborne ones. Practical estimation of u_{*_t} imply a certain degree of arbitrariness in detecting the "beginning of particles motion". Efforts to derive a theoretical expression for the threshold friction velocity have been done, since the Bagnold's first proposition. In its scheme, Bagnold derived a formulation basing on the balance of only aerodynamic and gravity forces acting on resting particles, and neglecting the others. Greeley and Iversen revised this formulation, to account for the effects of inter-particle and lift forces, that are supposed to be dominant especially for smaller particles (Greeley and Iversen, 1985; Iversen et al., 1976; Iversen and White, 1982). Shao and Lu (2000) further modified this scheme making use of theoretical physical schematization of inter-particle forces for sand-sized particles. They derived an explicit scheme for u_{*_t}, that can be conveniently expressed in the short form (see Shao and Lu (2000) for details):

$$u_{*t} \propto \sqrt{\alpha_1 d + \alpha_2 d^{-1}} \tag{3.6}$$

where the first term under the square root accounts for the effects of gravity and drag, while the other accounts of inter-particle cohesion. Equation 3.6 accounts for the varying importance of the different forces with varying particle size. Fitting wind tunnel data, Shao and Lu (2000) derived a practical and easy-to-implement estimation of u_{*t}:

$$u_{*t}^2 = 0.0123\left(\sigma_p g d + \frac{5\cdot 10^{-4}}{\rho d}\right) \tag{3.7}$$

If the same parameterization of the inter-particle forces is used also for dust-sized particles, we can analyse the relative importance of the different forces for the spectrum of particles.

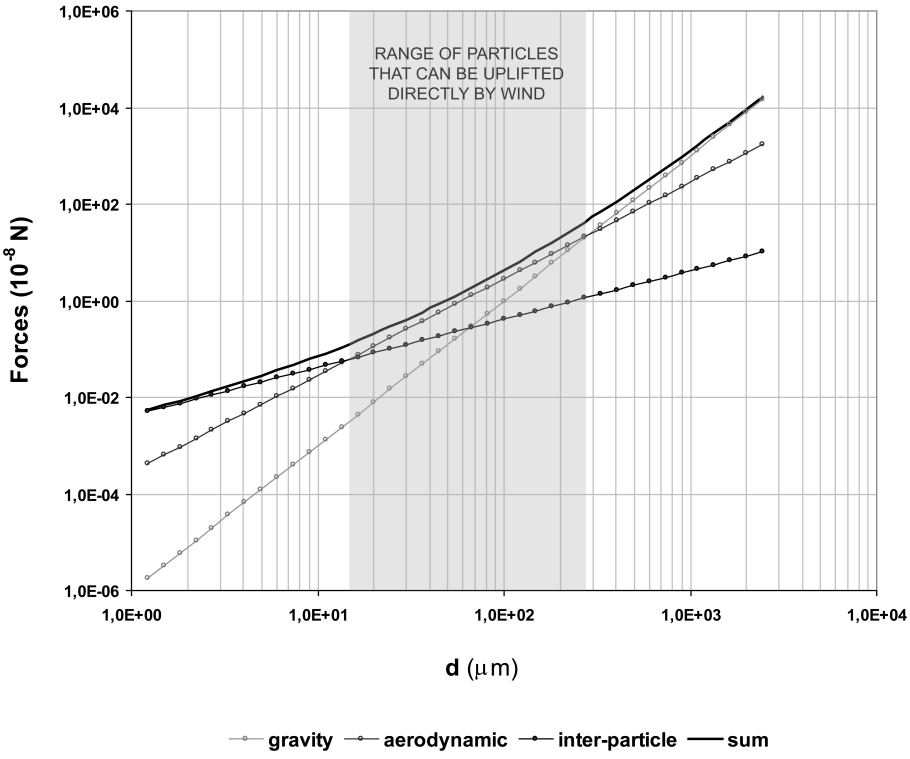

Figure 3.5. Relative importance of the forces acting on soil particles according to particle size. Gray area highlights the range of particles that can be directly uplifted by wind.

It will help clarifying some major features of wind effects on soil particles. Roughly, gravity force is proportional to d^3, aerodynamic forces are proportional to d^2 and total cohesive forces (including Van der Waals, electrostatic and capillary forces) are proportional to d. Figure 3.5 shows the relative importance of such forces at various sizes, for $u_* = 0.4$ ms^{-1}. It is easily recognized that particles smaller than 10 μm are by far dominated by bounding forces, hence they cannot be lifted at this friction velocity.

Aerodynamic forces dominate in the range ca. 10-300 μm; these particles are thus subject to uplift (their following fate depends again on their size and on the features of the flow field). At larger sizes, gravity dominates and particles are no longer uplifted; however, as we will see in the following, they can be subject to *creeping*. Chatenet et al. (1996) have shown that the loose wind-erodible fraction of arid soils can usually be considered as a mixture of at most three log-normally distributed soil aggregate populations. The geometric mean diameter and geometric standard deviation of the smallest of these modes are 125 μm and 1.6, respectively. This shows that the mass of finer particles (PM_{20}) present in arid soils in a free state is insignificant. These fine particles, that indeed exist within the soil, may be contained in two types of aggregates: they can either be glued to the surface of sand-sized grains or imbedded in aggregates of fine material. This is consistent with the former observation that inter-particle bounding forces dominate for very fine particles.

3.1.6 Other factors influencing threshold friction velocity

So far, to characterize soil erodibility we considered only forces acting on the particles themselves. To this respect, we can conveniently see the threshold friction velocity considered as an *uncorrected threshold friction velocity* u_{*t}^{0}. Indeed, other factors influence soil susceptibility to the wind action, either affecting momentum transfer or enhancing retaining forces; they act as "correction factors" on u_{*t}^{0}. Major influencing factors are soil moisture, soil cover by non-erodible elements and surface crusting or aggregation.Humidity has several important effects. First, it can increase u_{*t} indirectly by promoting vegetation growth (and hence, non-erodible cover). This effect can be taken into account by the means of z_0. Secondly, it can enhance the strength of inter-particle bonds in two ways: by promoting development of a humid film between grains (Fècan et al., 1999), or by favouring soil crusting. In the latter case, soil texture and composition are key parameters. For example, the type of physical crust that develops on soils with a very low content in fine particles (sandy soils) does not affect saltation, while stronger crusts that form on clayey or loamy soils are much more efficient in limiting availability of soil aggregates for saltation (Gillette and Passi, 1988).

Natural vegetation has a twofold role in protecting soil from wind erosion: it absorbs a part of the wind momentum flux by increasing surface roughness (Stockton and Gillette, 1990), thereby reducing wind erosivity and protects the soil surface from erosion, both by direct sheltering and by providing a "wake area" with high turbulence and zero mean velocity; furthermore, vegetation increases soil cohesion by retaining moisture and removes airborne

soil-particles in transport by “capturing” them (Kim et al., 2000). Several studies clearly showed that soil erodibility also depends strongly on the presence of clods, rocks, crop residues etc. (Raupach et al., 1993), that we can treat together as non-erodible elements. Experimental studies showed that the wind erosion thresholds observed on rough surfaces are significantly higher than those observed on smooth surfaces (Gillette and Stockton, 1989). Thus amount, stability and geometry of soil aggregates on the soil surface is a major factor affecting susceptibility of soil to erosion

Crust is the upper portion of the water-consolidated zone in the soil (Hagen, 2001), with high density. Soils with crusted surfaces without mobile aggregates are generally stable and have lower wind erodibility than similar un-crusted soils. The crust formation reduces the availability of mobile soil on the surface which explains the reduction in erodibility of crusted soils. The crusts can be formed due to structural properties of the soil (Chepil, 1951), salt concentration (Nickling and Gillies, 1984) or by microbial activity. The formation and stability of crusts and clods are related to clay content: increasing the soil clay content leads to the formation of bigger and stable soil aggregates which reduce the susceptibility of the soil to wind erosion. When the strength of the crust is augmented by an increase in the proportion of fine materials (clay), the amount of abrasion by saltating grains decreases (Rice and McEwan, 2001).

Taking all these effect into account, threshold friction velocity can be rewritten as:

$$u_{*_t} = u_{*_t}^0 \cdot R \cdot H \cdot M \tag{3.8}$$

In Eq. 3.8 the correction factors *R*, *H* and *M* account for surface roughness elements, soil moisture and surface aggregation and crusting, respectively. We will discuss some quantitative issues related these factors in Chapter 5.

3.1.7 Modes of particle motion

Creep, saltation and suspension

Particles that can be observed a few centimetres above a surface undergoing wind erosion cover a wide range of diameters - from about 0.1 μm to several hundreds of μm. However, particles of different sizes adopt different modes of motion during a wind erosion event.

In his work, Bagnold again provided for the first time a classification of the three main modes of particles motion under wind erosion, namely suspension, saltation and creeping (Bagnold, 1941). This classification, in its broad sense, is still considered valid. Here, we report a definition of such modes given by Shao (Shao, 2000):

Creeping. Particles lager than 1000 μm are to heavy to be lifted up even by very strong winds. However, they can be pushed along the surface by wind or by impact of other particles; thus, they roll or slide over the surface.

Saltation. It is the bouncing motion of sand particles, approximately in the range 70-1000 μm, across the surface. It is the principal mechanism of horizontal transport of soil particles in the wind direction. These particles can be either sand grains or aggregates of finer material. They are responsible for the formation and evolution of sand dunes and sand seas as well as of drifts of fence-lines. Typically, saltating particles are entrained into the atmospheric surface layer with an initial steep vertical velocity (forming an angle of about 55° with the horizontal), followed by an horizontal movement and return to the surface with a small impact angle (around 10°).

Suspension. After they are entrained into the atmosphere, particles smaller than approximately 70 μm often remain suspended in air, mainly because of their lightness and small terminal velocity. They can be relatively easily dispersed away from the surface by turbulent motions in the atmospheric boundary layer and carried by atmospheric circulations over large distances, up to thousands of kilometres (Shao, 2000). However, observations showed that only very fine particles, with an approximate upper limit of 20 μm can remain suspended for long time periods, up to several days (long-term suspension). Particles with a diameter between 20 and 70 μm remain suspended only for short periods of time (typically several hours).

Unless extremely favourable wheatear conditions occur, they are not transported further than few hundreds of kilometres. This is referred to as short-term suspension. As a consequence, the corresponding mass redistribution is of some importance at local scale only. Figure 3.6 shows an illustration of the particle modes, along with the main mechanisms of entrainment into and removal from the atmosphere.

This classification of saltating and suspended particle ranges, although important by a conceptual point of view, does not account for the effect of the actual flow field on particle motion.

A more objective definition is needed as long as accurate quantifications of dust emission are required. A quantitative definition can be derived if we consider that in order for a particle to remain airborne, the necessary condition is that its terminal velocity (w_t) is comparable or smaller than the mean vertical component of the Lagrangian velocity of the air parcel in which it is immersed (Shao, 2000).

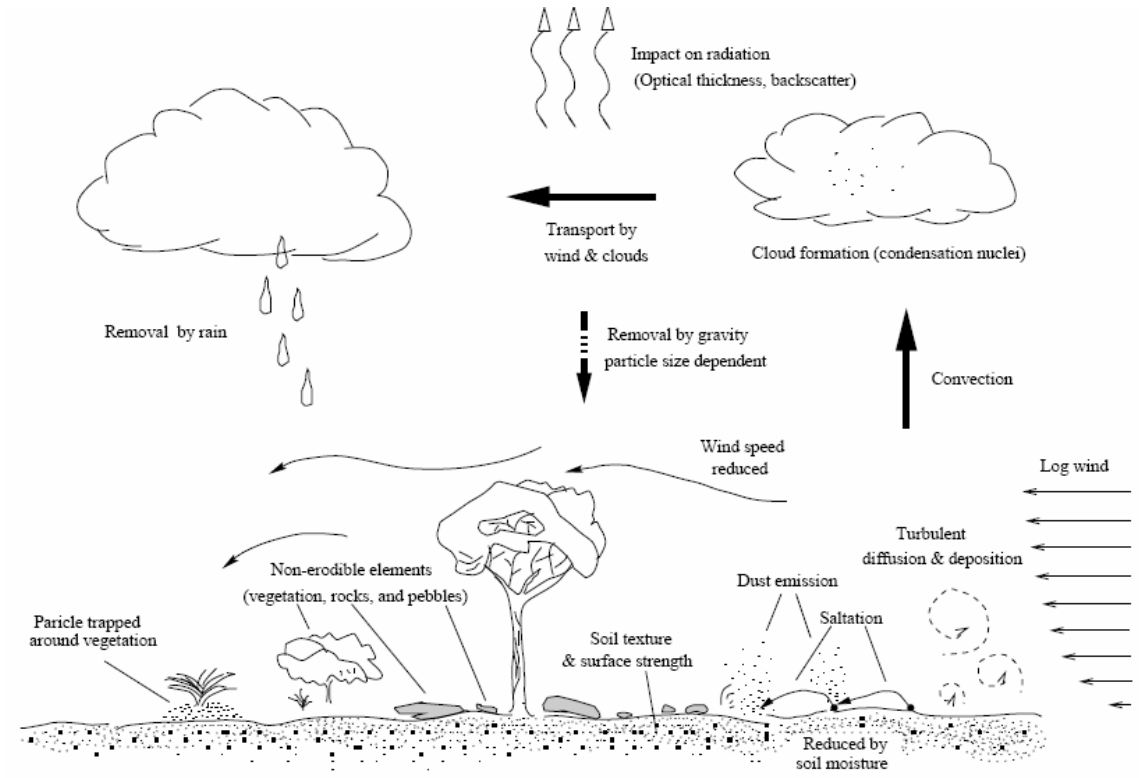

Figure 3.6. Sketch of particles motions and main processes of entrainment and removal from the atmosphere (redrawn from Lu (2000)).

The Lagrangian velocity is the velocity at which air parcels are dispersed upward by turbulence. In neutral atmospheric surface layers, the Lagrangian vertical velocity can be approximated by κu_*, where κ is, again, the Von Kármán constant. We can now introduce definitions of suspended and saltating particles on the basis of the ratio $|w_t|/\kappa u_*$. Suspended particles are those with a diameter smaller than d_1, with d_1 given by the solution of:

$$|w_t|(d_1) = \alpha_d \kappa u_* \tag{3.9}$$

Obviously, saltating particles are those with a diameter greater than d_1. An arbitrariness is introduced with the parameter α_d; a choice of 0.5, as in Shao et al. (1996) is a conservative definition of dust. Other authors set α_d to 1 (Scott, 1995).

On the basis of this definition, we can further refine the saltation classification. Pure saltation occurs only when turbulent fluctuations of the air flow do not affect particle motion to a large extent. In such conditions, saltation becomes a deterministic process, defined only by the initial conditions of particle motion and on the mean flow characteristics. We can define pure saltating particles as those with a diameter larger than d_2, where d_2 satisfies Eq. 3.9 with $\alpha_d = 5$.

Smaller saltating particles experience turbulent effects, thus their motion is referred to as *modified saltation*.

The splashing and sandblasting processes

At the downwind end of trajectories of saltating particles, their kinetic energy is partly transformed into heat in inelastic shocks, partly used to eject other aggregates from the soil (splashing), and the rest is used to release finer particles (approximately PM_{20}) from the aggregates or from the soil surface (sandblasting). In addition to the former theoretical derivation, there is much experimental evidence (Gillette and Walker, 1977; Houser and Nickling, 2001; Shao et al., 1993) to prove that direct mobilization by aerodynamic forces plays a minimal role in emissions of very fine particles and that these emissions can be considered as a direct consequence of saltation. Thus, from a formal point a view, it is natural to disconnect the study of sandblasting from the one of saltation. This idea was first developed by Gillette (1977) who compared sandblasting efficiencies of various natural soils in the south-western part of the US. The sandblasting efficiency was defined as ratios of measured PM_{20} vertical fluxes to measured horizontal saltation fluxes (F_h).

After Bagnold (1941), the basic knowledge of the saltation process was derived from wind tunnel simulations performed in ideal conditions. Indeed, experiments were carried out in dry conditions, at controlled wind speeds, over sand beds made of grains having all the same size and deprived of non-erodible elements. Various expressions accounting for the dependence of the horizontal saltation flux to the wind friction velocity were proposed (see Greeley and Iversen (1985), for a review). Well above the threshold friction velocity, the horizontal flux has been proved to be proportional to u_*^3.

Given that saltation is the ultimate cause of dust emission through sandblasting, one expects to find a quantitative relation between the horizontal fluxes of saltating particles (F_h) and vertical emission of dust (F_v). This can eventually take the form of a relation between F_v and u_*.

Mostly relying on field or wind tunnel tests, many researchers attempted to derive such a relation (Lu and Shao, 1999). Nevertheless, this seems to be not fully understood yet, although an increase of F_v with increasing u_* is always observed. The relation has been observed to spam from $F \propto u_*^{1.89}$ to $F \propto u_*^{6.54}$ (Houser and Nickling, 2001; White et al., 1996). Such variations have been variously attributed to inter-particle bonds strength or crusting effects.

Basing on the theoretical ground set up by Owen (1964), Gillette and Passi (1988) suggested that dust emission rates are proportional to u_*^4. Nickling and Gillies (1989) identified five classes to analyse data from their experimental sites, according to land use and surface morphology; they found some good correlations with the following formulas:

1) Natural undisturbed desert sites: $F \propto u_*^{2.99}$
2) Sites developed by fluvial processes: $F \propto u_*^{3.32}$
3) Construction sites: $F \propto u_*^{4.24}$
4) Mine tailings: $F \propto u_*^{2.93}$

while they acknowledged a wide scatter for agricultural soils. Later in this thesis (Sects. 5.2 and 5.5.2), we will confirm to some extent both the results from the alluvial sites and the large scatter from the agricultural sites.

3.2 Existing techniques for wind erosion measurement

Laboratory and field wind tunnel experiments provided the core of our present understanding of wind erosion processes; site-scale field monitoring provided valuable data to cross-check wind tunnel experiments, while network of sand drift and dust movement samplers strongly helped figuring out a comprehensive, regional scale picture of wind erosion patterns and atmospheric dust transport; attempts to assess wind erosion patterns at regional scale have also been done basing on indices derived from wind erosivity and soil erodibility, using remotely-sensed images and atmospheric data.

For the aim of this work we limit attention to the techniques used to quantitatively assess dust emission and to investigate the process of sandblasting. With this regard, the most important quantities to be measured are the horizontal saltation flux (F_h), and the vertical dust emission flux (F_v). According to Shao (2000), most of the understandings in such field have been achieved with the aid of wind tunnel experiments. Wind tunnel allows to study the phenomena in controlled conditions, to analyse the implications of different factors separately and to vary the controlling parameters arbitrarily. Laboratory wind tunnel tests have been used to investigate saltation (Bagnold, 1941), determination of the threshold friction velocity (Iversen et al., 1987), the equilibrium of saltation (Shao and Raupach, 1992), the process of dust emission (Rice et al., 1996; Shao et al., 1993), as well as the formation of sand dunes (Tsoar et al., 1985). Portable wind tunnels have also been designed to investigate wind erosion in controlled wind conditions on natural surfaces. Indeed, the process of collecting undisturbed soil surface samples is critical and even small

disturbances can influence the results largely. Among others, Nickling and Gillies (1989) and Leys and Raupach (1991) reported results of such experiments. The interpretation of wind tunnel experiments, however, is highly uncertain and extrapolation of the results to the natural environment disputable. Indeed, while some general features of the flow field can be relatively easily reproduced in a wind tunnel (such as the logarithmic mean wind profile), it is virtually impossible to retain a good dynamic similarity. Even the condition of retaining same Reynolds and Froude numbers (that is, in fact, not enough for a complete dynamic similarity) is extremely difficult in a wind tunnel. Simulating effects of (artificial) vegetation is even more critical, because the geometrical simulation between vegetation height and particle size cannot be preserved. After Stout (1990), Shao & Raupach (1992), Zobeck et al. (2003) and Dong et al. (2004), it is clear that to achieve fully developed saltation (equilibrium of saltation) it is required a sufficient *fetch*, that can extend from tens to hundreds of meters (*overshoot effect*). This distance, that is obviously not available in a wind tunnel, has been seriously underestimated with wind tunnel experiments (about 20 m). Shao (2000) reports another major example of mismatch between field and tunnel tests; the so-called saltation roughness z_{0s} (that is a measure of the apparent surface roughness due to saltating particles): a difference of one order of magnitude has been found with the two different approaches. Moreover, temporal changes in environmental conditions (e.g., climate, soil properties, vegetation) are not sufficiently taken into account.

Concerning the field measurements, because of difficulties in objectively measure vertical fluxes of dust, horizontal fluxes are often measured and used to indirectly derive vertical fluxes by means of theoretical relations, such as those aforementioned (Sect. 3.1.7). Saltating particles can be measured directly using sediment samplers (also called sand traps) or inferred using electronic samplers. Passive samplers - such as the Bagnold trap, the Fryrear trap and the Leach trap, the Modified Wilson and Cook trap, (Zobeck et al., 2003) - rely only on the wind to maintain the inlet flow. Because concentration differences can be very low, long time sampling allows more accurate estimation of fluxes. It implies that measurements based on this method are, by nature, slow. Nonetheless, detailed study of particle emission (and transport) may require high sampling frequencies. Thus, fast-responding sensors are needed. Sensors for fast measurement of saltation fluxes have been realized. For example, SENSIT (Stockton and Gillette, 1990) samples particles basing on the piezoelectric effect. Unfortunately, because of limits in sensitivity, it can be used only for relatively large particles (> 100 μm). Its use is thus limited to saltation fluxes.

Direct estimations of vertical dust fluxes have been attempted. Most of them are based on the *k*-theory. It states that – provided particle concentration is horizontally homogeneous - the turbulent component of the emission flux is proportional to the vertical concentration gradient, according to:

$$F_{vt}(d) = Kp(z,d)\frac{\partial c(z,d)}{\partial z} \tag{3.10}$$

Here, $c=c(z,d)$ is the particle concentration (kg m^{-3}) and K_p ($m^2 s^{-1}$) is the particle-eddy diffusivity, that basically accounts for the turbulent effects in a laminar-like analogy similar to the one used in Eq. (3.3). K_p is usually derived by analogy with the momentum flux; however, mainly because of the forces acting on moving airborne particles, K_p can differ strongly from K_m, and depends both on the particle size and on the quote. Subscript "*t*" in F_{vt} recalls that this is the turbulent component of such flux, that must be added to the gravitation component:

$$F_{vg}(d) = w_t(d)c(z,d)\,. \tag{3.11}$$

Generally speaking, this latter component should not be neglected a priori, even though it is usually small when strong wind erosion occur. This topic will be further explored in the Sect. 5.2. Calculation of the total flux following the *k*-theory requires measurements of particle (dust) concentration at, at least, two different heights. Samplers used to this aim are, generally, active samplers. These use a pump to maintain the inlet flow, thus they can feature finer meshes and sample smaller particles (< 2 μm) than the passive samplers do; they are not generally isokinetic, unless the flow is actively controlled by means of a mass flow controller, commanded by an independent wind speed measure. However, among others, Zobeck et al. (2003) pointed out that sampling efficiencies of active samplers at high wind speed is highly uncertain.

Although use of pre-weighed filters to determine dust mass is probably the easiest and cheapest method, dust mass can also be determined, e.g., by total elemental analysis (by proton X-ray emission, (Johansson and Campbell, 1988) or X-raw fluorescent spectrometry, (Quisefit et al., 1994)). Optical sensors, based on the light-scattering phenomena, are used for very fast measurements of dust concentration. Large uncertainties remain on the sampling efficiencies at high wind speeds for optical sensors; this is the major shortcoming of such sensors, that might be overcome with a calibration of the instruments based on laboratory tests of sampling efficiencies.

Shao (2000) recognized that "instruments for measuring dust fluxes with high sampling frequencies do not seem to exist". Because wind erosion is a scattered and intermittent

phenomenon, such an instrument would allow to study the emission processes in details and to accurately determine the relative importance of influencing parameters.

3.3 Wind erosion modelling and the issue of model validation

Existing wind erosion models can be divided in two categories: those focusing on horizontal soil fluxes and those that predict suspended dust emissions (vertical dust fluxes) due to wind erosion; this rough distinction reflects the two main interests of scientists dealing with wind erosion: on the one hand, one is interested in assessing the amount of soil lost due to the wind action; this is especially important to assess loss of soil productivity, for agricultural purposes. On the other hand, dust emission is relevant both for air quality studies and for global implications as widely discussed in Chapters 2.

Basing on early wind tunnel and field experiments of Bagnold (1941) and Chepil (1951) the Wind Erosion Equation, WEQ, (Woodruff and Siddoway, 1965), was derived; later on, it has been revised (RWEQ, Fryrear (1986)); it is based on empirically derived relationships among major factors controlling wind erosion. The US Environmental Protection Agency modified the WEQ to estimate fraction of eroded soil that becomes Total Suspended Particulate (TSP). Among the vertical dust flux prediction models, EPA model assumes that emissions generated by wind erosion depend on the frequency of disturbance of the erodible surface, because each time a surface is disturbed, its erosion potential is restored. Gillette and Passi (1988) developed a model to estimate total dust production; it is based on the probability density function of wind speed during the periods of interest, correlating the dust emission also to a threshold friction wind speed. This approach has been used later, for example by Nickling and Gillies (1993) and Tegen and Fung (1994). Finally, models have been developed that predict both horizontal soil fluxes and vertical dust fluxes: the Texas Erosion Analysis Model, TEAM, (Gregory and Darwish, 2001), treats the threshold friction velocity as a variable rather than a constant, taking into account particle diameter, soil moisture and wind friction velocity. Shao et al. (1993) derived another theory of dust emission based on consideration of particle binding energy and of the energy balance of a single saltation impact. The wind erosion prediction system (WEPS) developed by Hagen (2001) in a process-based, continuous, daily time step model simulating wind erosion and vertical fluxes, considers spatial and temporal variability of input data and of sub-processes that modify soil erodibility. Other modelling approaches (Saxton et al., 2000) calculate vertical flux multiplying a soil dustiness index (PM_{10}/TSP) and horizontal flux derived from empirical equations similar to the original WEQ.

Among main limitations of models discussed above, the treatment of vertical fluxes as fraction of horizontal fluxes is perhaps the most striking: indeed, while it has been shown that horizontal soil losses reach a saturation value (the so –called *maximum transport capacity*), vertical dust fluxes do not; therefore it would be inappropriate to scale vertical dust fluxes from the horizontal saltation fluxes predicted with this model. Moreover, it is necessary to consider the variability of threshold wind speed, small scale topographic features and other influencing parameters, both climatic and environmental. The energy-based model of Shao et al. (1993) has uncertainties in estimating dust particle binding energy and in considering kinetic energy of saltating particles, that is not conservative, as a proportion is converted into heat. In contrast to energy-based model, a new model (Lu and Shao, 1999) estimates dust emission on the basis of the volume removed by impacting sand grain, related with particle impact velocity and impact angle (volume-based model).

As introduced in the previous Section, most instruments to assess dust emission by wind erosion are based on the direct measure of horizontal fluxes of saltating particles. Vertical fluxes of suspended particles are then derived indirectly, by means of theoretical relations, such as the *k*-factor theory (Ono et al., 2003), basing on some hypothesis about the physics of erosion. These relations are analogous to the ones used in the wind erosion models. As a consequence, these instruments cannot be used to validate models. To validate and evaluate dust emission models it is needed an instrument whose determinations are fully independent from the model to be validated.

In the following chapter we present an instrument developed to fill the gaps individuated in Sects. 3.2 and 3.3. It is designed to measure dust fluxes at the field scale, at high frequencies and without introducing disturbances that may affect the “natural” processes. It allows interpretation of the main dynamics involved in the wind erosion process, including dependencies on wind speed and direction, climatic conditions, vegetation cover. Vertical dust fluxes are here measured directly, independently from the mechanisms that led to the emission. This makes the system suitable for model validation and tuning. The system is based on the *eddy covariance* theory, firstly developed in the framework of gas fluxes. Here, we extend this theory to dust-sized particles and interpret the former formulation as the limit case of particles with negligible mass.

Particles concerned here fall in the aerodynamic range 0.35-9.50 μm, representing both the bulk of PM_{10} (in terms of mass) and the range that can be measured with commercial OPC

with a sufficient accuracy. The mathematical formulation will help defining the limits of applicability of the eddy covariance to such particles and interpreting experimental results.

4
THEORY, MATERIALS AND METHODS

4.1 Extension of the eddy covariance theory to dust-sized particles

The so-called *eddy covariance* (EC) is the supporting methodology to many field of investigation. Among them, the greenhouse gases surface exchange is probably the most popular. Great part of the theoretical benchmarks that helped refining the methodology have been achieved in the framework of CO_2 and H_2O fluxes, as well as of VOCs and ultra-fine aerosol fluxes. To get a thorough overview of the theory and the related methodologies refer to Aubinet (2000), Baldocchi et al. (1988), Valentini et al. (1996), vanDijk et al. (2004). For an overview of EC in Italian, refer to, e.g., Sozzi et al. (2002).

Recently, fast methods exploiting the EC approach have been developed and tested to derive time-integrated emission rates of aerosol particles released in urban areas from anthropogenic sources (Dorsey et al., 2002; Martensson et al., 2006; Nemitz et al., 2000). In particular, Nemitz et al. (2000) used an optical particle counter (OPC) to get size segregated fluxes of particles larger than 0.1 μm over the city of Edinburgh. While OPC are suitable sensors for the fast detection of particles in the coarse mode (D3 mode), the possibility to apply the EC method to their flux determination needed to be verified.

4.1.1 The origin of the problem

Any kind of particle (either gaseous, liquid or solid) immersed in a flow field is subject to stresses, exerted by the fluid. Because of their negligible mass, gases and ultra-fine aerosols (with diameters in the nanometres range) respond to such stresses with an infinitesimal delay. As a consequence they are subject to the same accelerations experiences by the air parcels and follow exactly the same trajectories. A scalar quantity immersed in a flow field,

which exhibit such behaviour is called a “passive scalar”. Passive scalars not only follow exactly the flow field, they also do not cause any modification in it. This has the major implication that the air flow field can be firstly studied independently; its forcing on the scalar motion can be later analyzed separately. Passive scalar behaviour is typical, for example, of the temperature field, that can be considered a perfect passive scalar (its mass is null), as long as it does not induce buoyancy effects.

However, dust particles in the atmosphere are heavy particles, as their density (around 2600 kg m^{-3}) is much larger than that of the air (around 1.2 kg m^{-3}). Mass induces both inertia and gravity effects on particles. In particular, inertia causes particles to respond slowly to turbulent fluctuations, while gravity causes particles to have a mean downward motion even in still air. Figure 4.1 shows schematically the action of these two forces on the particle motion. Such forces cause the scalar to deviate from the trajectories of the air parcel where it is immersed. Deviating from the trajectory of its companion eddy, a particle undergoes the influence of new eddies. In general, these impose a third cause of deviation from the original streamline; this effect is referred to as the “trajectory crossing effect” (Yudine, 1959).

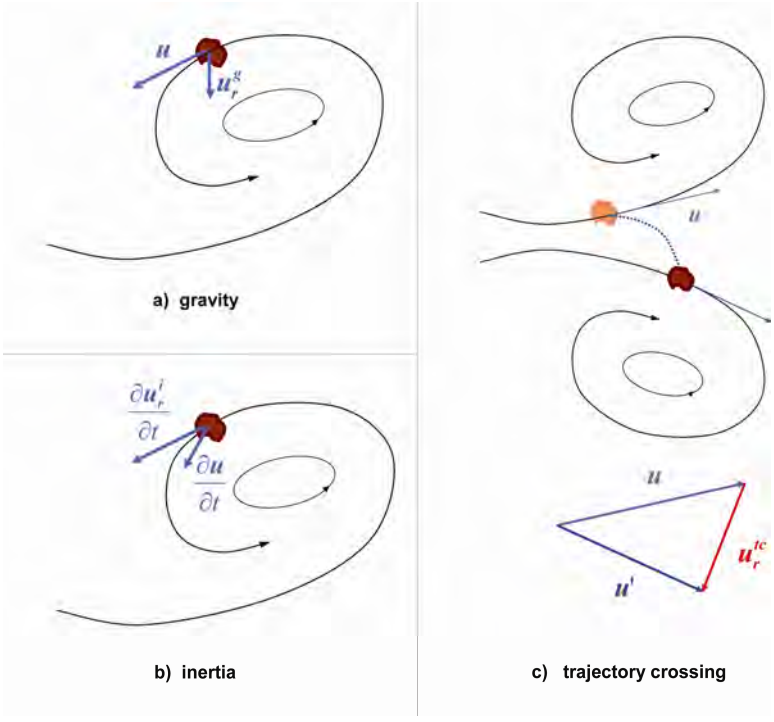

Figure 4.1. Schematic view of the effects of gravity, inertia and trajectory crossing on the motion of a particle immersed in a flow field.

Though its origin is in the inertia and gravity forces, the trajectory crossing effects - through the presence of a new stochastic companion eddy - induces an *independent* deviation component. As a result, particle velocity $\boldsymbol{u_p}$ differs from fluid velocity $\boldsymbol{u}$, this difference being represented by a particle-to-fluid relative velocity $\boldsymbol{u_r}$:

$$\boldsymbol{u_p} = \boldsymbol{u} + \boldsymbol{u_r} . \tag{4.1}$$

Because of this relative velocity, the EC technique, as established for gases, cannot be applied directly to heavy particles. However, under certain conditions, a modified formulation for the EC is still possible.

4.1.2 Theoretical constraints to the application of the eddy covariance to dust particles

A theoretical treatment is needed to estimate the fraction of mineral dust to which the EC approach can be safely applied. This can be done starting from the conservation equation of particle concentration in an atmospheric flow field:

$$\frac{\partial c}{\partial t} + u_{pj}\frac{\partial c}{\partial x_j} = S + \gamma \nabla^2 c \tag{4.2}$$

where c is the concentration of particles expressed in suitable units; u_{pj}, is the j^{th} component of the particles velocity vector $\boldsymbol{u_p} \equiv (u_p, v_p, w_p)$ in a suitable coordinate system, in which the (x,y)-plane is parallel to the local surface and positive z points out of the surface; γ is the particles diffusivity in atmosphere ($m^2 s^{-1}$), $S = S(\boldsymbol{x},t)$ is the source/sink term. By applying the ensemble average operator to Eq. (4.2) and the Reynolds decomposition to all variables, Eq. (4.2) becomes:

$$\frac{\partial \overline{c}}{\partial t} + \overline{u}_p\frac{\partial \overline{c}}{\partial x} + \overline{u'_p\frac{\partial c'}{\partial x}} + \overline{w}_p\frac{\partial \overline{c}}{\partial z} + \overline{w'_p\frac{\partial c'}{\partial z}} = \overline{S} + \gamma \nabla^2 \overline{c} \tag{4.3}$$

where an overbar means (ensemble) average and primes mean fluctuations around the average. For the sake of simplicity, Eq. (4.3) was written for the case in which the x-axis was aligned with the mean horizontal velocity.

Taking into consideration the three independent effects that give raise to a particle-to-air relative velocity $\boldsymbol{u_r}$, it can be rewritten as:

$$\boldsymbol{u_r} = \boldsymbol{u_r^g} + \boldsymbol{u_r^i} + \boldsymbol{u_r^{tc}} \tag{4.4}$$

where the components g, i and tc refer to the terms accounting for gravity, inertia and trajectory-crossing effects, respectively. Equation (4.4) can be simplified by applying the

Reynolds decomposition to $\boldsymbol{u_r}$ and by analysing the contribution that each process gives to time averaged value of the particle velocity ($\overline{\boldsymbol{u}}_r$) and to its fluctuating components ($\boldsymbol{u}_r'$). Since only gravity affects the average value of particle velocity, we can write:

$$\overline{\boldsymbol{u}}_r = \overline{\boldsymbol{u}}_r^g = w_t * \boldsymbol{k} \tag{4.5}$$

where w_t is the particle free fall velocity (also called terminal velocity) acting along the vertical axis ($\boldsymbol{k}$ is the vertical unit vector). As far as the fluctuations are concerned, the only components affecting $\boldsymbol{u}_r'$ are those associated with inertia and trajectory-crossing effects ($\boldsymbol{u}_r' = \boldsymbol{u}_r'^{i} + \boldsymbol{u}_r'^{tc}$). However, it has been shown that in the atmosphere the contribution of inertia is negligible for particles with diameters up to about 500 μm (Csanady, 1963). The fluctuating component of $\boldsymbol{u_r}$ can thus be simplified to:

$$\boldsymbol{u}_r' = \boldsymbol{u}_r'^{tc}. \tag{4.6}$$

Taking into account Eqs. (4.5) and (4.6), Eq. (4.3) becomes:

$$\frac{\partial \overline{c}}{\partial t} + \overline{u}\frac{\partial \overline{c}}{\partial x} + \overline{u_p' \frac{\partial c'}{\partial x}} + (\overline{w} + w_t)\frac{\partial \overline{c}}{\partial z} + \overline{w_p' \frac{\partial c'}{\partial z}} = \overline{S} + \gamma \nabla^2 \overline{c} \tag{4.7}$$

If molecular diffusion effects are small with respect to turbulent stresses and no horizontal turbulent flux divergence occurs, integration of Eq. (4.7) along z gives rise to:

$$\underset{I}{\int_o^{h_m} S dz} = \underset{II}{\overline{w_p' c'}\Big|_{z=h_m}} + \underset{III}{\int_o^{h_m} w_t \frac{\partial \overline{c}}{\partial z} dz} + \underset{IV}{\int_o^{h_m} \frac{\partial \overline{c}}{\partial t} dz} + \underset{V}{\int_o^{h_m} \overline{u}\frac{\partial \overline{c}}{\partial x} dz} + \underset{VI}{\int_o^{h_m} \overline{w}\frac{\partial \overline{c}}{\partial z} dz} \tag{4.8}$$

where *I* is the scalar source/sink term; *II* represents the vertical turbulent flux at height h_m; *III* is the flux due to gravitational advection, *IV* represents the storage of the scalar below the measurement height; *V* is the flux due to horizontal advection and *VI* the one due to fluid vertical advection.

If atmospheric stationarity and horizontal homogeneity are achieved, the last three terms of the right-hand side of Eq. (4.8) can be neglected, and the working equation for the EC of particles becomes:

$$F_p = \int_o^{h_m} S dz = \overline{w_p' c'}\Big|_{z=h_m} + w_t \overline{c}\Big|_{z=h_m} \tag{4.9}$$

in which h_m is the height at which measurements are performed. Equation (4.9) states that the particles source/sink term, equivalent to the net release of particles F_p, equals the sum of the vertical eddy flux and the gravitational settling flux.

This expression reduces to the one commonly used for gases:

$$F_p = \overline{w'c'} \tag{4.10}$$

when:

$$w_t \cong 0 \qquad \text{and} \qquad w_r'^{ct} \cong 0 \;\Rightarrow w_p' \cong w' \tag{4.11}$$

Conditions (4.11) occur when gravitational settling is small with respect to the turbulent flux, and the trajectory crossing effect is negligible, as expected.

To assess in which conditions gravitational settling can be neglected, a preliminary analysis was performed on the basis of the particle terminal velocity w_t. According to Shao (2000) particles are likely to remain airborne if the mean vertical Lagrangian velocity of the air parcel surrounding them is larger than w_t. The particle terminal velocity is given by Eq. (3.2). Since a particle-to-air density ratio of ca. 2200 can be reasonably assumed for mineral dust, particles with aerodynamic diameters of 9.50 and 1.35 μm should have settling velocities of ca. $3.9*10^{-3}$ ms^{-1} and $7.9*10^{-5}$ ms^{-1}, respectively. In a neutrally-stratified atmospheric surface layer, the mean vertical component of the Lagrangian velocity can be estimated (Hunt and Weber, 1979) by the product κu_*, between the Von Kármán constant ($\kappa \cong 0.4$) and the friction velocity, u_*. By considering that during wind erosion events u_* is always well above 0.2 ms^{-1}, the corresponding Lagrangian velocity is higher than $8*10^{-2}$ ms^{-1}. This implies that gravitational settling can be neglected with respect to turbulent diffusion.

The optical diameter (D_{opt}) corresponding to this aerodynamic fraction (D_{ae}) can be estimated by recalling that:

$$D_{ae} = D_{opt} \cdot \rho_p^{\,1/2} \cdot f(D_{opt}, m) \tag{4.12}$$

in which (ρ_p) is the normalized density of particles and m is the refractive index. The function $f=f(D_{opt},m)$, is usually taken in the form of a 2nd-order polynomial function in m, the coefficients depending on the diameter range (McMeeking, 2004). For northern Asian dust, the refractive index can be considered to be $m=1.53$ (Clarke et al., 2004), thus $f(D_{opt},m)$ is around 0.85. Since the density of fine soil particles measured in the sites investigated was ρ_p=2.5 g cm^{-3} (see below), $D_{ae} \cong 1.35 \cdot D_{opt}$. This means that fluxes of particles with an optical range up to ca. 7.00 μm could have been safely measured by EC. The equivalence between net fluxes and the co-variance between the vertical wind and particle concentrations also requires that stringent criteria are followed in the selection of the measuring site to meet horizontal homogeneity and isotropy conditions. We will see in the Sect. 4.4 how the sites selected to monitor wind erosion meet these requirements strictly.

4.2 The EOLO system for direct measurements of mineral dust fluxes

In Sect. 4.1 we set up the mathematical framework for the application of the eddy covariance approach to mineral dust particles. In Sect. 4.1.2 we concluded that inertia and gravity effects can be safely neglected when applying eddy covariance for measuring fluxes for particles with optical diameters up to about 7 μm. With the OPC selected, counting efficiencies larger than 90% were possible for particles with an optical diameter ranging between 0.26 and 7.00 μm. By using the conversion procedure described in the previous section, size-segregated fluxes of mineral dust particles with aerodynamic diameters between 0.35 and 9.50 μm could have been measured with our system. It covers the largest portion of mineral dust mass subject to long range transport.

In this Chapter we present a new technology that realizes dust flux measurements basing on this theory. The first prototypal realization, that comprises commercial sensors for wind and concentration measurements, has been designed and engineered in a joint–venture between DiSAFRi (Univ. of Tuscia, Viterbo, Italy) and FAI Instruments s.r.l. (Rome, Italy, URL: www.fai-instruments.it). It has been given the name EOLO, that stands from Eddy cOvariance-based upLift Observation system. It was equipped with a software for data processing, also developed within this thesis. The system has been validated in a field campaign carried out in the framework of the WinDust project (Sect. 2.4.3). The validation strategy and results are illustrated in the next Chapter.

4.2.1 Hardware

A schematic view of the first prototype of EOLO is shown in Figure 4.2a. It is comprised of two main sections: the wind system and the concentration system. The wind system consisted of an ultrasonic anemometer Metek USA-1, (Metek GmbH, Elmshorn, Germany), allowing a fast and accurate measurement of the 3-D wind components and sonic temperature. This last parameter also provides a good estimation of the air temperature, especially in the dry conditions occurring in the desert. The concentration system, shown in Figure 4.2b includes several parts. The most important are the OPC (CI-3100 series, Climet Instruments Co., Redlands, CA, USA) and the Multi-Channel Analyzers (MCA8000, Amptek Inc., Bedford, MA, USA).

To minimize uncertainties, the inlet of the measuring system was directly attached to the anemometer. In our design, sampled particles were split in two channels: the so-called finer channel (D_{opt} from 0.26 to 0.54 μm) and the coarser channel (D_{opt} from 0.54 to 7.00 μm).

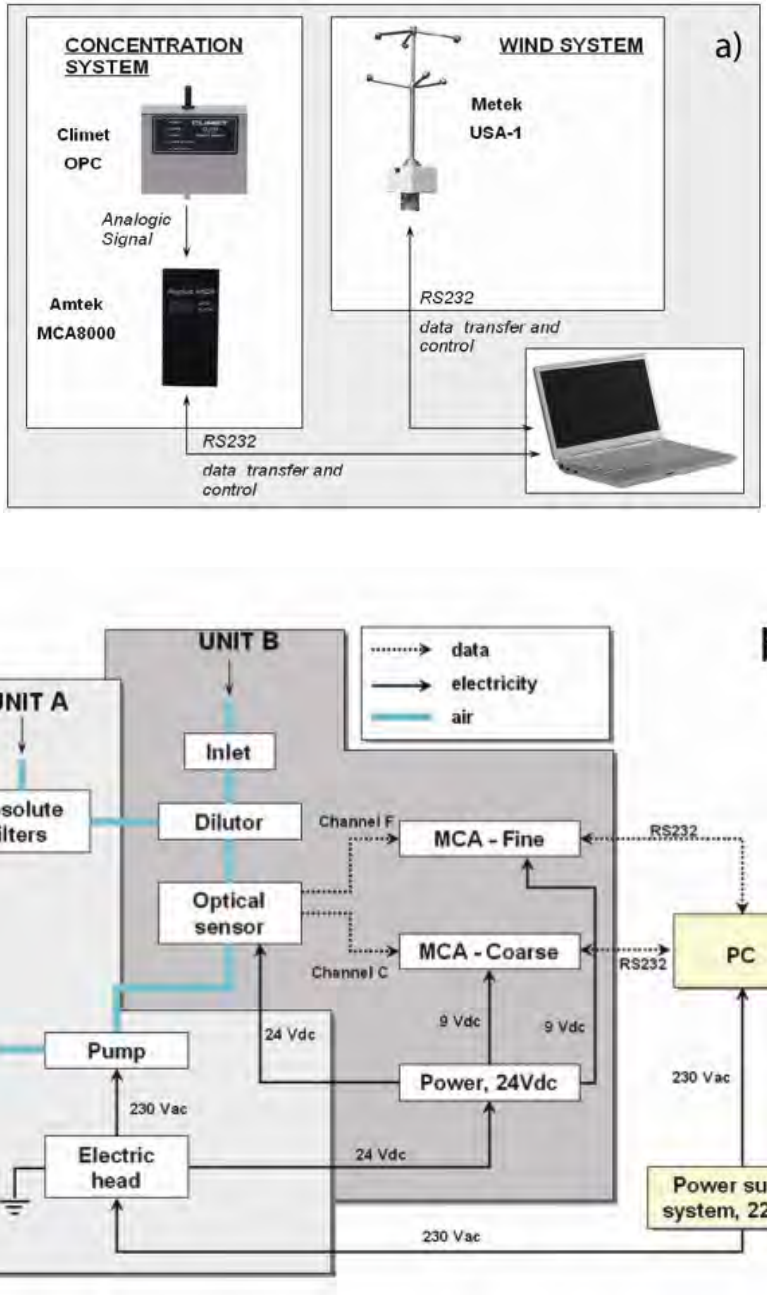

Figure 4.2. a) simplified view of the eddy covariance system for measuring fluxes of mineral dust particles (EOLO); b) details of the concentration system, engineered by FAI Instruments (Rome, Italy)

The system simultaneously acquires data from the two channels through dedicated MCA devices. “Finer” and “coarser” particle number concentrations are stored every 30 minutes. This time period, which also corresponds to the averaging time in Eq. (4.10), was selected on the basis of the experience acquired by EC of gases. It represents the best compromise to achieve a correct sampling of turbulent eddies and to get averaging times short enough to meet the steady-state condition required by the theory (Aubinet, 2000; Aubinet et al., 2001; Goulden et al., 1996).

The acquisition frequency was also carefully chosen. While high sampling frequencies are needed for an accurate collection of smaller eddies, their use might lead statistically poor sampling of large particles. In the case of mineral dust particles, it was found that an acquisition frequency of 5Hz represented the best compromise between these opposite requirements. In any case, the system was built in a way that all acquisition features, with the exception of the “finer” and “coarser” channel selection, could have been changed by the operator.

According to Buzorius et al. (2003), the main sources of particle signal dumping are due to the finite time response of the sensor and the attenuation of fluctuations within the sampling line if the flow is laminar. Figure 4.2b shows details of the pneumatic circuit and the data acquisition system. A pump was used to deliver the air to the sensing device where each particle was counted and sized based on the back-scattered light of a diode laser. In our case, total flow rate was 28.4 lpm, split as 1.42 lpm of sample air and 26.98 lpm of clean air, and was kept constant by a critical nozzle inserted in the flow path. Such dilution was needed to avoid masking effects of particle counting during high concentration periods. The dilution was applied some 3 cm after the sampling inlet, and the total tube length, from the inlet to the sensor, was 124 cm. Inner tube diameter was 6.35 mm, thus the flow was strongly turbulent (Re= 6280) essentially throughout the whole sampling line. Moreover, the OPC does not feature a real sampling volume. Particles pass in a 5.3 mm tube and are counted as they pass. The intrinsic time response of the sensor is thus limited only by the electronics needed to acquire and convert signals. The A/D converter and the acquisition via serial port was tested with a 10 Hz signal. Results show that the signal is correctly sampled. We can thus conclude that particle signal dumping is negligible in our experimental setup.

The system was able to simultaneously record counts of particles falling in 18 size ranges. The number of particles per unit of sampled volume (number concentration) was than obtained. It will be indicated in the text as $N_{a,b}$, where a and b define the range under consideration. N will be conveniently replaced by V or M, referring to particle volume or mass concentrations, respectively. These latter values were estimated by assuming that spherical particles exhibiting the same, constant density.

The system was located inside a tough case to protect the instrumentation from shocks or falls occurring during transport or during storm events.

4.2.2 Software

The software needed to control the system and process data has been fully developed. In particular, an ANSI-C program controls the hardware devices, synchronizes the acquisition from the 2 serial connections, acquires and store raw data in a specified format. Several acquisition features can be modifies by the end user at run-time: (i) the acquisition frequency, (ii) the duration of the acquisition per channel, (iii) the gain of the MCA, that is the number of electrical channel to be acquired. Due to the hard conditions in which the system is designed to work (in remote areas, in adverse weather conditions, possibly powered by gasoline generator), the acquisition software has been provided with a set of status-check tools, in order to assure proper working even in the case of temporary power shortages.

Data acquired on site are in the form of two sets of contemporary files; one set contains wind and temperature data in the format allowed by the acquisition routines provided with the anemometer, while the other contains concentration data, in the form of raw number counts, split per particle size, according to the gain of the MCA (i.e., the larger the gain, the larger the number of sizes sampled). Each file contains 30min of data. A post-processing software, developed in FORTRAN 77/90, checks data for validity and manages the two datasets, in order to create suitable input files to the software for flux computation, according to EC theory. This software, named CODY, is a brand new EC processing software also written in FORTRAN 77/90; it performs the typical steps of the EC methodology, as standardized in the framework of GHG fluxes measurement, i.e.:

- *time lag detection* by means of a maximum-covariance analysis;
- *data alignment* according to the time lag.
- *de-trending* to eliminate possible long-term trends affecting data and make them fit the steady-state hypothesis (Gash and Culf, 1996)
- *calculation of variance/covariance* among all variables
- *2D/3D/Planar Fit axis rotation* to align the x axis to the mean wind direction and nullify the covariance between v and w (Aubinet et al., 2001; Kaimal and Finnigan, 1994).
- *flux calculation* for each of the 18 sub-ranges available and derivation of PM_1, $PM_{2.5}$ and PM_{10} fluxes by summation of relevant sub-ranges (van Dijk et al., 2004).
- calculation of turbulence parameters such as Monin-Obukhov length, friction velocity and sensible heat flux.

The full set of collected output comprises:

- instantaneous (5Hz) data of 3-components wind speed
- instantaneous (5Hz) data of air temperature
- instantaneous (5Hz) data of number, surface, volume and mass particle concentration for the 18 sub-ranges
- mean data (averaged over a user-defined time period) of wind, temperature and concentrations
- standard deviations and auto/cross-correlations of wind, temperature and concentration data
- net (emission less deposition), 30-min averaged, vertical particle fluxes for each of the sub-ranges
- aggregated PM_1, $PM_{2.5}$ and PM_{10} net, 30-min averaged, vertical fluxes
- friction velocity, Monin-Obukhov length, heat flux.

4.3 The Wind Erosion Assessment Model (WEAM)

The WEAM model was developed by H. Lu and Y. Shao (Lu, 2000; Lu and Shao, 1999; Shao, 2001), moving from well-established relationships after Bagnold (1941), Owen (1964) and later revisions. Bombardment by saltating particles, or sandblasting, is assumed to be the ultimate source of finest particles emission. Accordingly, the amount of dust released either from saltating aggregates or from the surface depends on the individual kinetic energy of bombarding particles. Dust emission estimations are then based on the volume removed by impacting grains. For convenience, we briefly recall here the main equations of the model. Following Lu and Shao (1999), WEAM predicts size-dependent dust fluxes *F(d)* as:

$$F(d) = \frac{0.12 C_\alpha g f \rho_p}{p} Q(d) \qquad (4.13)$$

where d is the particles diameter (m), *Q(d)* ($gm^{-1}s^{-1}$) is the size-dependent horizontal flux of saltating particles, C_α is a coefficient of order 1, g is the gravity, f is the total volumetric fraction of dust in the sediment, ρ_p is the bulk soil density (g cm^{-3}) and p (N m^{-2}) is the soil penetration resistance. The horizontal flux Q can be modelled as (Owen, 1964):

$$Q(d) = \begin{cases} (c\rho u_*^3 / g)[1 - (u_{*_t}(d)/u_*)^2] & u_* \geq u_{*_t}(d) \\ 0 & u_* < u_{*_t}(d) \end{cases} \qquad (4.14)$$

where the coefficient c is of order 1, ρ (g cm^{-3}) is the air density, u_* (ms^{-1}) is the actual friction velocity, while u_{*_t} (ms^{-1}) is the threshold friction velocity. These latter parameter describes soil erodibility and thus depends on soil surface features. It can be simplified as (Shao and Lu, 2001):

$$u_{*_t} = u_{*_{t0}} \cdot R \cdot H \tag{4.15}$$

In Eq. (4.15), $u_{*_{t0}}$ is an uncorrected threshold friction velocity, while the correction factors R, H and account for major influencing features, namely surface roughness elements and soil moisture, respectively. Surface aggregation and crusting is also believed to play a major role in wind erosion, but their influence has not been modelled satisfyingly so far, thus we will neglect such parameters.

Finally, total vertical fluxes for a given range are calculated by integrating Eq. (4.14) over all the saltating, sandy-sized particles and Eq. (4.13) over the range of interest. In this application, only suspension of particle with aerodynamic diameter lower than 10 μm was considered for a direct comparison with fluxes measured by EOLO.

To accurately set all the input parameters required by Eqs. (4.13-15) with the purpose of a detailed comparison, field data were acquired in the investigated sites during the monitoring periods. It assured full comparability between modelled and measured flux data.

A total of 40 plots was sampled for the five sites concerned. The sampling squares (10x10 m for soil and 30x30 m for vegetation) were placed about 300-400 far from the EC system along the cardinal directions, to assure that sampled soil falls within the most relevant portion of its footprint.

In the following sections, details of the model implementation are provided to highlight main steps followed in model parameterization. For this specific case study, we attempted to take into account temporal variability of most relevant inputs, to obtain results that are as much as possible comparable with EOLO measurements.

4.3.1 Correction factors for threshold friction velocity

Soil moisture

Moisture content was measured for both undisturbed samples of the first 2.5 centimetres of soil and for disturbed samples of the first centimetre. However, these two parameters were observed to differ strongly, sometimes up to 90%. It is worth saying that moisture content is a key parameter for assessing water role in particle interspaces (Fècan et al., 1999) and the model has been proven to be highly sensible to its value. Several studies (Ravi, 2001)

suggest that wind erosion is mainly affected by the highly variable moisture content of the first few millimetres, whose primary source is atmospheric humidity. Wind tunnel tests (Gregory and Darwish, 1990) showed that atmospheric humidity plays an important role in determining moisture content at the soil surface, where wind indeed exerts its stress. This dependence from air humidity is significant especially in arid environments and seasons. Accordingly, we attempted to model soil moisture *w* for more superficial soil (few millimetres) on the basis of the air relative humidity (*RH*). From the latter parameter, the soil matrix potential (Ψ) is derived from the following theoretical relation:

$$\Psi = \left(\frac{RT}{M}\right) \cdot \ln(RH) \tag{4.16}$$

where *R* is the gas constant (8.31 J/mol K), *M* is water's molecular weight (g) and *T* the absolute air temperature (K). Then, we inverted the empirical relation in (Gardner, 1970) to derive volumetric soil moisture from matric potential (ψ):

$$\Psi = a \cdot w^{-b} \tag{4.17}$$

where *a* and *b* are parameters depending on the soil type (Saxton et al., 1986).

Although many studies about the effect of sediment water content on aeolian transport related such dynamics to the water content (*w*) on a volumetric bases (m^3/m^3), this parameter does not contain information on how tightly the water is held by the soil. However, Chepil (1956) and Chen et al. (1996) consider inter-particle forces developed by the adsorbed water film being much lower than inter-particle capillary forces. Capillary forces, which are referred to as the *water potential* (*w'*), induce a reinforcement of cohesion and are more closely associated with soil texture and structure; indeed the water potential around the grains is negligible for sands and increase with clay fraction content, following a second order polynomial equation (Fècan et al., 1999):

$$w' = 0.14(clay)^2 + 0.17(clay) \tag{4.18}$$

Thus, in this study the soil moisture enlargement factor *H* for the was parameterized as:

$$\begin{aligned} H &= 1 && for\ w < w' \\ H &= \left[1 + 1.21(w - w')^{0.68}\right]^{0.5} && for\ w > w' \end{aligned} \tag{4.19}$$

Effect of surface roughness by non-erodible elements

Vegetation has a twofold role in protecting soil from wind erosion: it absorbs a part of the wind momentum flux by increasing surface roughness (Stockton and Gillette, 1990) and protects the soil surface from erosion by direct sheltering. However, in this work, we will

show how, in suitable conditions, particular vegetation patterns might have an overall opposite effect and promote soil erosion (Sect. 5.4.2).

Soil erosion also depends on the presence of clods, rocks, crop residues etc. (Raupach et al., 1993), that can be treated together as non-erodible elements. Experimental studies showed that wind erosion thresholds observed on rough surfaces are significantly higher than those observed on smooth surfaces (Gillette and Stockton, 1989). Thus, also amount, stability and geometry of aggregates on the surface is a major factor affecting susceptibility of soil to wind erosion.

The impact of roughness elements on threshold wind friction velocity (R) was modelled, following Raupach et al. (1993), as:

$$R = \sqrt{(1 - \lambda\sigma)(1 + m\beta\lambda)} \tag{4.20}$$

where the first term of the product accounts for coverage, while the second accounts for drag; λ is the roughness density, σ is the basal to frontal area ratio (commonly assumed to be 1); m is a parameter indicating uniformity (if 1) or non-uniformity (if <1) in the surface stress: m=0.5 was here assumed; β is the ratio of the drag coefficients of roughness element over that of the bare soil, $\beta = C_R/C_S$. Numerous studies (Crawley and Nickling, 2003; Raupach et al., 1993) assessed β at about 90-100 for vegetated surfaces and 1 for bare soils (Okin and Gillette, 2004); these values were also used here.

Soil cover by non erodible cover

Non erodible surface cover includes any material lying on the soil surface, protecting it from the wind stress and from the impact of saltating grains. In several models, non erodible surface cover includes coarse rock fragments and flat lying plant residues. Generally, it is assumed an exponential decrease in soil loss with increasing surface cover (Bilbro and Fryear, 1995). An automatic image analysis procedure was developed and used to estimate soil cover by nadir-view photographs taken on site, to account only for particles greater than 2 mm and for both flat and standing vegetation cover. The method consists in the automatic detection of elements by means of a sequence of image processing steps (including *edge detection*, *smoothing*, *de-speckling*, *filtering*) carried out with the *Image J* software (freely available at http://rsb.info.nih.gov/ij/). Particle densities was determined by means of a picnometer-based standard procedure (ISO/TS, 2004).

4.3.2 Data collection for model application

With the aim of a direct comparison between EOLO results and WEAM predictions, we carried out a data collection campaign for model parameterization. Model input parameters had to be assessed in the same sites and at the time of the monitoring with EOLO, in order for the comparison to be as much reliable as possible. Main input parameters to WEAM are: *i.* the size distribution of soil particles; ii. soil cover by non erodible elements; iii. soil water contents; iv. surface roughness; v. particle densities (*in situ* and solid)

A total of 4 disturbed soil samples were collected for soil texture analyses. About 64 distribution classes, from 0.339 to 2000 µm were obtained by size analysis through laser diffraction technique, after dispersion of the sample in a 2‰ sodium hexametaphosphate solution $(NaPO_3)_6$.

Following Lu and Shao (1999) a linear combination of minimally and fully dispersed particle size was considered to define the overall size distribution:

$$p(d) = \gamma p_f(d) + (1-\gamma) p_m(d) \tag{4.21}$$

where $p(d)$ is the suspended particle size distribution and $p_f(d)$ and $p_m(d)$ are the fully and minimally soil particle size distribution, representing true and *in situ* distribution, respectively; γ is the weighting factor (depending on u_* and u_{*_t}) that approaches zero in case of weak erosion and unity in case of strong erosion (Chatenet et al., 1996; Gomes et al., 1990; Shao, 2001). $p_m(d)$ and $p_f(d)$ were computed by means a mixture distribution analysis, considering each distribution as the result of two or more log normal populations, according to:

$$p(d) = \frac{1}{d} \sum_{i=1}^{n} \frac{w_i}{2\pi\sigma_i} e^{\left(-\frac{(\ln d - \ln D_i)^2}{2\sigma_i} \right)} \tag{4.22}$$

Here, d is the diameter, n is the number of modes, and σ_i, D_i, and w_i are the standard deviation, the median and the weight of i^{th} distribution, respectively. Log-normal particle size distributions $p_f(d)$ and $p_m(d)$ were assumed (Udden, 1914; Wentworth, 1922), constituted by several populations. MIX3.1 (MacDonald and Green (1988), http://icarus.math.mcmaster.ca/peter/mix/mix.html) was used to perform sediment analyses of populations. Mode, fraction and standard deviation of such populations were implemented in the model for fully dispersed distribution. As for the minimally dispersed distribution, these parameters were estimated by comparing soil texture with those derived from previous studies (Marticorena et al., 1997; Shao et al., 2002), taking into account that

minimally and fully distributions are likely to be very similar, because of the negligible clay content at the Gobi sites.

4.4 Investigated sites

The first monitoring campaigns with EOLO have been carried out in the framework and with the financial support of the WinDust project. These lasted some four months (May-June 2005 and April-May 2006) and interested a total of ten sites, all located in northern China. We report here only the five sites whose data have been used for the purposes of this thesis. Site locations are shown in Figure 4.3 and their main characteristics, in terms of soil type and cover, summarized in Figure 4.4. Sites can be separated in: *i.* "desert sites" in the Alashan Prefecture of Inner Mongolia Autonomous Region and *ii.* "anthropogenic sites", comprising agricultural fields and rubble pits, in the Beijing Municipality.

The western Inner Mongolia Plateau (Alashan desert) is a ground surface of Gobi, alluvial and lacustrine sediments. The Alashan desert includes the Badain Jaran desert, the Tengger desert, the Ulan Buh desert and the Hexi Corridor. It can be considered as the southern extension of the Mongolian Plateau. The Southern Mongolian/Northern China Gobi shows extremely desolate landscapes, where neither vegetation nor animals can survive because there is no surface or underground water at all (Xuan et al., 2004). Annual precipitation in the regions can be as low as 10-50 mm/yr, the lowest values being registered in the Tengger and Badain Jaran deserts.

Among the "desert sites" we can further distinguish between Gobi sites in the Ejin'a county, representative of natural conditions, and the Air-Sowing site, in the Alxa Zuoqi county, representative of a large-scale reforestation intervention in a desert area. Ejin'a Banner county is located in Northwest Inner Mongolia, within an area of 102000 km^2 and an altitude of 898-1598 m above sea level. The area is topographically high at the edges and low in the middle, and descends gradually from NE to SW (the slope is about 0.1 %). There is a large inland river, the Heihe River, flowing across the region with a length of 250 km and developing the famous Ejin'a Oasis at its lower reaches (South). The surface is characterized by high variability in soil texture (coarse to fine grained clastic and clay beds), of alluvial origin. This area has a very hot climate in summer and cold in winter. Mean wind velocity averages 4.2 m/s, with peaks of 20 m/s. The annual average precipitation is 37 mm, against an annual potential evaporation of 3841.5 mm. In the oasis there are natural and artificial forests consisting of *Populus diversifolia*, *Elaeagnus angustifolia* and *Haloxylon ammodendron*. This area belongs to Central Asia sandstorm

area, that in the past was characterized by a landscape of rivers and lakes, but now, because of over exploitation, it is at risk of desertification: indeed old rivers and lakes dried up and forest areas are decreased. Two sites (GB1 and GB2) were selected in this area. The GB1 site, which is flat and highly homogeneous, is characterized by bare, Gobi soil where only sparse shrubs are present: *Nitraria sibirica, Ephedra sinica, Caragana stenophylla, Phragmites communis, Peganum harmala.*. The short vegetation is partly covered by small, sandy dunes extending downwind. These originated from deposition of sand and dust transported during previous storm events. Due to this vegetation/dune pattern, soil here was considered as the superimposition of two distinct soil types: the "dune" and the "inter-dune" soils. The distinction arises when dealing with particle size distribution, soil moisture and soil cover by non erodible cover.

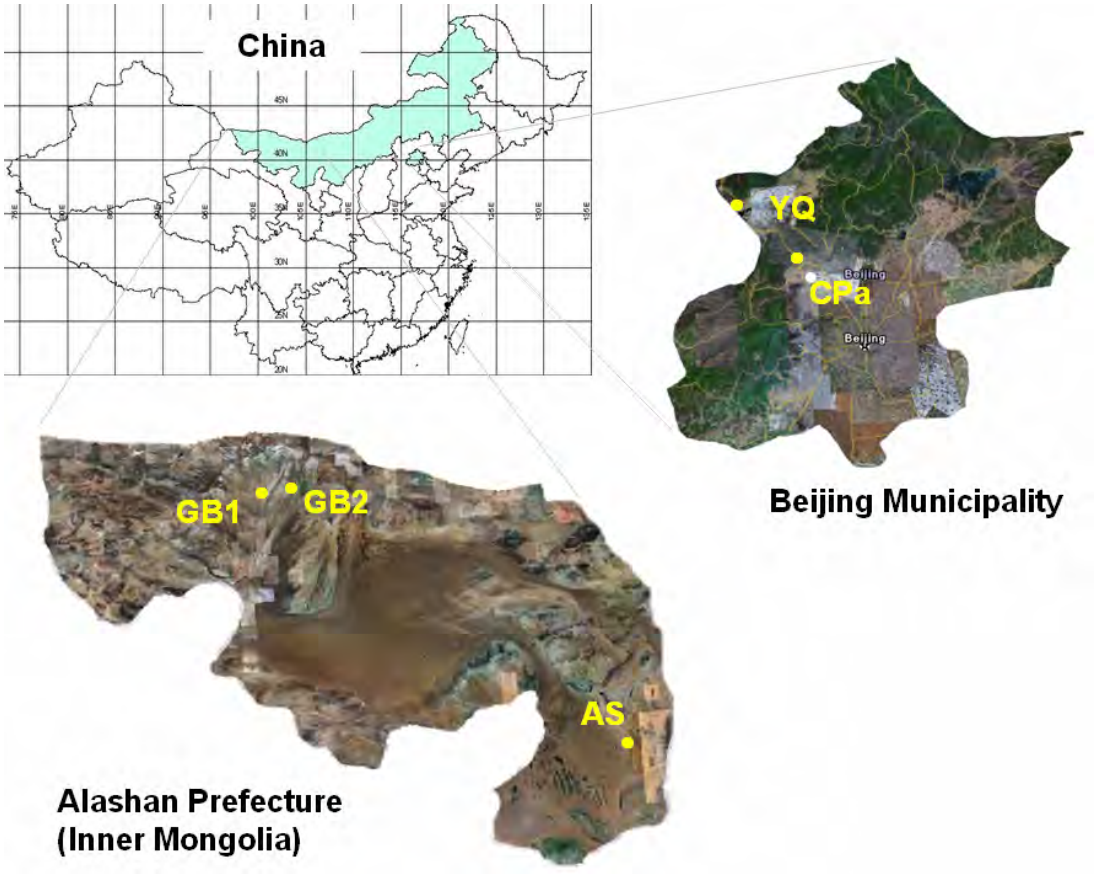

Figure 4.3. Location of sites where mineral dust fluxes were measured by EOLO and whose data are used in this thesis.

Alxa Zuoqi county is located at the easternmost fringes of Alashan Prefecture. It is bounded by the Tengger desert westward and by the Helan Mountains eastward. It mostly comprises arid sandy lands, with sparse and sporadic vegetation cover, mainly constituted by shrubs

(*Reamuria soongorica, Haloxylon ammodendron, Caragana stenophylla*). It is homeland to some 200.000 people living in two main town and a constellation of villages and isolated houses within the desert. Population exploits natural resources (such as wood and water) and attempt some agricultural activity (mainly maize and sunflowers), thereby stressing the delicate natural equilibrium of the region, possibly leading to enhanced desertification.

Site 1: GB1 (flat Gobi soil with natural shrubs)

- location: **100.53624°E - 41.88334°N**
- area**: Ejin'a**
- soil type: **gobi, flat**
- vegetation cover: **sparse shrubs with small dunes downwind**

Site 2: GB2 (flat and bare Gobi soil)

- location: **100.97517° E - 41.93814° N**
- area**: Ejin'a**
- soil type: **gobi, flat**
- vegetation cover: **none**

Site 3: AS (air-sowed sandy land)

- location: **105.60964°E - 38.86769°N**
- area**: Alxa Zuoqi**
- soil type: **sandy, irregular topography due to small dunes**
- vegetation cover: **dense shrubs, homogeneously distributed**

Site 4: CPa (conservation tillage spring maize experimental field)

- location: **116.40992° E - 40.18673° N**
- area**: Changping district (Beijing)**
- soil type: **silt, flat with small tillage roughness**
- vegetation cover: **standing and flat residues of maize**

Site 5: YQ (traditionally tilled spring maize field)

- location: **115.86301° E - 40,37107° N**
- area**: Yanqing district (Beijing)**
- soil type: **silt, with tillage roughness and sparse crop residues**
- vegetation cover: **mainly bare, with some crop residues**

Figure 4.4. Location, soil type and vegetation cover at all sites included in this thesis.

A site (AS) was selected in this county to monitor dust emission in an area of the Alashan desert interested by a long-lasting afforestation intervention by air-sowing. This activity, funded within the WinDust project and part of the 4th phase of the Three North shelterbelt

programme, is in progress in Alashan since 3 decades and involved the sandy lands at the eastern fringes of the Tengger Desert. Selected site is located within an area reforested several years ago (from 4 to 8). Sowed vegetation at the site was comprised of 3 main local shrubs: *Artemisia ordosica*, *Nitraria sphaerocarpa* and *Ephedra sinica;* secondary species present in the site were *Sancius branchyotus*, *Thermopsis schichkinii*, *Hedysarum fruticosum*, *Leymus chinensis*, *Ixeris chinensis*. Once again, topography is ideal for eddy covariance measurements, because the site is completely flat and vegetation mixed homogeneously.

With the aim of evaluating effectiveness of conservation tillage in mitigating wind erosion, we selected two agricultural sites in the Beijing Municipality. The first one (CPa), located in the Changping district (few tens of kilometres Northwest of Beijing downtown), is a spring maize minimum tillage experimental site. It is treated with low-tillage ploughs and sewers, with both standing and laying crop residues left on the field surface. The second one (YQ) is located in the Yanqing district, some 80 km Northwest of Beijing. This maize field is worked with traditional agricultural techniques, including deep ploughs, crop residues burning, etc. Both agricultural fields are flat and large enough (more than about 2 km in each direction) for the eddy covariance to be applied safely.

5
RESULTS AND DISCUSSION

In this Chapter, we report the first results obtained with EOLO. The first part of the Chapter focuses on the validation of the system and assessment of the uncertainties associated to fluxes. In doing this, we focus on the data collected at the GB1 site. Indeed, during monitoring in this site, a strong dust emission event occurred, classified at the Ejin'a meteorological station as a weak storm event. Meteorological, environmental and soil conditions at this site were particularly suitable for a careful analysis and a detailed comparison with the WEAM model. This comparison pushed us to explore the dependence of dust emission on wind direction, a dynamic that is seldom considered in natural environments. In the final part of the Chapter, we provide the first results obtained in the quantification of the emission reduction after mitigation interventions.

5.1 Validation of EOLO

The validation of EOLO followed two main streams. Because OPCs are not designed to measure at frequencies such as 5Hz, an evaluation of the concentration measurements was needed. Secondly, we quantified uncertainties in flux calculation due to particle counting. With an *a posteriori* approach, we also evaluated in which conditions measurements are representative of actual fluxes, by means of a spectral analysis.

5.1.1 Cumulated and size-segregated particle concentrations

Figure 5.1 reports the time series of total particle number concentrations ($\boldsymbol{N_{0.26\text{-}7.00}}$) recorded by EOLO at the GB1 site. Only one intense dust emission event was recorded during the whole monitoring campaign and it occurred in the last days of May.

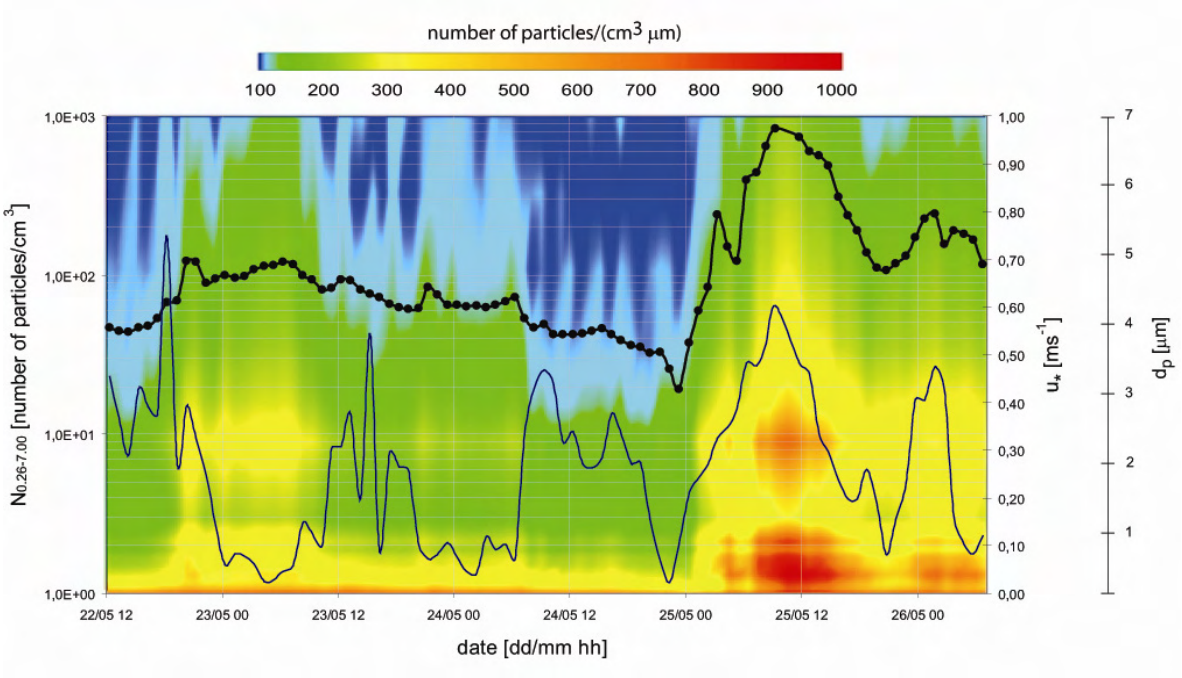

Figure 5.1. Time evolution of total particles number concentration sensed by EOLO ($N_{0.26\text{-}7.00}$, bold line with circles) and friction velocity (thin line) recorded from 22 to 26 May 2005 at the GB1 site, Ejin'a area. Concentrations are represented on a logarithmic scale. On the background, contour plot of size-segregated particle number concentration are also reported.

Particle number concentrations recorded during this event were one to two orders of magnitude higher than those recorded in previous days. Since no particle mass monitors were available at the site, a comparison was made with data from the Navy Aerosol Analysis and Prediction System (NAAPS) (http://www.nrlmry.navy.mil/aerosol/).

The model, described in Westphal et al. (1988) predicts 6-hour averaged data of mineral dust mass concentration smaller than 5.00 µm (aerodynamic diameter) at the surface layer. Model outputs have a sufficient spatial resolution to follow mineral dust evolution in the investigated area. Particle mass concentrations lower than 5.00 µm were obtained from EOLO by summing particle number contributions from all channels with an optical diameter smaller than ca. 4.00 µm and by converting these values into mass ($M_{0.26\text{-}4.00}$ in µg m^{-3}). Figure 5.2 compares the time evolution of particle mass concentrations predicted by the NAAPS model (a) with those measured by EOLO (b). Data refer to the storm event recorded at the end of May. Although the time resolution of the model did not allow to verify short-term variations, a good consistency was observed between the two dataset. This suggested that the bulk of mineral dust particles emitted in the area was falling inside the size-range sensed by EOLO. It is worth noting that the good agreement between measured and modelled values was not limited to this episode but was observed in almost

all sites in which the impact of anthropogenic sources was limited, regardless from the occurrence of desert storms events.

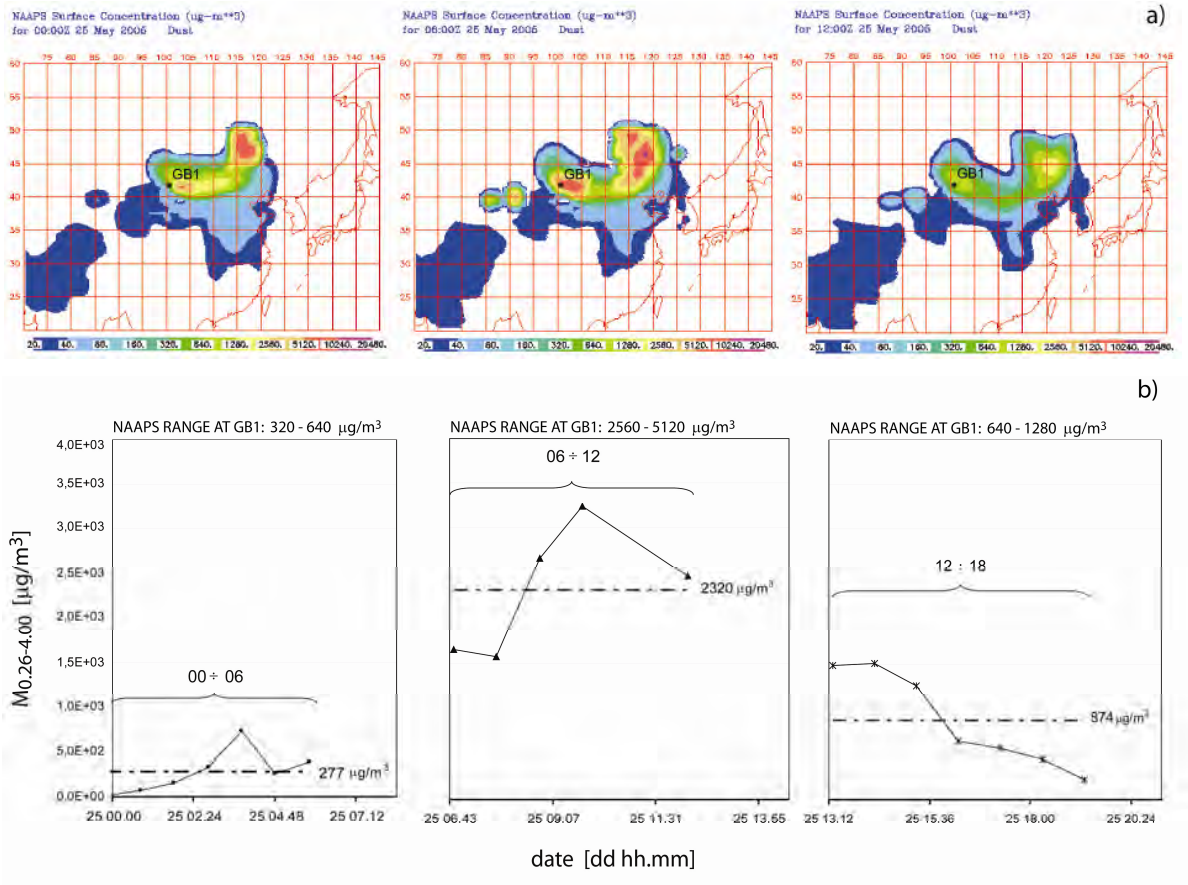

Figure 5.2. Mineral dust mass concentration during the strong dust event of 25 May 2005 at GB1 site: a) NAAPS "Dust" plots at surface layer; GB1 site location is also showed. b) mass concentration time series derived by EOLO. Units are µg/m^3.

Data obtained at the GB1 site during the event were also used to evaluate the evolution of mineral dust particles under high emission conditions. *N* and *V* values of particles recorded in the 18 size ranges investigated were separated into classes as a function of the friction velocity. Three classes, corresponding to average values of 0.15, 0.30 and 0.45 ms^{-1}, were selected for this analysis. In Figure 5.3a are reported data of size-segregated particle number concentrations, whereas volume concentrations are shown in Figure 5.3b. Solid lines with symbols were used to identify averaged values of profiles belonging to each class of the friction velocity. Dotted lines refer ,instead, to individual measurements. Although a general increase of *N* with the friction velocity was observed, the one occurring in the 0.40-0.60 µm range was suggestive of a substantial generation of finer particles above a certain value of the friction velocity. The release of these particles does not directly come from the wind action. Such particles are, indeed, so strongly attached to large, sandy grains, to form

a sort of permanent coating hard to be remove even at high wind velocities. Their release can be better explained by the sandblasting process induced by saltating particles (Shao, 2000). As shown in Figure 5.3b, trends of particle volume concentrations as a function of the friction velocity are quite different from those followed by particle number concentrations.

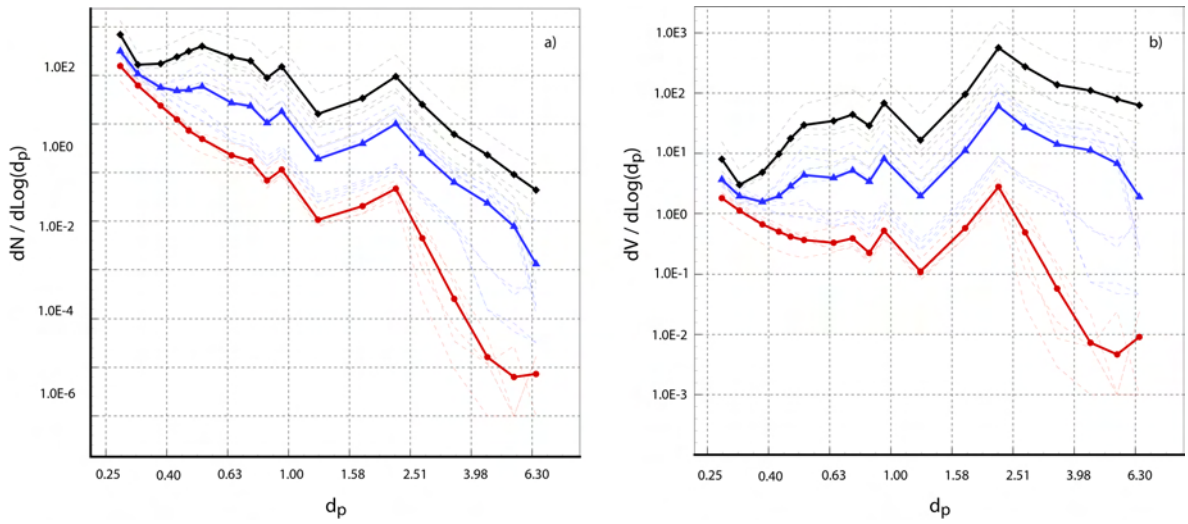

Figure 5.3. Number (a) and volume (b) concentrations vs. particle diameters during the dust event at the GB1 site. Units are [number of particles/cm^3] and [µm^3/cm^3] for the number and volume concentration, respectively; diameters are expressed in µm. Red, blue and black thick lines with symbols are the average profiles of the 0.15, 0.30 and 0.45 ms^{-1} wind friction classes, respectively. The highest wind friction class refers to the most intense period. Light, dashed lines are examples of profiles in the three classes.

Volume concentrations of coarser particles increase much more rapidly than particle numbers during the dust event. While in low turbulent conditions the contribution of finer particles ($V_{0.26\text{-}0.90}$) to the total volume is comparable to that of coarser particles ($V_{2.00\text{-}4.00}$), a larger increase in the coarser mode occurs during the dust event. It is such that the total volume concentrations can be considered to be almost exclusively formed by particles falling in the $V_{2.00\text{-}7.00}$ range. Size-segregated number concentrations feature a bi-modal behaviour of particles in the accumulation range (Figure 5.3a), with peaks approximately at 0.25 and 0.55 µm. While in the classical view of the accumulation range size distribution, only one peak occurs (see Figure 2.1), John and co-workers (1990) observed two peaks at 0.2 ± 0.1 µm and 0.7 ± 0.1 µm in a polluted urban environment. This bimodal character have also been observed during summer in Los Angeles (Hering et al., 1997). Our results suggest that such bimodal character in the accumulation range should be extended also to emissions in natural conditions. Indeed, our concentration measurements were carried out in clean-background conditions (desert environment) and at the time of emission; this

suggests that, when emission occurs for natural causes, the bimodal shape is a direct consequences of the erosion process and not a secondary effect of atmospheric chemistry or physics.

5.1.2 Co-spectral analysis

A co-spectral analysis was performed on the raw data in order to find out if *tc* effects were affecting the motion of particles falling in any size range. To focus attention on the vertical dynamics, co-spectra are calculated by using the vertical wind speed, *w*, as the transporting variable. Based on the classical theory of turbulence K41 (Kolmogorov, 1941), it can be assumed that trajectory crossing effects are negligible and data statistically valid whenever particle concentrations behave as passive scalars in the inertial frequency sub-range.

Different approaches can be used to find out if particles behave as an ideal scalar. The most used consists in comparing co-spectra of particles determined in the inertial sub-range with those theoretically expected (Martensson et al., 2006). Since theoretical calculations are only possible for specific turbulence conditions, such as neutrally stratified atmospheres (Stull, 1988), this approach in not the most appropriate when, such in our case, rapid changes in turbulence take place. In these conditions, a comparison between the normalized co-spectra of particles with those of an experimental variable known to be passively transported by the air flow represents a better option to analyze the concentration dynamics. If particles behave as a perfect scalar, their co-spectra should match those of the experimental variable in the inertial sub-range. In our case, co-spectral analysis was performed by comparing normalized co-spectra of particle concentration with those of the sonic temperature, which can be certainly assimilated to a passive scalar. Results obtained are summarized in Figure 5.4a and 4b, where data of regularized and normalized co-spectra of particle concentrations and sonic temperatures are plotted as a function of the normalized frequency f_n. This latter parameter is defined by $f_n = f * h_m / U$, where f is the frequency in Hz, h_m is the measurement height, (h_m =12 m) and U is the horizontal wind speed in ms^{-1}. In the figure, individual symbols are used to indicate co-spectra of particle mass concentrations in the various size ranges, whereas the continuous red lines refer to co-spectra of the sonic temperature. Data were obtained by processing individual datasets according to the following procedure: *i*. Hanning filtering; *ii*. Fast Fourier Transform; *iii*. raw co-spectra calculation; *iii*. raw co-spectra block averaging over exponentially-spaced frequency ranges; *iv*. as single datasets, each raw co-spectrum presents high levels of irregularity; thus, further local filtering (block-weighted average) was applied to highlight the main slopes; *v*. normalization by the variables covariance.

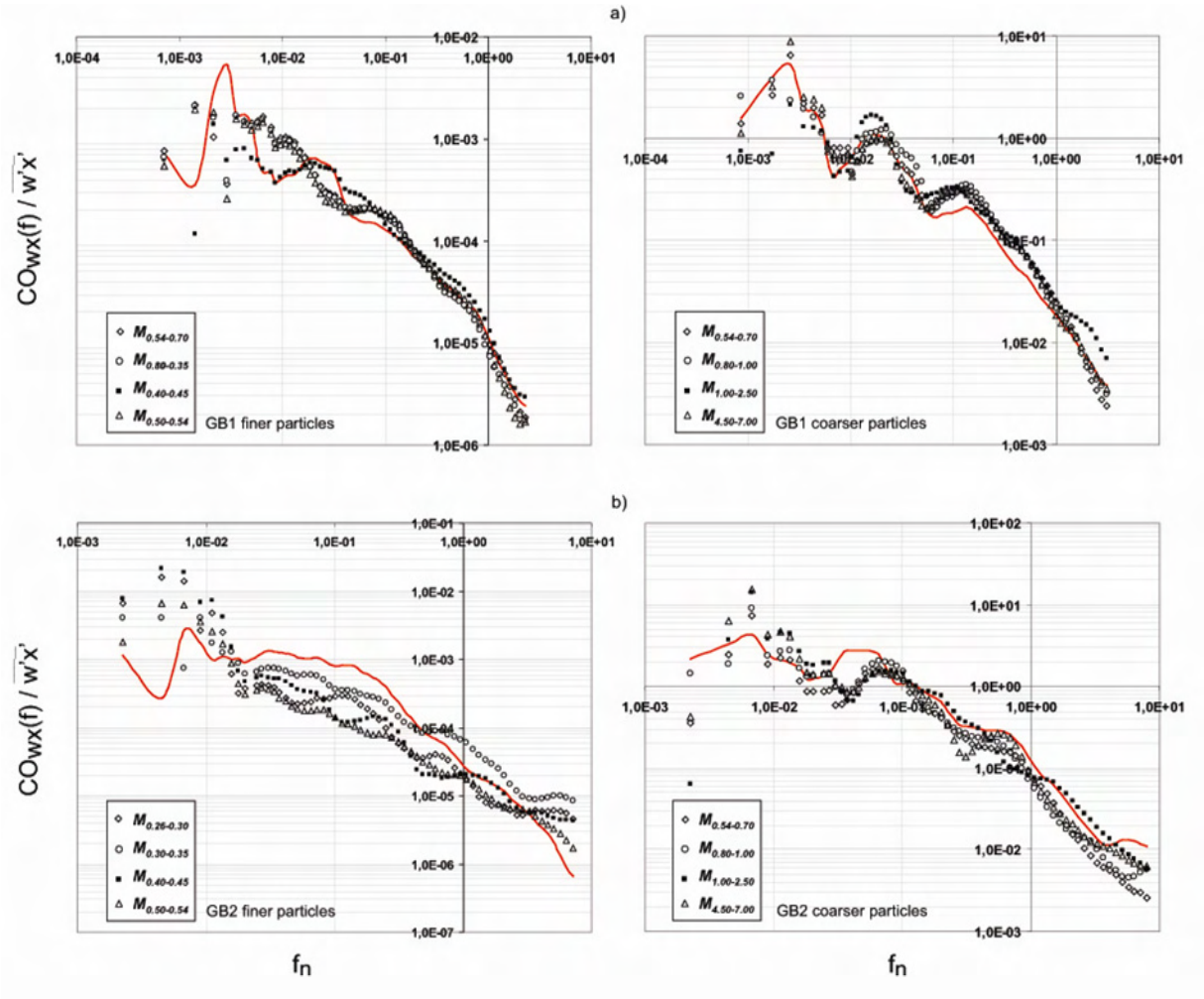

Figure 5.4. Normalized co-spectra of vertical wind and sonic temperature (red curves) and of vertical wind and particle concentration (symbols), as a function of the normalized frequency (U is used here to indicate the mean horizontal component of the wind speed). Plots refer to co-spectra of 30-minutes datasets for (a) a strong dust event at GB1 site and (b) a weak dust event at GB2 sites. The co-spectra of wind and sonic temperature is used as a reference.

Plots in Figure 5.4a refer to data recorded during the storm event of 25 May 2005, when the maximum particle mass concentrations were reached over the site and the average values of the wind speed and of the friction velocity were 13.9 and 0.6 ms^{-1}, respectively. Plots in Figure 5.4b refer to data collected on 28 May 2005 at the GB2 site, when particle mass concentrations were low and averaged values of the wind speed and of the friction velocity were 10.1 and 0.4 ms^{-1}, respectively.

Figures clearly show that under highly turbulent conditions (GB1 site), normalized co-spectra of both finer and coarser particles closely matched those of sonic temperature in the inertial subrange, that approximately extends beyond values of $f_n=1$. This suggested that in these conditions, *tc* effects were actually negligible and fluxes adequately described by the same equations used for gases. The same good consistency was not found at the GB2 site in

which low turbulent conditions occurred during the monitoring campaign. Deviations from a perfect scalar occurred in both the finer and coarser particle ranges. This does not necessarily means that *tc* effects affected our determinations, because other effects contributed to reduce the correlation between co-spectra of particles and those of the sonic temperature. The most important was associated with the fact that the instrument was specifically designed to measure particles during storm events, when high concentrations are reached. Under low turbulent conditions, indeed, particle number concentrations dropped down to values in which the dilution step drastically reduced the number of particles reaching the sensor and counts recorded were not always statically representative of the actual concentrations. In the next Section, we provide an estimation of the uncertainties in flux measurement due to particle counting.

5.1.3 Uncertainties in flux measurements with EOLO

According to Taylor (1982), uncertainty in flux calculations by EC can be expressed as:

$$\delta\left(\overline{wc}\right) = \sqrt{\sum_{i=1}^{N}\left[\delta\left(\frac{w_i c_i}{N}\right)\right]^2} \tag{5.1}$$

where, w_i and c_i are individual, high frequency vertical wind and concentration measurements and N is the total number of independent measurements in the averaging period (in our case, this is $N = 5Hz \cdot 30\min \cong 9000$). Symbol δ denotes the uncertainty for the quantity in parenthesis.

Buzorius et al. (2003) specified this expression for uncertainties when using a particle counters. Taking into account only the counting uncertainty (that is by far the most important), Eq. 5.1 becomes:

$$\delta\left(\overline{wc}\right)_{conc} = \frac{\sigma_w \bar{c}}{N_0} \tag{5.2}$$

where σ_w is the standard deviation of the vertical wind speed, $\bar{c}$ is the average concentration and N_0 is the total number of particles counted in the averaging period. All the parameters in Eq. 5.2 are available as size-dependent output from EOLO. Figure 5.5 shows time series of particle number fluxes and error bars for particles with mean optical diameters 0.28 μm and 3.50 μm, at the GB1 site; in the upper part of the figure, relative uncertainties are also plotted. As expected, relative uncertainty due to particle counting are large (100-1000%) in the first days, when measured fluxes were very small, and drop to values of 1-10% during the strong emission event of 25 May.

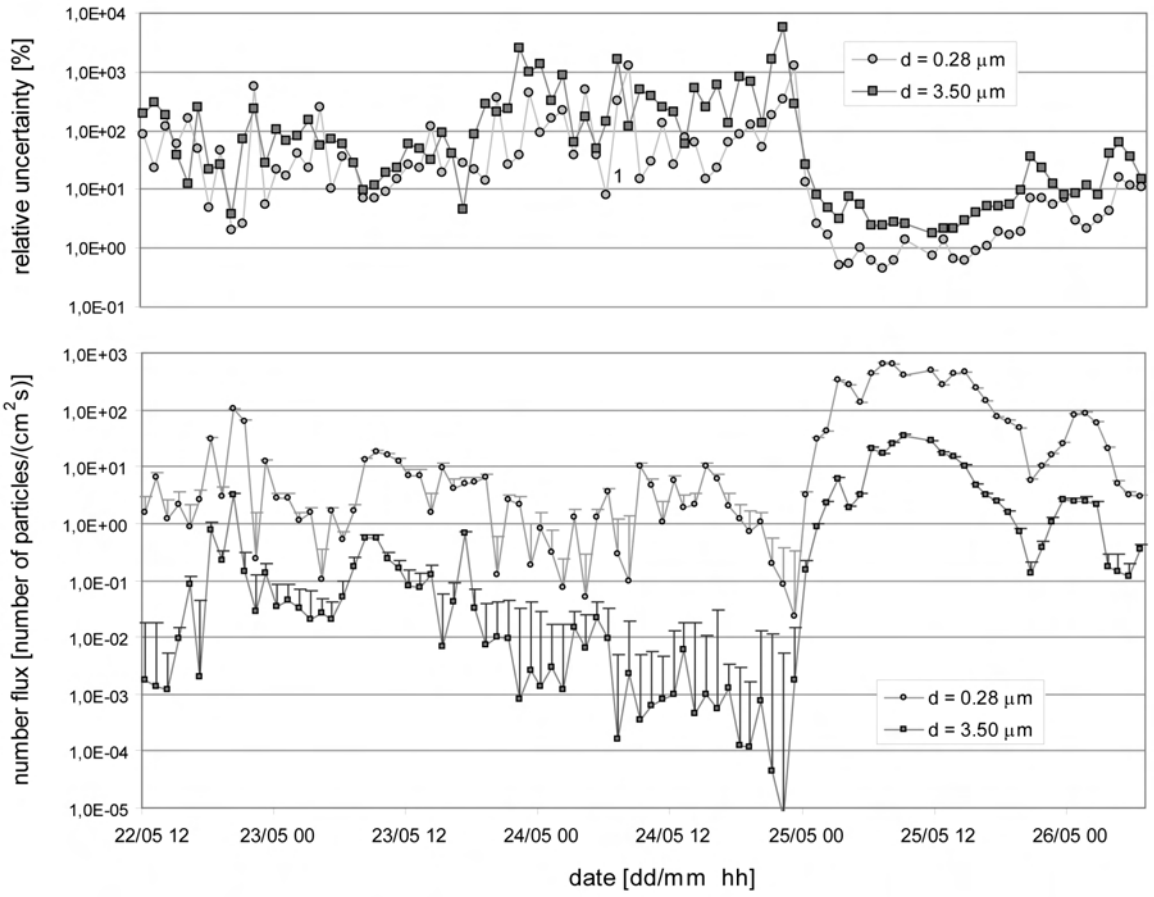

Figure 5.5. Time series of particle number fluxes for particles with optical diameters of 0.28 µm (light grey circles) and 3.50 µm (dark gray squares). In the upper plot, relative uncertainties for the same measurements are plotted with same symbols.

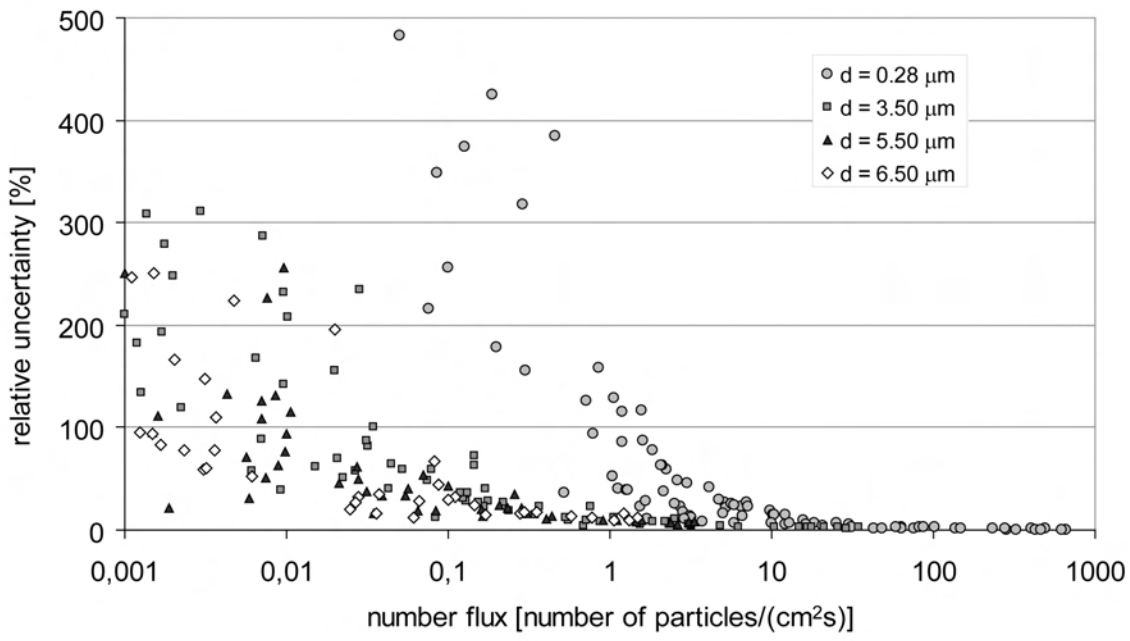

Figure 5.6. Relative uncertainties vs. particle number fluxes for several particles optical diameters.

Figure 5.6 shows a scatter plot of the relative uncertainty vs. number fluxes, for particles with average optical diameter up to 6.5 μm. A consistent trend is observed for all size ranges. The drop in relative uncertainty with increasing fluxes is due to the fact that, in this case, strong fluxes are associated with high concentrations. In the desert environment, in fact, high concentrations are likely to be due to dust emission by wind erosion: in this case they are thus necessarily associated with high fluxes. In other environments, however, we might observe high concentrations and small fluxes. For instance, this is the case of the urban environment, where high background concentrations are often observed even in case of no relevant emission/deposition fluxes. In this case, uncertainty in flux computation due to particle counting can be very small even associated to small fluxes.

One way to avoid high uncertainties at small concentrations and to evaluate sources leading to deviations of number concentrations under low turbulence conditions (Fig. 5.4b) the dilution step should have been avoided and whole sample sent to the OPC. Because of these limitations, we will focus our discussion on size-segregated fluxes of mineral dust to data collected during the storm event. Data collected under low turbulent conditions will be only used to provide a general idea of variations occurring over the site.

5.2 Dust emission during a storm event in the Gobi desert

By keeping in mind the considerations made above, fluxes measured by EC were first used to check if the gravitational settling was really negligible with respect to turbulent fluxes.

This was obtained by comparing the gravitational settling of particles falling in the coarser mode ($N_{0.54\text{-}7.00}$) calculated by using Eq. (4.9) with net fluxes measured by EC. The comparison was performed on data collected on the GB1 site. These are displayed in Figure 5.7. It is evident that gravitational fluxes were generally 1 to 2 orders of magnitude lower than net turbulent fluxes, and, in most of the instances, their contribution could have been neglected. Only sporadically, gravitational fluxes exceeded the turbulent ones. This happened when both the turbulence and particle number concentrations were small. In these cases, however, turbulent values were also affected by a large uncertainty.

The sequence of events that occurred at the GB1 site was also exploited to get information on the way how emission of mineral dust occurs in desert areas of northern China and to analyze what happens during storm events. Data reported in Figure 5.8 show that emission fluxes of total particle number concentrations ($N_{0.26\text{-}7.00}$) do not follow the same trend as the friction velocity. Although several periods were recorded in which high wind speeds and

friction velocities were reached during the monitoring period, only in the last days of measurement huge fluxes were measured.

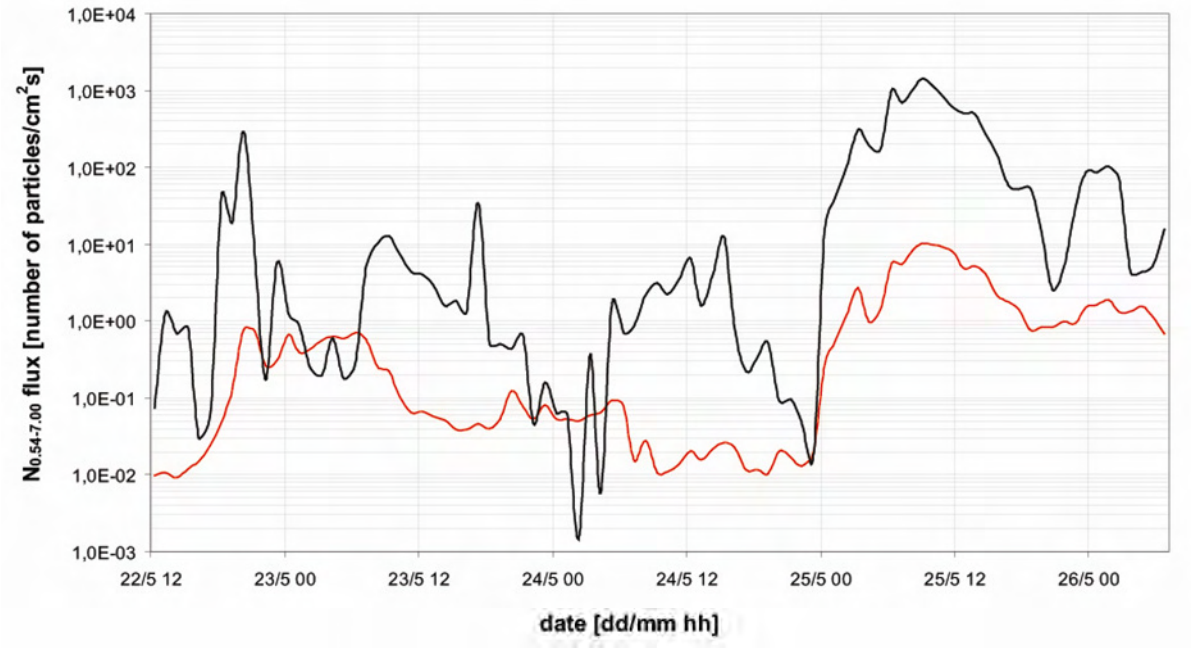

Figure 5.7. Time series of $N_{0.54\text{-}7.0}$ turbulent number fluxes (black line) vs. $N_{0.54\text{-}7.0}$ gravitational number fluxes (red line) during the monitoring period (22 – 26 May 2005) at the GB1 site. Fluxes are represented as absolute values, on a logarithmic scale.

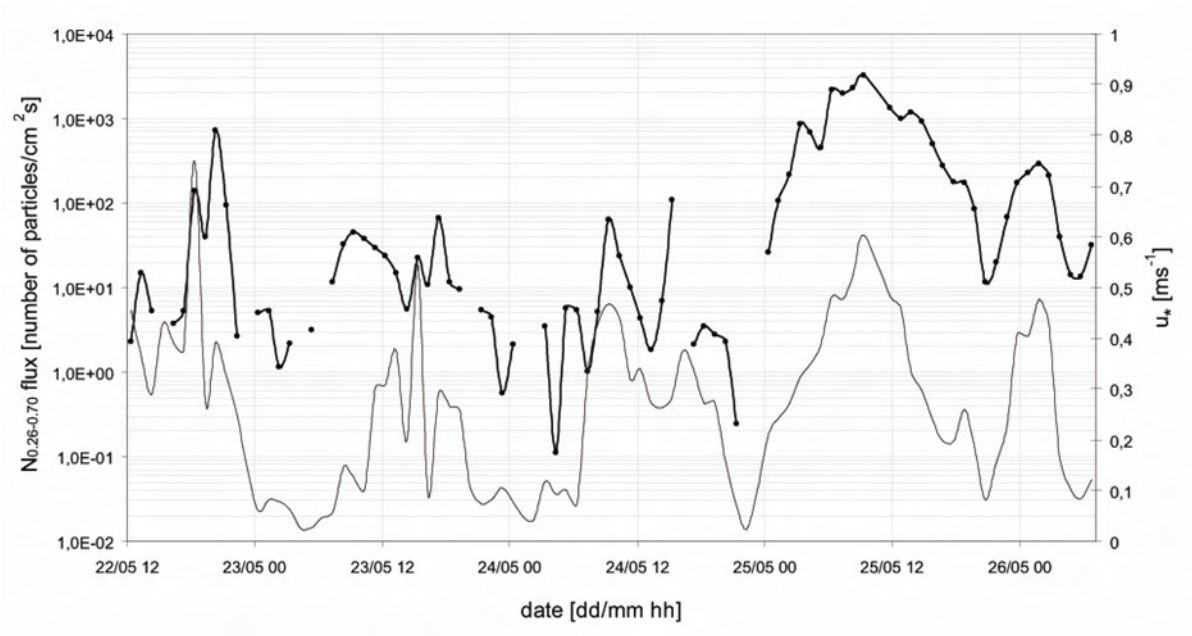

Figure 5.8. Time series of particles ($N_{0.26\text{-}7.0}$) number fluxes (bold line with circles) and friction velocity (thin line) during the monitoring period (22-26 May 2005) in the GB1 site. Fluxes are represented on a logarithmic scale; missing values relates to negative (net deposition) fluxes, that are not of interest in this thesis.

During this episode values as high as $3*10^4$ particles $cm^{-2}s^{-1}$ were recorded over the site. They were 1 to 2 orders of magnitudes higher than those measured in previous days under similar conditions in terms of wind speed and friction velocity.

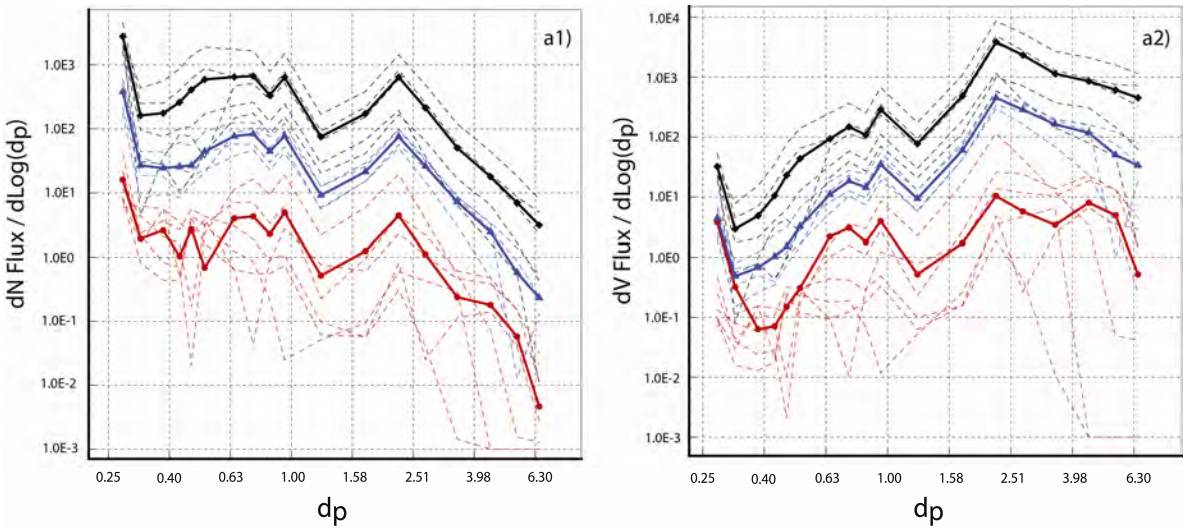

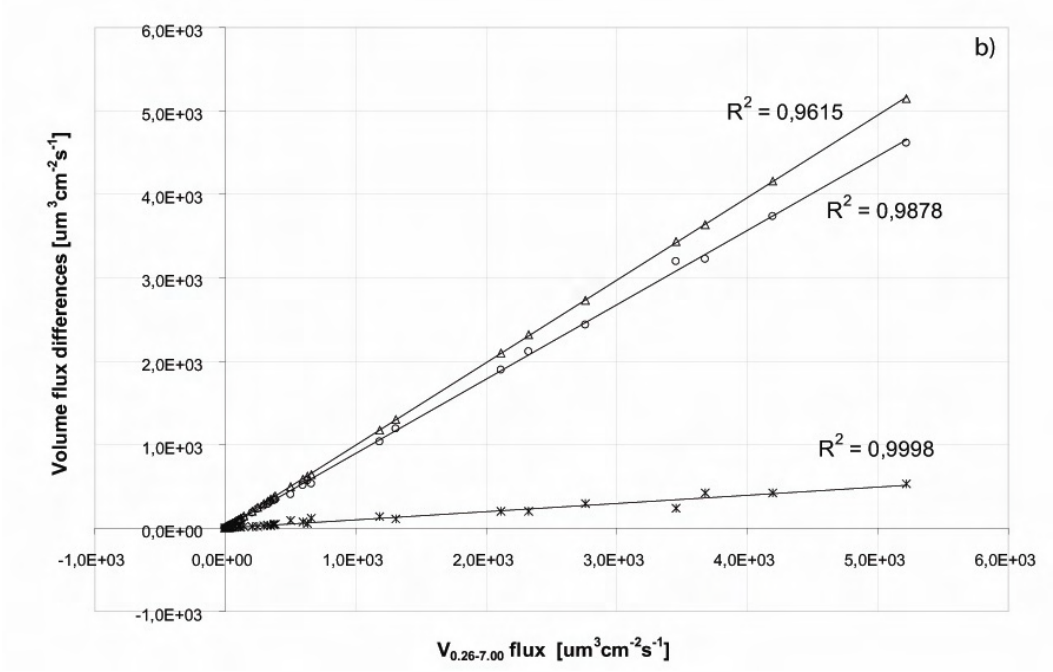

Figure 5.9. a) Particle number (a1) and particle volume (a2) fluxes vs. particles diameters during the monitoring period at the GB1 site. Units are [number of particles/cm^2s] and [$\mu m^3/cm^2$s] for the number and volume fluxes, respectively. Red, blue and black thick lines with symbols are the average profiles of the "low", "medium" and "high" friction velocity classes, respectively. The high friction velocity class refers to the most intense moment of the dust event. Light, dashed lines are examples of profiles in the three classes. b) Differences in volume vertical fluxes among $V_{0.26\text{-}7.00}$, $V_{0.26\text{-}1.85}$, and $V_{0.26\text{-}0.74}$; $V_{0.26\text{-}7.00}$ - $V_{0.26\text{-}0.74}$ (triangles), $V_{0.26\text{-}7.00}$ - $V_{0.26\text{-}1.85}$ (circles), $V_{0.26\text{-}1.85}$ - $V_{0.26\text{-}0.74}$ (stars) vs. $V_{0.26\text{-}7.00}$ net vertical flux, during the strong dust event at GB1 site; solid lines, linear regressions.

This is consistent with the fact that other parameters, such as wind direction, air humidity, particle density and the texture, cover, moisture content and roughness of soil, play an important role in the development of desert storm events. If we focus on the storm event we can see that particle fluxes behaved differently from concentrations, in the sense that no substantial changes in size-segregated flux profiles were recorded. Data reported in Figure 5.9(a1) indicate that the profile of particle number fluxes are always dominated by particles falling in the finer range ($N_{0.26\text{-}0.30}$) with two maxima peaking in the $N_{0.70\text{-}1.00}$ and $N_{1.50\text{-}3.00}$ modes. Above 3.00 μm of optical diameter, an exponential decay occurs in the particle number fluxes. In terms of particle volume (and particle mass), emission fluxes are, instead, definitely dominated by particles falling in the $V_{1.50\text{-}3.00}$ mode, with a small contribution coming from particles in the $V_{0.70\text{-}1.00}$ range, see Figure 5.9(a2). Overall, larger volume particles account for ca. 74% of the entire volume, whereas finer particles contribute only to ca. 7%. In terms of aerodynamic diameter, this means that net vertical fluxes generated during storm events are essentially given by particles falling in the $PM_{2.5}$-PM_{10} range. This represents a substantial variation with respect to low turbulent conditions , in which fluxes of coarser particle account for ca. 40% of the total volume and the finer ones for ca. 22%.

The relative importance of the $V_{0.26\text{-}7.00}$, $V_{0.26\text{-}1.85}$, $V_{0.26\text{-}0.74}$ modes in determining the total particle volume and their substantial constancy during storm events characterized by high particle emission is well illustrated in Figure 5.9b. The good correlations coefficients given by the linear regressions suggest that it is possible to estimate with good accuracy size segregated fluxes of mineral dust particles from their total fluxes expressed in terms of both mass and volume.

Data collected are also useful to better understand the role played by the wind speed in determining particle emission in acute episodes in which wind erosion and sandblasting are, by far, the dominant sources of mineral dust. Although several factors are known to affect particle generation in the wind erosion process, their assessment is rather difficult and, sometimes, controversial (Shao, 2000). This explains why many models still use relations between the friction velocity and particle fluxes to parameterize the emission process. Particle fluxes are usually related to the friction velocity through a power function, whose exponent was found to change from 6.54 to 1.89 (White et al., 1996), (Nickling and Gillies, 1989). Such large variations, that have been attributed to inter-particle bonds strength and/or crusting effects (Houser and Nickling, 2001), can introduce large errors in the models. Data collected during the storm event were particularly suitable to investigate this aspect because determinations were made when deposition fluxes were small when

compared to emissions and the emission process was essentially driven by wind erosion. Under these conditions, other effects, such as those arising from changes in the moisture content of soil, could have been neglected and the relation between particle emission and turbulence better assessed.

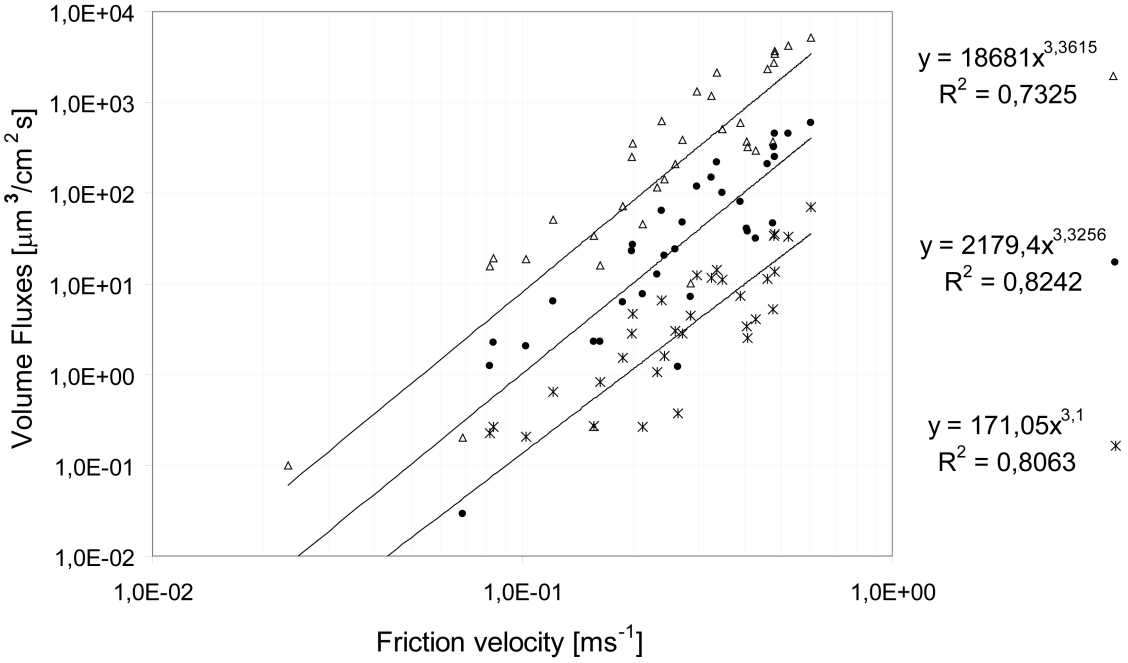

Figure 5.10. Net vertical volume fluxes of $V_{0.26\text{-}7.00}$ (triangles), $V_{0.26\text{-}1.85}$ (full circles), $V_{0.26\text{-}0.74}$ (stars) vs. friction velocity during the strong dust event at GB1 site; the three ranges roughly correspond to PM_{10}, $PM_{2.5}$ and PM_1 in aerodynamic diameter; solid lines, power regressions.

When particle volume fluxes in three size ranges (namely $V_{0.26\text{-}7.00}$, $V_{0.26\text{-}1.85}$, $V_{0.26\text{-}0.74}$) were plotted against the friction velocity, curves shown in Figure 5.10 were obtained. Power regression gave exponents ranging between 3.1÷3.36 with a r^2 of 0.732. It is much higher than those reported in previous literature (Houser and Nickling, 2001) in which r^2 values of 0.38 were reported. Since in the EC approach the friction velocity is derived independently from vertical dust fluxes, the good correlation displayed in Figure 5.10 is suggestive of a genuine physical dependence, and it does not seem to be just a spurious result of the calculations, as suggested, for example, in Houser and Nickling (2001).

5.3 Application of the WEAM model: input parameters

Particle size distribution and particle density

Main input for model parameterization (see Sect. 4.3) were derived from the soil samples collected and from *in situ* measurements. Of particular interested was the size distribution,

derived from soil samples with the procedure described in Sect. 4.3.2. An example of the result, derived for the GB1 and Gb2 sites, is reported in Figure 5.11. We recall that, for the purpose of a careful parameterization, GB1 site was considered as the juxtaposition of a "dune" and an "inter-dune" soil types.

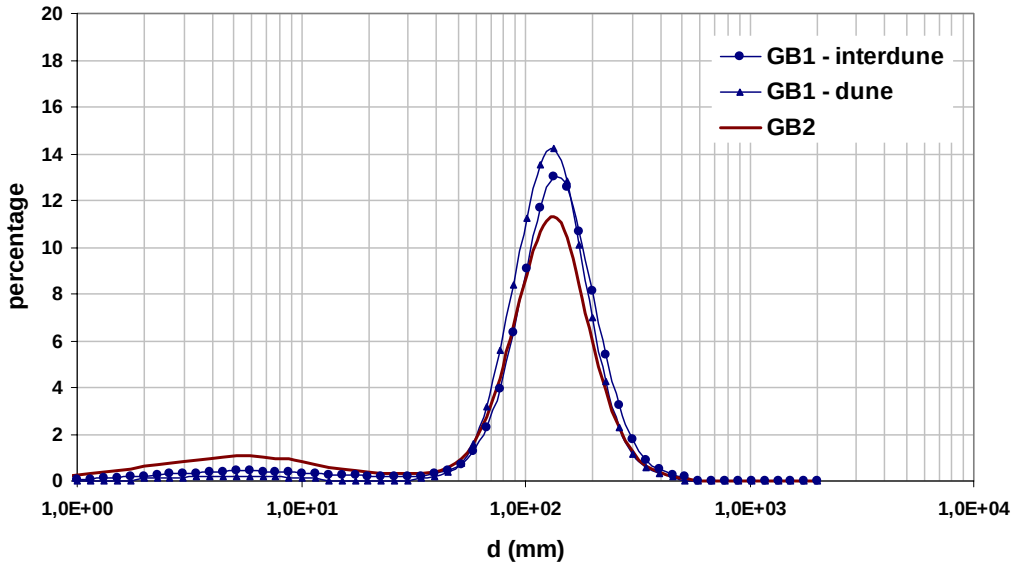

Figure 5.11. Size distribution of soil particles for GB1 and GB2 sites, as derived by soil sample analysis by laser diffraction. The "inter-dune" and "dune" soil types are shown separately.

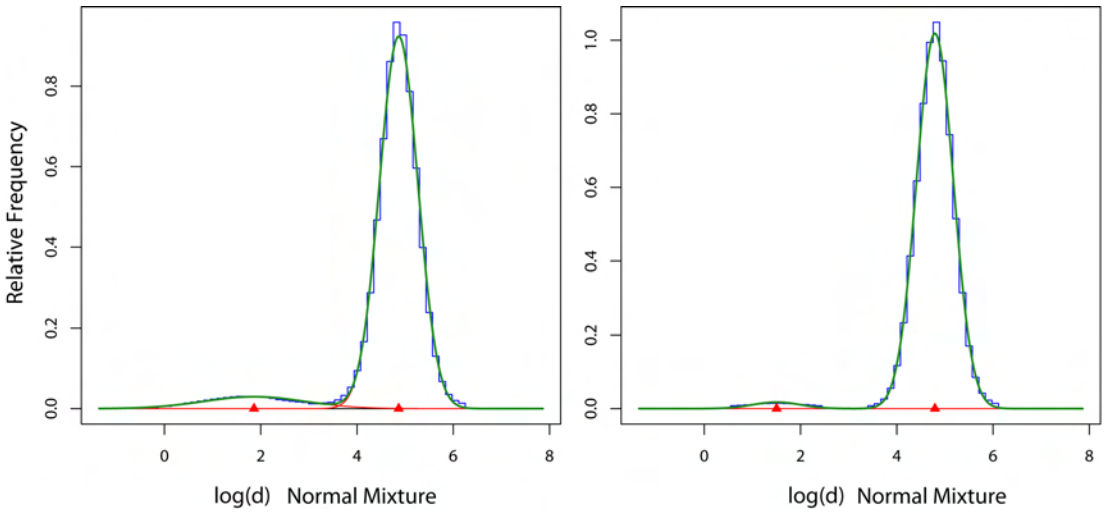

Figure 5.12. Minimally dispersed particle populations up to 2000 µm as reconstructed by MIX3.1 software for the "inter-dune" soil type (left-hand plot) and the "dune" soil type (right-hand plot), at the GB1 site.

Figure 5.12 shows an example of the size distribution of particles whose emission is considered in the model application, that is the size fraction measured by EOLO (up to ca. 10 µm) for the GB1 site. This is a weighted average of fully and minimally distributions

according to Eq. (4.21). In the figure, it is compared to the one derived by EOLO, for a friction velocity of 0.6 ms^{-1}.

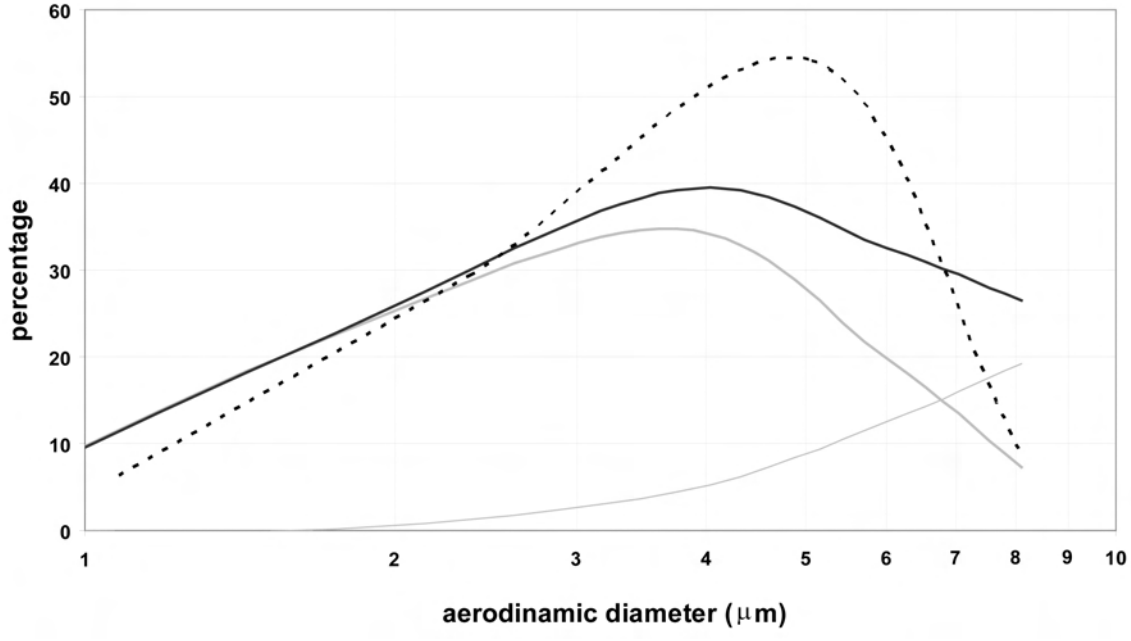

Figure 5.13. Size distribution of particles in the range 1-10 μm at the GB1 site for u_*=0.6 ms^{-1}. Light-gray thin line is the minimally dispersed, light-gray bold line is the fully dispersed and dark-gray bold line is the linear combination of the previous ones; dotted line is the distribution observed with EOLO.

		particle density (g/cm^3)		grave	sand	silt	clay
GB1	**AVR**	2,54	**AVR (%)**	46,65	48,75	4,14	0,46
	ST_DEV	0,07	**ST_DEV (%)**	14,02	14,2	0,47	0,31
GB2	**AVR**	2,48	**AVR (%)**	50,55	39,85	8,2	1,4
	ST_DEV	0,08	**ST_DEV (%)**	0,01	1,52	1,19	0,35
AS	**AVR**	2,45	**AVR (%)**	0	76,81	22,38	0,81
	ST_DEV	0,04	**ST_DEV (%)**	0	6,57	6,41	0,16
CPa	**AVR**	2,48	**AVR (%)**	0	43,76	55,75	0,49
	ST_DEV	0,13	**ST_DEV (%)**	0	7,83	7,68	0,22
YQ	**AVR**	2,48	**AVR (%)**	0	39,01	58,52	2,46
	ST_DEV	0,11	**ST_DEV (%)**	0	6,06	5,66	0,43

Table 5.1. Particle density and soil texture at all sites.

Figure 5.13 shows results of the application of the MIX3.1 software for determination of particle populations, obtained for the GB1 site. Mode, fraction and standard deviation of such populations were implemented in the model for fully dispersed distribution. Similar results were obtained for all other sites. Table 5.1 reports soil texture for all sites, together

with particle densities, determined by means of a picnometer-based standard procedure (ISO/TS, 2004).

Soil cover

Figure 5.14 shows an exemplary result of the application of the procedure set up for the automatic detection of soil cover by non erodible elements. Comparison with detections by visual inspection showed satisfactory agreements for both vegetation cover and cobble cover, with r^2 values of about 0.9 in almost all conditions. Table 5.2 summarizes the results of this task, reporting gross values of soil cover by non erodible elements.

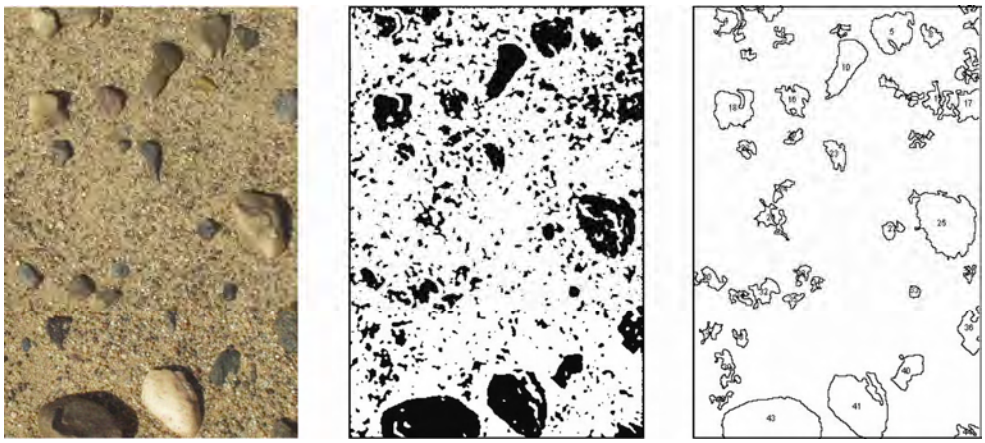

Figure 5.14. Main steps of the automatic procedure developed with Image J to assess soil cover by non erodible elements. Pictures refer to the Gobi soil at GB2 site.

site	soil cover by non erodible elements (%)		
GB1	23	**GB1 - dune**	30
		GB1 - interdune	22
GB2	25		
AS	30		
CPa	30		
YQ	24		

Table 5.2. Soil cover by non erodible cover as derived by the automatic procedure descript in Sect. 4.3.1.

5.4 Effect of natural vegetation: comparison between EOLO and WEAM

5.4.1 Time series of net fluxes

Figure 5.15 shows the time series of net mass fluxes measured by EOLO and simulated by WEAM, again at the GB1 site (22-26 May 2005). Despite several periods of high wind speed and friction velocity occurred at that site, that clearly follow a daily pattern, direct measures by EOLO only showed a strong burst of dust emission during May 25th,as already described in Sect. 5.1 and 5.2.

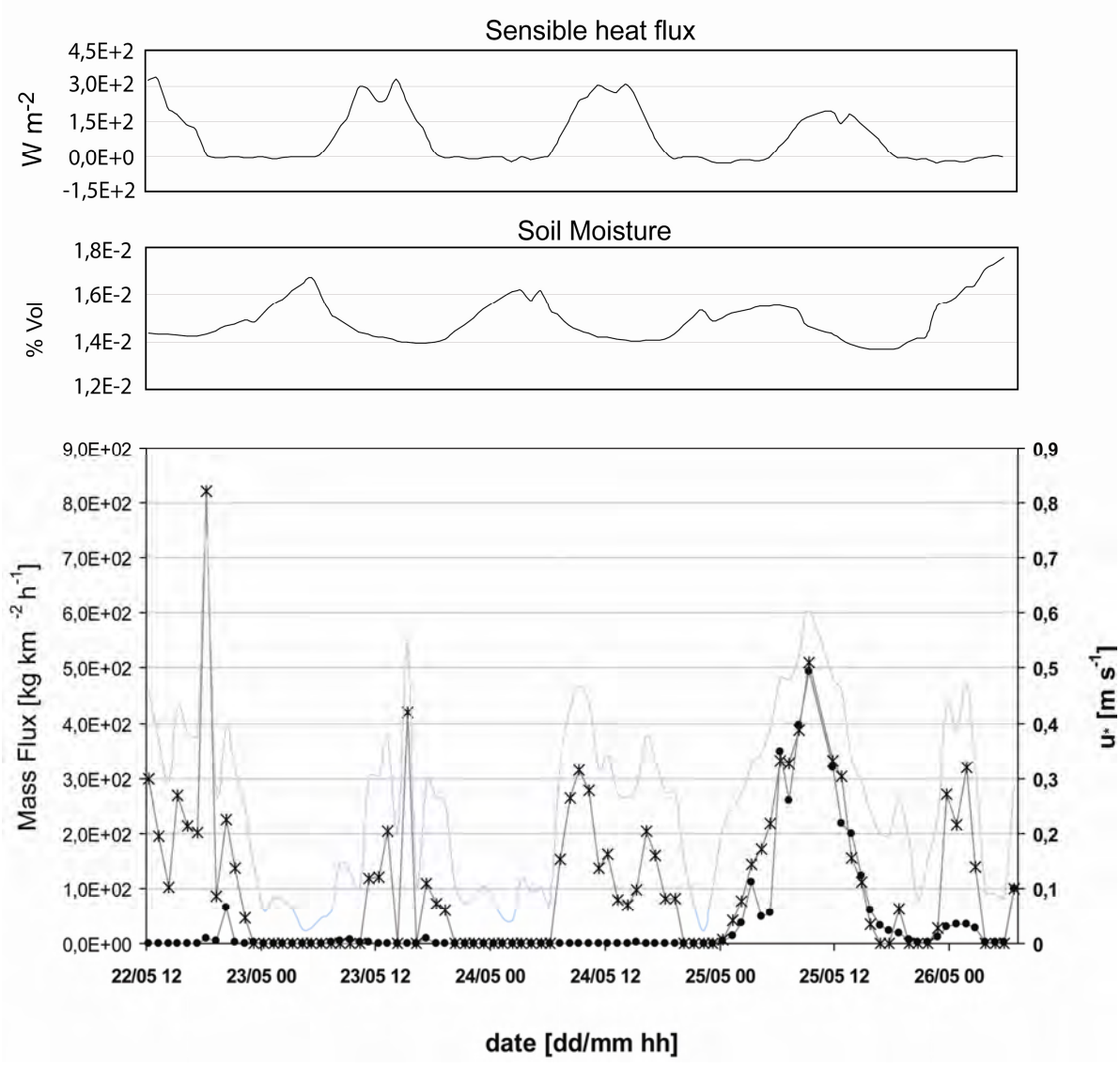

Figure 5.15. Time series of $M_{0.26\text{-}7.00}$ vertical fluxes measured by EOLO (black circles) and simulated with WEAM (black stars) for 5 days monitoring at GB1 site (22-26 May 2006). Light blue line is the friction velocity (right-hand scale). Also shown are the time series of sensible heat flux and soil moisture during the same period. The linear scale for fluxes highlights the intense event, classified as a weak dust storm, registered by EOLO during 25 May.

On the contrary, WEAM predicted several burst of dust emission, basically following the friction velocity patterns. It is worth saying that most of the time, the downward, deposition fluxes measured by EOLO (detected by the sign of the instantaneous vertical wind covariance) are negligible with respect to the emission fluxes; this is especially true during intense wind erosion. This makes EOLO net fluxes comparable with purely emissive fluxes predicted by WEAM. In the upper part of Figure 5.15, soil moisture and sensible heat flux time series are also shown. Soil moisture was calculated according to Eqs. (4.16-19). Sensible heat flux is an indicator of the turbulence intensity due to buoyancy effects; as such, it provides information on the erosion potential of the wind field. However, neither soil moisture nor sensible heat flux showed significant variations during the event, with respect to previous days. All other parameters taken into consideration in the model remained virtually constant during such short monitoring period; hence, they did not influence dust emission trends.

A general idea of the situation of dust at the surface level in the site area can be drawn again from Navy Aerosol Analysis and Prediction System (NAAPS) model outputs (http://www.nrlmry.navy.mil/aerosol/). As already mentioned the model provides estimations of mineral dust mass concentration smaller than 5.00 μm (aerodynamic diameter) at the surface layer; particle size distribution shown in Figure 5.13, suggests that there is no major difference between NAAPS and EOLO particles ranges, in terms of mass. Figure 5.16 shows a series of NAAPS outputs for the eastern Asia region, for the period 22-26 May 2005; the GB1 site is also indicated. As evident, model predictions show a general pattern similar to that described by EOLO; a more detailed comparison during the “dust event” of May 25th was shown earlier (Sect. 5.1), where the analogy is confirmed also by a quantitative point of view. Although no direct conclusions about fluxes should be derived by a mere observation of particle concentrations, both EOLO and NAAPS outputs make clear that WEAM overestimated emissions during 22nd-24th of May. On the contrary, during the storm event of 25 May emissions predicted by WEAM follow the fluxes measured by EOLO with an excellent agreement.

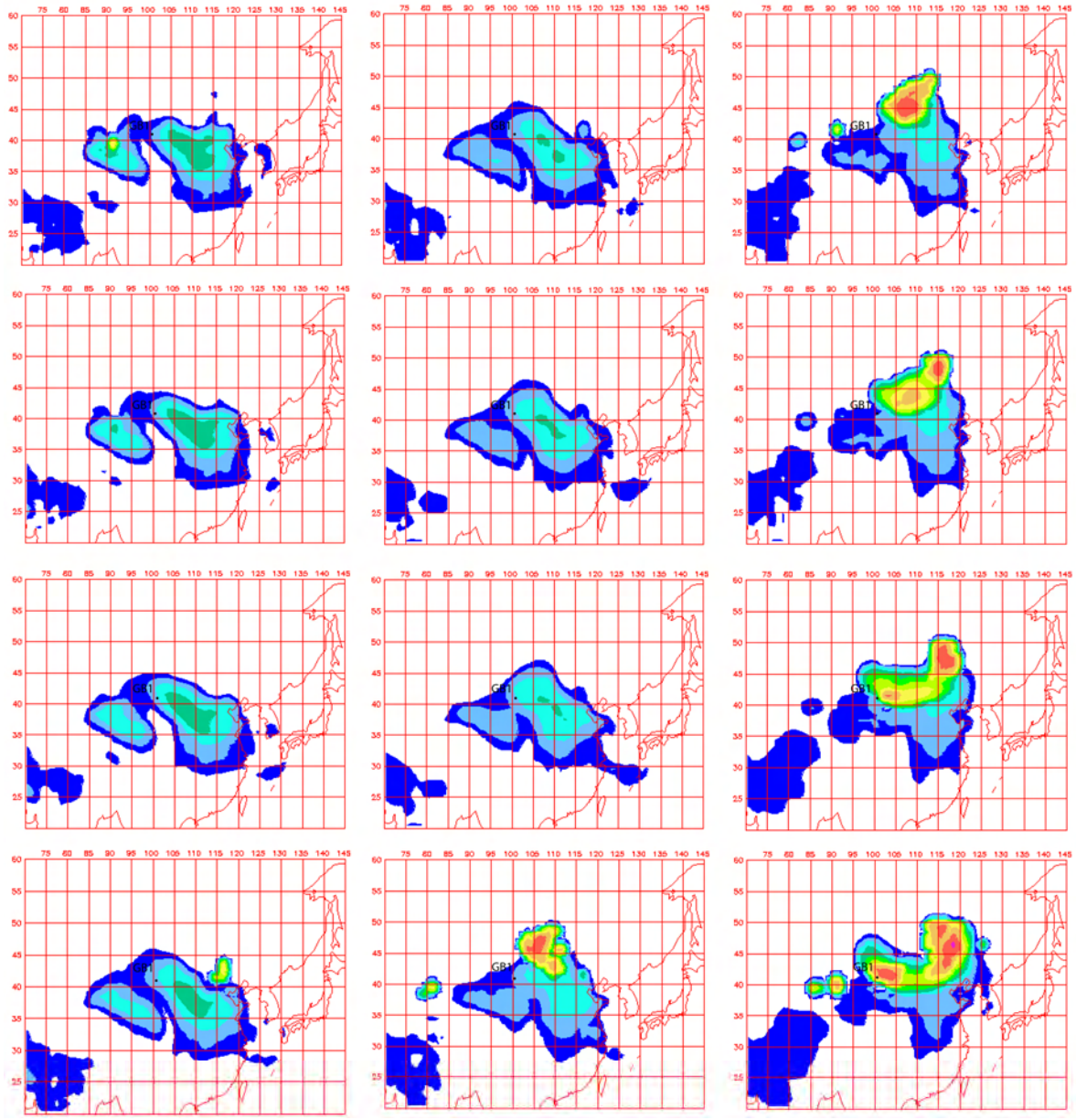

Figure 5.16. NAAPS dust output series at the surface layer for the eastern Asia region, from 22 to 26 May 2005. The series shows that, in terms of mineral dust concentrations, a strong event was foreseen by the model for the GB1 site region only during 25 of May. GB1 location is also shown in the plots

5.4.2 The effect of wind direction

An explanation for the discrepancies highlighted in the previous section might be related to the influence of wind direction with respect to surface anisotropies. As mentioned in Sect. 4.4, the GB1 site presents sparse shrubs, partly covered by small sand dunes extending downwind. These dunes originated from deposition of sand and dust transported during previous intense events; they constitute a well defined anisotropy of the surface. In Figure 5.17 the Gobi, “inter-dune” soil type and a landscape view at GB1 site are shown.

The shrubs/dunes cover at the site was sampled by means of four 30x30m sampling squares. An example of the results is also shown in Figure 5.17. As evident, dunes are aligned in the NW-SE direction.

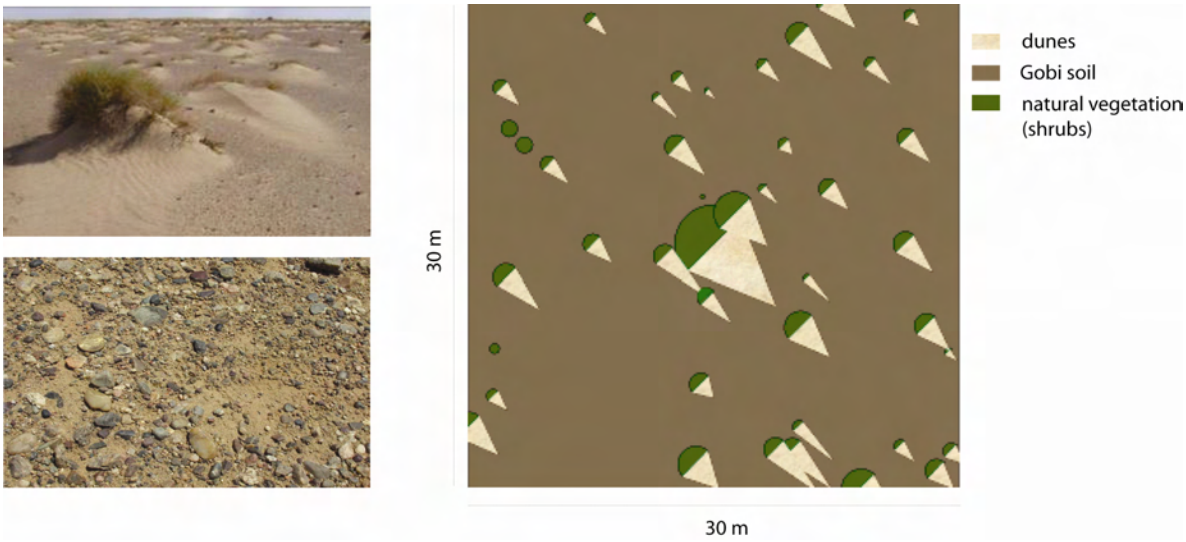

Figure 5.17. (left) Landscape and Gobi, "inter-dune" soil pictures at GB1. (right) example of the shrubs/dunes pattern, sampled at GB1.

With the purpose of assessing to what extent such anisotropy might influence dust emission, the correlation between emission fluxes and wind direction was explored. Results are shown in Figure 5.18. In Figure 5.18(top), friction velocity time series is reported together with wind direction. Figure 5.18(bottom) reports a polar plot of measured particle fluxes vs. wind direction. Colours in Figure 5.18 are used to identify three time periods with different prevailing wind directions. Figure shows that during the emission event of 25 May prevailing winds were from E, and that in the previous days, when no relevant emissions were recorded by the EC system, wind came mostly from N and S. It can be argued that the eastern winds –impacting on the dunes perpendicularly - are able to mobilize the sand of the dunes more efficiently than wind from N or S. This sand feeds the saltation flux and promotes dust emission by sandblasting. If the wind is not efficient in moving sand from the dunes, even strong winds do not cause relevant dust emission. However, the WEAM does not consider wind direction as an influencing parameter. Such lack of parameterization did not allow to sufficiently take into account wind processes on an anisotropic surface; it might explain the major differences with respect to measured fluxes. Interestingly, after the storm event of May 25th the direction of the dunes changed

according to the prevalent wind direction during the storm (E); consequently, susceptibility to the wind direction also changes with time.

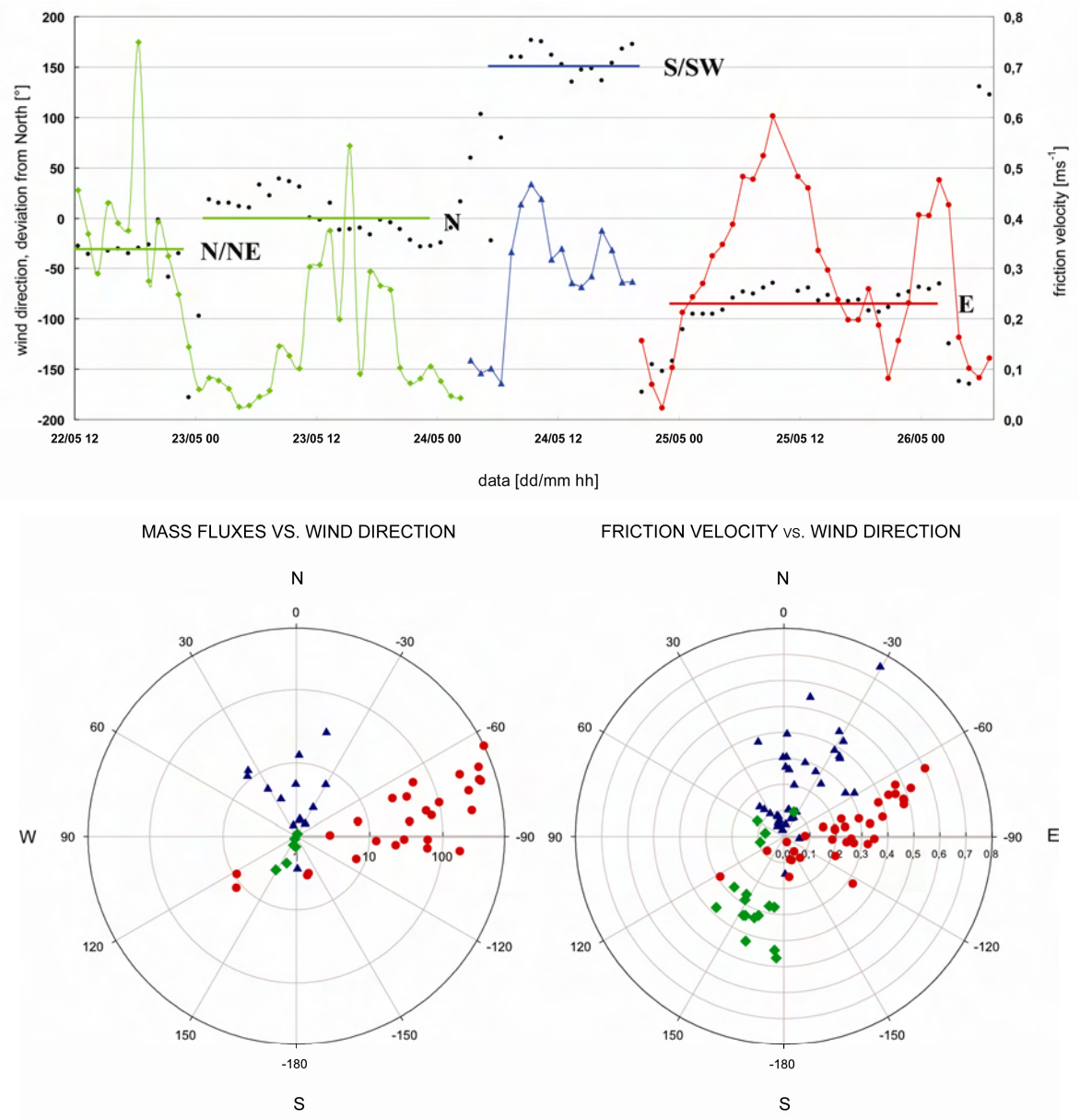

Figure 5.18. (top) Time series of friction velocity (solid line with symbols) and wind direction (black dots) during the monitoring period at GB1. Colors distinguish periods with different prevailing wind directions: green for N and N/NE winds, blue for S/SW winds and red for E/NE winds. (bottom) Polar plots of $M_{0.26\text{-}7.00}$ fluxes (left) and friction velocity (right) as a function of wind provenance direction. Units are [kg km^{-2}h^{-1}] for mass fluxes and [ms^{-1}] for friction velocities. Colours and symbols are as in Fig. 5.16(top).

This suggests that, for such sites, the occurrence of intense erosion (and possibly of dust storms) is related to a *change* in the prevailing wind direction, that creates suitable conditions for efficient sand dislodgment and intense sandblasting. Filtering data according to the wind direction and selecting only those related to eastern winds, a far better

agreement is reached between modelled and measured dust fluxes, as shown in Figure 5.19. The correlation coefficient reached the satisfying value of r^2=0.87. The linear regression also highlights a good agreement also in terms of absolute values, with a gain of 0.89 and an offset of 49 kg $h^{-1}km^{-2}$.

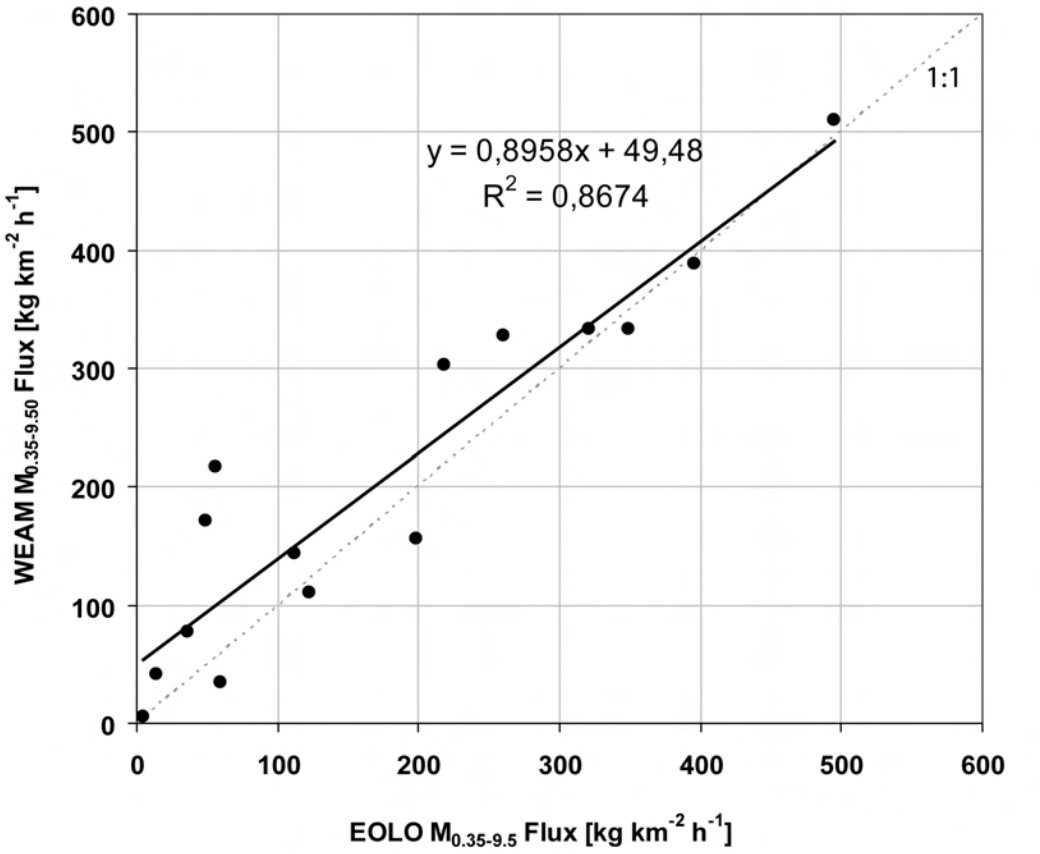

Figure 5.19. WEAM vs. EOLO $M_{0.35\text{-}9.50}$ fluxes (aerodynamic diameters) at the GB1 site after data filtering according to wind direction. Only data for winds coming from the [-60°, -120°] sector were considered. Solid line, best linear fitting, dashed line, 1:1 line.

It is worth noting that the GB1 site is representative of typical landscapes of the western Alashan region, that might be responsible for an important portion of dust emission in that area. Careful characterization of these sources is thus crucial for an improved modelling of DSS arising in China. Prospero et al (2002) discussed how juxtaposition of sand seas and former alluvial areas represents one of the most peculiar environmental characteristic of major dust sources of the world. The area of Ejin'a is surrounded by sand seas of dunes and mega-dunes. The sand found at the GB1, while not typical of the Gobi soil on its own, is likely to be deposited at the site from previous events of sand transport. It is reasonable to assume that this sand is provided by the sand seas that can be found some 50-100 km far from the site.

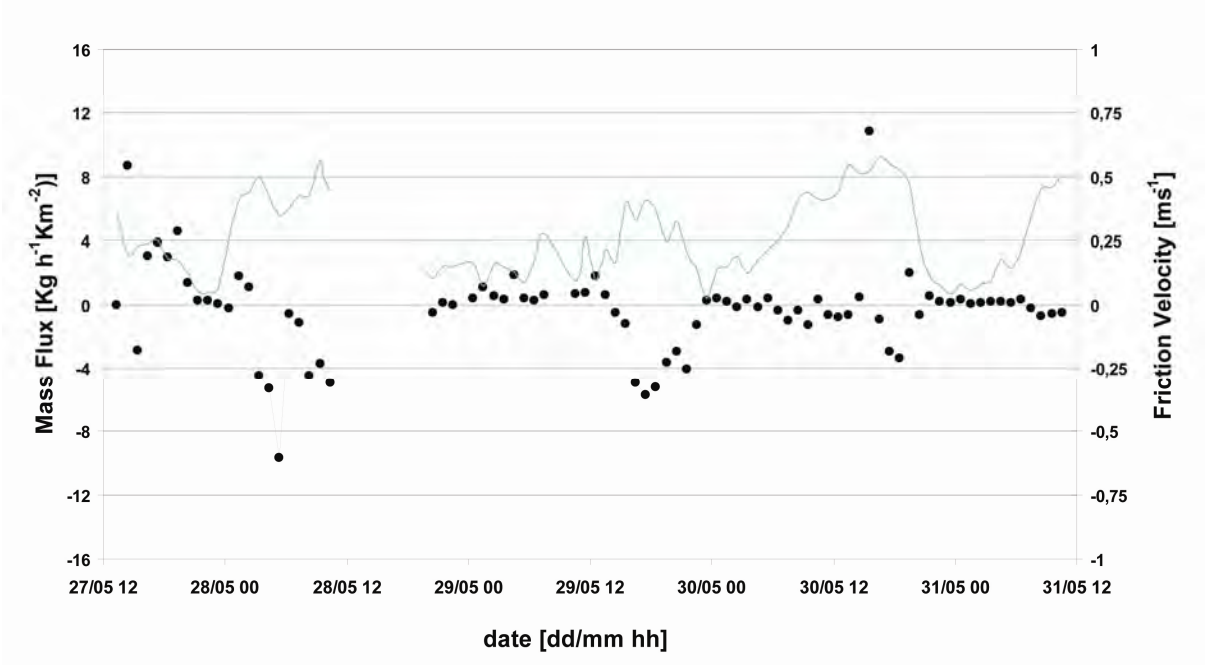

Figure 5.20. $M_{0.26\text{-}7.00}$ **fluxes (black circles) and friction velocity (light blue line) measured by EOLO at GB2 site for5 days from 27 to 31 May 2005**

The deposition of such sand promoted by the sparse vegetation, created the small shrub/dune pattern. This makes the site a source on its own, when following events of strong winds from a suitable direction mobilize the sand of such small dunes.

In total absence of vegetation, the sand deposition (and accumulation) is much lower, and thus the site lacks of the soil component that can feed the sandblasting process. This is the case of the GB2 site, where indeed no relevant emissions where recorded by EOLO, even in case of strong winds and high friction velocities (Figure 5.20). On the contrary, high friction velocities corresponded to net deposition fluxes; this is consistent with the fact the, in absence of sources, high downward momentum fluxes cause efficient particle dry deposition.

5.4.3 Dust fluxes vs. friction velocity

In Sect. 5.2 we have explored the dependence of emission fluxes from friction velocity during the storm event occurred at GB1.

In Figure 5.21 the experimental result obtained with EOLO is compared to several models. Once again, only data from the dust event of May 25th are shown. In the graph, solid lines represent the best fitting power law, the best fitting 3rd-order power law according to the model of Shao et al. (1993), the best fitting 4th-order power law, according to the model of Gillette and Passi (1998), and the WEAM model as applied basing on the field data.

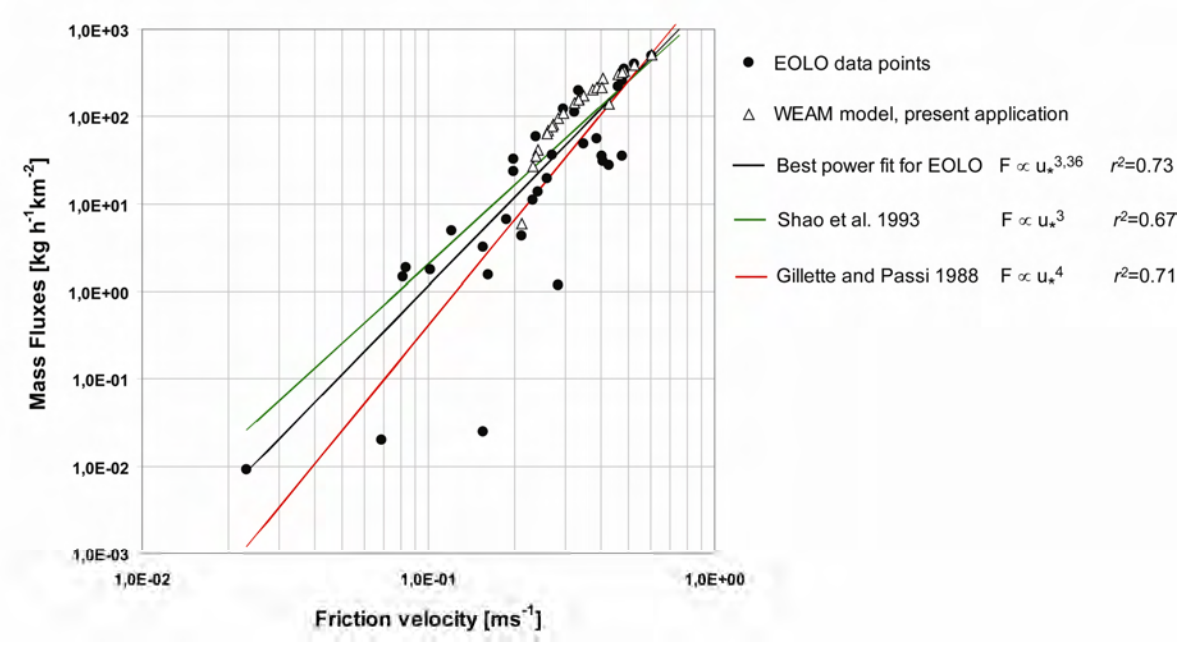

Figure 5.21. Mass fluxes vs. friction velocity during the dust event of 25 May at GB1. EOLO data points (black circles), WEAM model application (triangles). Also shown are the best power fitting for EOLO data points (black line), the best fitting 3rd-power model, according to Shao et al. (2003), and the best fitting 4th-power model, according to Gillette and Passi (1998). In the legend, values of r^2 are also reported.

All of the models fit experimental data fairly well. The best power fitting, featuring an exponent of 3.36, correlates with the experimental data worst than the present WEAM model application (r^2=0.73 and 0.86 respectively), whose higher power is 4. This suggests that, limiting the comparison to the higher power degree, might lead to misinterpretations; indeed, even though the higher power seems to be overestimated in WEAM, the whole model fits experimental data excellently, and better than any "pure" power law.

5.5 Effectiveness of mitigation interventions at different scales

5.5.1 Air-sowing activity within the 3N Shelterbelt Programme

EOLO was used to assess dust emissions - and dust emission reduction - from an area of Alashan desert interested by a long-lasting afforestation intervention by air-sowing (see Sect. 4.4). Unfortunately, it has not been possible to monitor a "reference" site featuring the same soil type while not covered by man-made vegetation. However, it is reasonable to assume that the soil at this site – if bare - is more susceptible to wind erosion than the soil at GB1, because of its textural properties, featuring far more silt and sand percentages. Thus, the GB1 site is taken as a "conservative" reference to evaluate the effectiveness of the air-sowed vegetation cover in reducing dust emission.

To perform the comparison, we derived a regression function of dust emission vs. friction velocity (see Sect. 5.4.3) and used this function to calculate an *annual emission* factor for the two sites. By *emission factor* we mean the summation over a solar year (from January, 1st to December, 31st) of dust emissions. Because annual data of wind, temperature and humidity are only available on a daily scale for the sites of interest, we actually calculated the emission factors as a summation, over the year, of *daily emission values*. For the seek of comparison, we used the same "climatic year" for both sites. Friction velocity was derived from daily wind speed data according to:

$$u_* = kU / \ln(z / z_0) \tag{5.3}$$

where *k* is the Von Kármán constant, U is the wind speed, *z* is the height at which the wind speed has been measured (10m), and z_0 is the roughness length, assumed for the two sites (according to the vegetation survey) as:

GB1: $z_0 = 0.1\ m$

AS: $z_0 = 0.4\ m$

Following a modelling approach, for each day the emission is assumed possible only if the friction velocity is higher than the threshold friction velocity that, as a function of soil moisture, changes on a daily bases. The threshold friction velocity is calculated according to Eq. (4.15), where u_{t0}^* is a function of the soil size distribution, and the enlargement factors H and R are functions of the soil water content and of the surface cover by non erodible elements, respectively. As for the soil water content, this is derived according to Eqs. (4.16-19), where the daily values of relative humidity are derived by the actual temperature and the dew-point temperature. These latter parameters are also available with a daily time step. Nevertheless, it is not reasonable to expect *the daily average friction velocity* to be larger than the threshold friction velocity: indeed, this request is true for the *instantaneous friction velocity*. On the other hand, a certain limit must still hold for the lower friction velocity that is able to generate wind erosion: as a tentative compromise, a "*daily threshold friction velocity*" is defined as:

$$u_{*DT} = \alpha \cdot u_{*T} \quad \alpha = 1/3 \tag{5.4}$$

The condition for having a daily non-zero dust emission is that *the daily friction velocity is greater than the daily threshold friction velocity*; only for these days an emission is actually calculated. The choice of the value of *1/3* for α lies on a poor physical ground. However, a sensibility analysis has been carried out: we verified that, for values of α ranging from α *=2/3* to α *=1/3*, the values of the emission factors changed no more than 10%. Thus, the

choice of the threshold within a reasonable range doesn't affect the order of magnitude of the emission factor to a large extent.

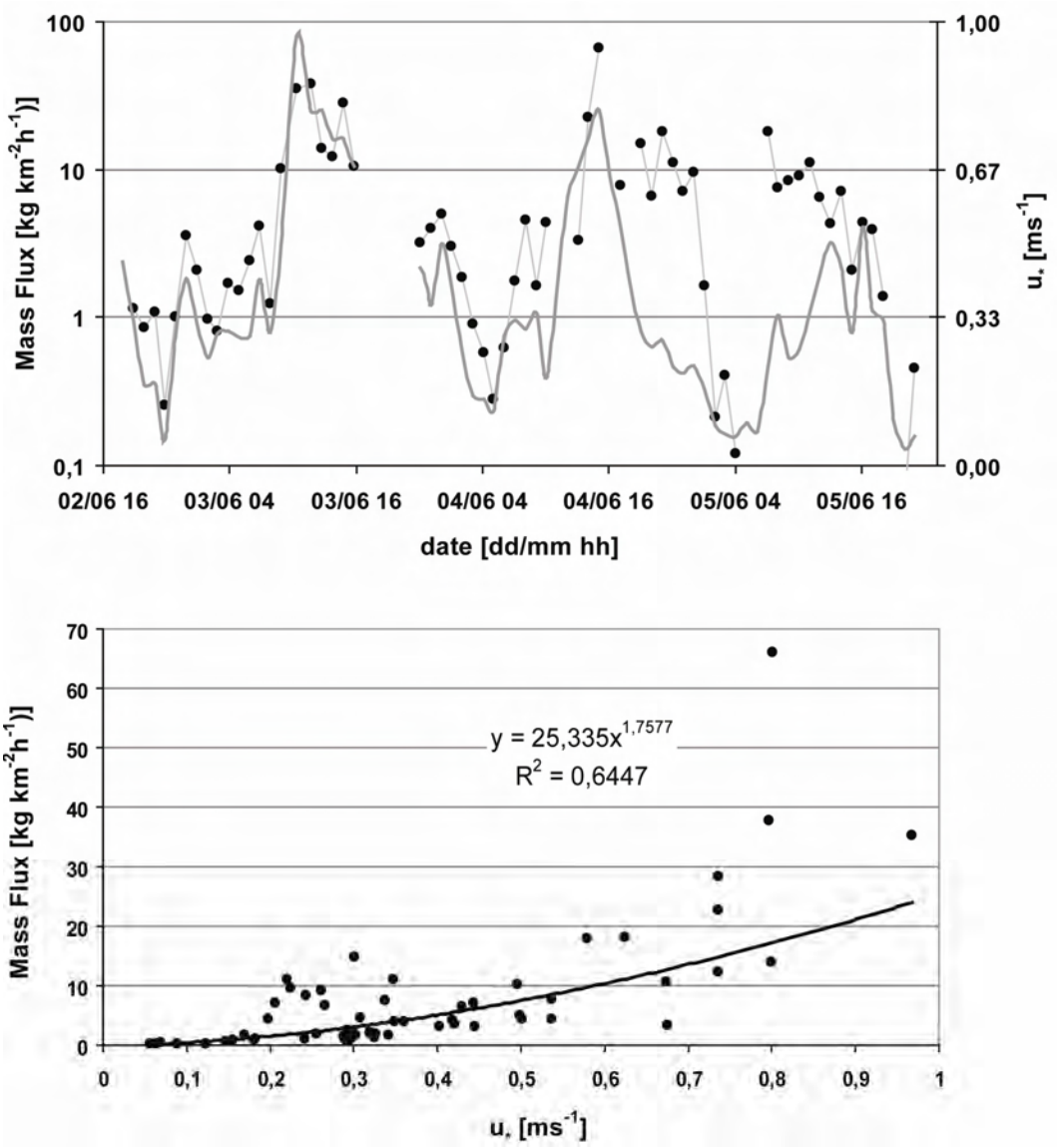

Figure 5.22. a) Time series of $M_{0.26\text{-}700}$ fluxes (black dots) and friction velocity (solid gray line) at the AS site for the monitoring period 2-5 June 2005. Fluxes are represented on a logarithmic scale. b) $M_{0.26\text{-}700}$ fluxes vs. friction velocity (black dots), and power regression (solid line), derived from the same data.

A major limit of this approach must be carefully taken into account. Dust emission by wind erosion is an intermittent phenomena, that is much more related to the instantaneous wind speed, rather than to the average wind speed; it means that a "daily dust emission" value derived by a daily wind data is to be considered as a very rough estimation. As an example, consider the following situations: a day with a constant wind speed of 7 m/s (that has a daily average of 7 m/s, a rather high one), might have zero emissions, if no "spikes" of

wind occur. On the contrary, a daily average of 4 m/s with several spikes up to 12-14 m/s could give high emissions. For these reason, results have to be considered as indicative.

We already derived an emission function for the GB1 site:

$$F_p^{GB1}(u_*) = 4185 u_*^{3,36} \tag{5.5}$$

where F_p is expressed as [kg km^{-2}h^{-1}]. Figure 5.22 shows the time series of mass fluxes (a) and the relation between such fluxes and friction velocity (b) for the AS site, during the monitoring period 2 to 5 June 2005. Note that here the trend of emissions follows the friction velocity pattern strictly. This is consistent with the fact the soil cover is homogeneous at this site and thus wind direction is not expected to play a role in the emission dynamic (Sect. 5.4.2).

The power regression gave the relation:

$$F_p^{AS}(u_*) = 25 u_*^{1,75} \tag{5.6}$$

Using Eqs. (5.3-6) we calculated the following emission factors (using wind and temperature data referred to the year 2004 at the meteorological station of Ejin'a):

$$EF_{GB1} = 608412 \ kg\,km^{-2}yr^{-1}$$
$$EF_{AS} = 6791 \ kg\,km^{-2}yr^{-1} \quad .$$

Even though this estimations are affected by a series of uncertainties (that, in any case, are the same for both sites), the result shows a difference of two order of magnitude in the emissions from the AS site with respect to GB1.

5.5.2 Conservation tillage implementation in the Beijing Municipality

In 2005, there were 173000 hectares of croplands in the Beijing Municipality, with some 53000 hectares of winter wheat, 70000 of spring maize and legume and 50000 of summer maize. Globally, conservation tillage was applied to some 50% of total croplands, as summarized in Table 5.3.

Planting mode	Crop species	Total cultivated area (ha)	Cultivated area by CT (ha)	(CT/Total) Percentage
Two-crops a year	Summer maize	50,000	45,000	90%
	Winter wheat	53,000	6,600	12.5%
One-crop a year	Spring maize and Legume	70,000	31,000	44.8%
Total	----	173,000	88,000	50.7%

Table 5.3. Total croplands in Beijing Municipality and share of conservation tillage in 2005

In view of the 29th Olympic Games that will be held in Beijing in 2008, Beijing Municipality has started a program aiming at improving the urban and rural eco-environments, reducing sand and dust sources and preventing and control sand-dust pollution. Conservation tillage diffusion plays a central role in this action. The goal is to implement conservation tillage for grain crops in nine districts/counties of Beijing, expanding the concerned area from 88000 to 153000 hectares (Nie, 2006), according to a schedule as in Table 5.4.

Types of crops	2006	2007	2008	Total Area
Double-crop	10700	17400	7800	35800
Spring corn	10200	11500	9900	31600
Maize	400	470	470	917
Total	21.400	29.400	18100	68900
Share	31.0%	42.6%	26.4%	100%

Table 5.4. Schedule of conservation tillage expansion in three years (2006-2008) in the Beijing Municipality.

With the aim of assessing the overall effect of this large scale intervention plan, in the framework of WinDust we started a set of comparisons between conservation and traditional tillage implementations.

As a first attempt and following the same approach as in Sect. 5.5.1, we compared the annual emission factors from two agricultural sites in the Beijing Municipality: the first one (CPa, see Sect. 4.4) is a spring maize minimum tillage experimental site; it is treated with low-tillage ploughs and sewers, with both standing and laying crop residues left on the field surface. The second (YQ) is a maize field worked with traditional agricultural techniques, including deep ploughs, crop residues burning, etc. In this case, the soil texture of the two sites is essentially the same (see Table 5.1), hence the difference in site emissivity is only driven by human intervention.

Figure 5.23 shows the emission fluxes as functions of friction velocity for CPa and YQ sites, during the monitoring campaign of Spring 2006. The best fitting power regressions are:

$$F_p^{YQ}(u_*) = 2{,}70u_*^{4{,}07}$$
$$F_p^{CPa}(u_*) = 1{,}60u_*^{3{,}26} \qquad (5.7)$$

Note that largely different exponents of the power laws were obtained for the two agricultural sites, consistently with former results found in literature (see Sect. 3.1.7). Using these emission functions, we calculated the annual emission factors as described in Sect.

5.5.1, using *the same climatic year* for the two sites, as derived from the meteorological station of Changping. We obtained the following emission factors:

$$EF_{YQ} = 1{,}45 \ \ kg\,km^{-2}\,yr^{-1}$$

$$EF_{AS} = 0{,}85 \ kg\,km^{-2}\,yr^{-1}$$

This suggests that the conservation tillage practice has the potential to reduce dust emissions for agricultural sites by some 40% on an annual bases, with respect to traditional techniques.

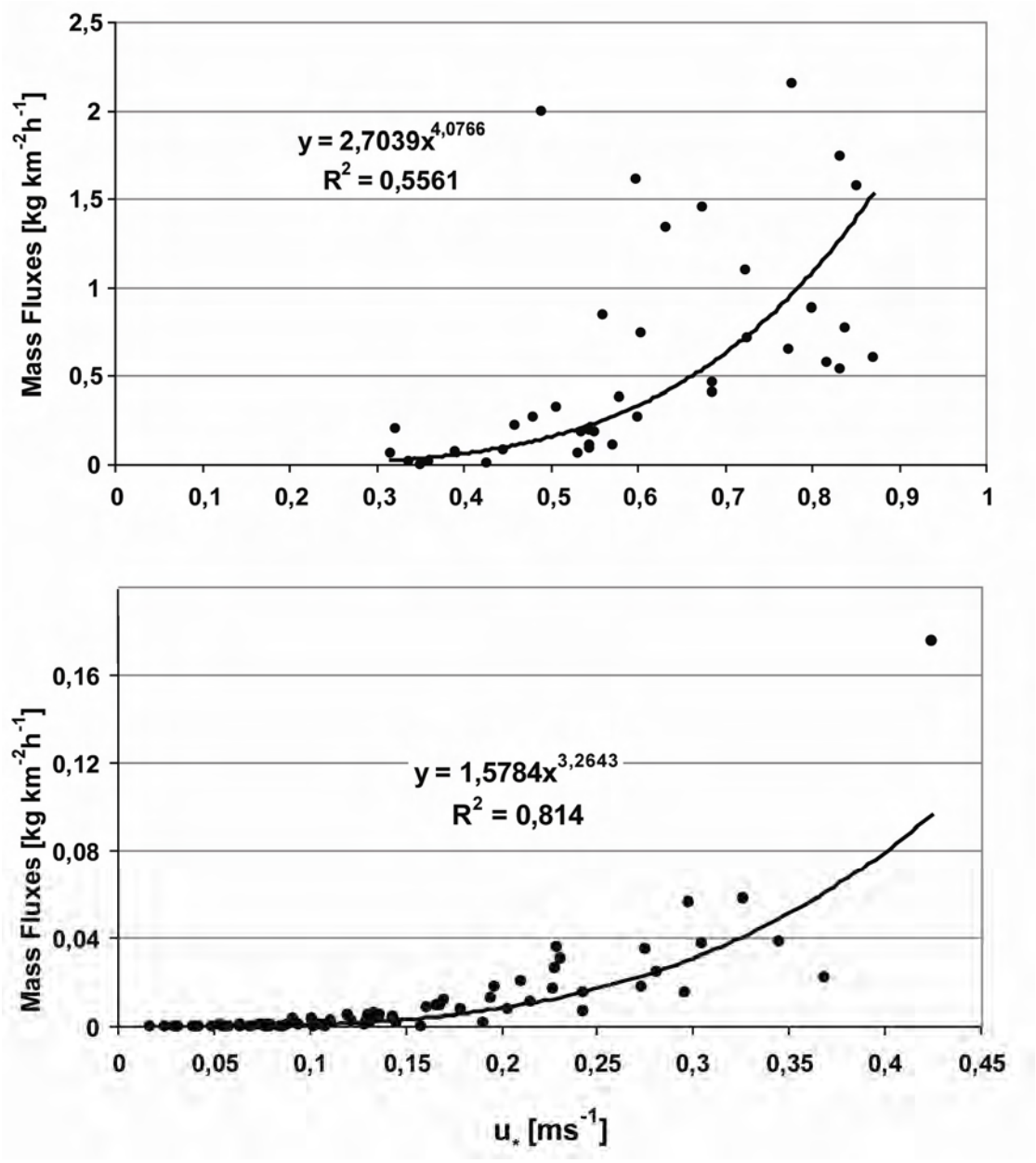

Figure 5.23. Mass fluxes ($M_{0.26\text{-}700}$) vs. friction velocity for the two agricultural fields CPa (top) and YQ (bottom). Black circles: data points; solid lines: best fitting power regressions. CPa is an experimental field of conservation tillage, while YQ is representative of a traditionally worked maize field.

Using *site specific climatic data*, we compared the emission factors derived by EOLO with those calculated using US EPA formulas (Nie, 2006). Results are summarized in Table 5.5. It is interesting to note that, while the EPA prevision matches perfectly out calculations for the traditionally tilled field – suggesting that the formulas are well calibrated for such well-known situation – the emission reduction due to conservation tillage is largely overestimated, with respect to EOLO results. It might suggest that tuning of a dust emission formula for conservation tillage conditions is not as easy as for traditional conditions; emissions might strongly depend on what kind of conservation practice is actually implemented and the modelling should take these difference into due account.

	WORKING TECHNIQUE	ANNUAL EMISSION * [T km-2yr-1]	
		EOLO	EPA**
YANQING	Traditional	**1,45**	**1,45**
CHANGPING	Conservative	**2,4**	**0,82**

* Based on site-specific climatic data

** Courtesy of Mr. Nie Lei (see WinDust Report, 2006)

Table 5.5. Annual estimation of dust emissions from two agricultural sites in Beijing. Comparison between EOLO estimation and simulation with US EPA formulas. This calculations are based on *site specific* data.

6
SUMMARY AND CONCLUSIONS

In this thesis we addressed a new methodology for the assessment of wind erosion with particular reference to the development of a new instrumentation for the direct measurement of mineral dust particle emission fluxes. This work was intended to fill the gap existing in the set of tools needed to study wind erosion at all its relevant scales. Indeed, to the best of our knowledge, no instruments for the fast, direct measurements of vertical fluxes of dust particles exist. The instrumentation is intended as a tool for wind erosion model validation and evaluation.

Wind erosion is here addressed as one of the main mechanisms of desertification; in particular, the role of atmospheric dust in the desertification process is stressed out. An overview of the wind erosion phenomena at global and local scales is provided, in order to introduce fundamental notions that are needed to clearly mean why a dust emission measuring system was needed and to clarify its potentialities in terms of model validation and tuning. The developed system is based on the eddy covariance theory. So far, eddy covariance has been used only for gases or particles with negligible mass; hence, an extension of the theory to heavy particles was needed. It helped defining the range of particle to which eddy covariance could be applied safely, and assessing in which conditions measured fluxes are representative of actual emissions.

The system, called EOLO was designed and optimized to measure vertical fluxes of particulate matter in the optical range 0.26-7.00 μm, that roughly corresponds to the aerodynamic range 0.35-9.50 μm: in terms of mass, this is a good approximation to PM_{10}. The system is composed primarily by a 3D sonic anemometer and an optical particle counter that samples the dust-laden air. It provides size-segregated number fluxes on a 30-

minutes base; surface, volume and mass fluxes are also estimated assuming spherical particles.

EOLO was firstly applied in two monitoring campaigns in Northern China, in the framework of the WinDust project. The campaigns involved Gobi desert sites, afforested sites and agricultural sites in the Beijing Municipality. EOLO was used to investigate the relation between dust emission fluxes and friction velocity. Results showed that this relation is best represented by a power fitting of order 3.36, thereby confirming some former result found in the literature. Monitoring a Gobi desert site featuring a sparse shrubs pattern highlighted that natural vegetation might act as to enhance wind erosion, if certain conditions hold. It further showed that wind direction with respect to soil cover anisotropies might play a major role in the emission process, and stressed out that this dependence should be taken into due account when modelling wind erosion. Comparison with the WEAM model showed that, as far as the wind direction is taken into due account, an excellent agreement in the emission fluxes is reached.

EOLO was also used to evaluate the potentialities of emission reduction of afforestation programs. Monitoring an air-sowed afforestation intervention over a sandy land in the Eastern Alashan desert showed that it has the potential of abating dust emission by as much as 2 order of magnitude. Similarly, the comparison between results obtained in two agricultural sites (maize fields) in the Beijing Municipality, showed that conservation tillage can reduce dust emission by some 40% with respect to traditional techniques. Of course, any conclusion here is intended as a preliminary result, suggested by obtained data. Far more monitoring efforts are indeed needed to carefully assess the effects of all the processes and driving parameters involved in wind erosion.

Although limited by the number of events recorded, results obtained provide useful information to parameterize the emission process during both dust storms and intense emission events. A co-spectral analyses showed that the instrument was able to provide reliable data when high particle concentrations were reached and under strong turbulence conditions. Its accuracy was definitely much lower when low concentrations and limited turbulence occurred over the site, also because of the uncertainties in particle counting. However, this limitation can be partly circumvented if the dilution step is avoided and the whole air sample sent to the optical sensor. We believe that an increase of a factor of 20 in the particle number is more than enough to get statically accurate values of particle concentrations under normal conditions, as it has been shown by previous authors. Other limits of the instrument are associated with the particle sizing capabilities of the OPC and

with biases arising from sub-kinetic sampling occurring in the coarser mode under very high turbulent conditions. This aspects are presently under investigation.

EOLO has potentialities that go beyond the study of wind erosion; indeed, it is able to measure particulate vertical fluxes regardless of their actual origin. As far as we are able to measure some properties of the particles under investigation (such as their refractive index, density and shape), it can measure fluxes of any kind of particles in its range. As an example, it could be used to measure particulate emission fluxes due to fires, or fluxes (either emissions or depositions) of anthropogenic pollutants in urban environments, such as those due to traffic, factories, domestic pollutants, and to better assess their actual sources.

REFERENCES

Albrecht, B.: Aerosols, Cloud Microphysics, and Fractional Cloudiness, Science, 245, 1227–1230, 1989.

Andreae, M. O.: Climate effects of changing atmospheric aerosol levels, in World Survey of Climatology, Future Climate of the World, 16, A. Henderson Sellers ed., Elsevier Publ., Amsterdam, 341–392, 1995.

Andreae, M. O. and Crutzen, P. J.: Atmospheric aerosols: Biogeochemical sources and role in atmospheric chemistry, Science, 276, 1052−1056, 1997.

Aubinet, M.: Estimates of the annual net carbon and water exchange of forests: the EUROFLUX methodology, Adv. Ecol. Res., 30, 113-175, 2000.

Aubinet, M., Chermanne, B., Vandenhaute, M., Longdoz, B., Yernaux, M. and Laitat, E.: Long term measurements of water vapour and carbon dioxide fluxes above a mixed forest in Ardenne's region, Agricult. For. Met., 108, 293–315, 2001.

Bagnold, R. A.: The Physics of Blown Sand and Desert Dunes, Methuen & Co. ed., London, 1941.

Baldocchi, D., Hicks, B. B. and Meyers, T. D.: Measuring biosphere-atmosphere exchanges of biologically related gases with micrometeorological methods, Ecology, 69, 1331–1340, 1988.

Bates, T. S., Anderson, T. L., Baynard, T., Bond, T., Boucher, O., Carmichael, G., Clarke, A., Erlick, C., Guo, H., Horowitz , L., Howell, S., Kulkarni, S., Maring, H., Mccomiskey, A., Middlebrook, A., Noone, K., O'dowd, C. D., Ogren, J., Penner, J., Quinn, P. K., Ravishankara, A. R., Savoie, D. L., Schwartz, S. E., Shinozuka, Y., Tang, Y., Weber, R. J. and Wu, Y.: Aerosol direct radiative effects over the northwest Atlantic, northwest Pacific and North Indian Oceans: estimates based on in-situ chemical and optical measurements and chemical transport modeling, Atmos. Chem. Phys., 6, 1657–1732, 2006.

Bilbro, J. D. and Fryear, D. W.: Wind Erosion losses as related to plant silhouette and soil cover, Agron J, 86(3), 550-553, 1995.

Blanchard, D. C.: The production, distribution and bacterial enrichment of the sea-salt aerosol, in Air-Sea Exchange of Gases and Particles, P. S. Liss and W. G. N. Slinn eds., Reidel Publ., Boston, 407−454, 1983.

Boahene, K.: The Challenge of Deforestation in Tropical Africa: Reflections on its Principal Causes, Consequences and Solutions, Land Degrad. Develop., 9, 247–258, 1998.

Bonasoni, P., Cristofanelli, P., Calzolari, F., Bonafè, U., Evangelisti, F., Stohl, A., Zauli Sajani, S., Van Dingenen, R., Colombo, T. and Balkanski, Y.: Aerosol-Ozone correlations during dust transport episodes, Atmos. Chem. Phys., 4, 1201–1215, 2004.

Buzorius, G., Rannik, Ü., Nilsson, E. D., Vesala, T. and Kulmala, M.: Analysis of measurement techniques to determine dry deposition velocities of aerosol particles with diameters less than 100 nm, J. Aerosol Sci., 34, 747-764, 2003.

Chatenet, B., Marticorena, B., Gomes, L. and Bergametti, G.: Assessing the microped size distributions of desert soils erodible by wind, Sedimentology, 43, 901–910, 1996.

Chen, W., Zibhao, L., Zhenshan, L. and Zuotao, Y.: Wind Tunnel test of the influence of soil moisture on erodibility of loessial sandy loam soil by wind, J. Arid Environ., 34, 391-402 1996.

Chepil, W. S.: Properties of soil which influence wind erosion, IV. State of dry aggregate structure, Soil Sci., 75(2), 387-401, 1951.

Chepil, W. S.: Influence of moisture on erodibility of soil by wind, Soil Sci. Soc. Am. Proc., 0, 288-292, 1956.

Clarke, A. D., Shinozuka, Y., Kapustin, V. N., Howell, S., Huebert, B., Doherty, S., Anderson, T., Covert, D., Anderson, J., Hua, Z., Moore, K. G., Mcnaughton, C. and Carmichael, G.: Size-Distributions and Mixtures of Dust and Black Carbon Aerosol in Asian Outflow: Physio-chemistry and Optical Properties, ACE-Asia project report, 2004.

Crawley, D. M. and Nickling, W. G.: Drag Partition For Regularly Arrayed Rough Surfaces, Bound-Lay. Meteorol., 107, 445–468, 2003.

Csanady, G. T.: Turbulent Diffusion of Heavy Particles in the Atmosphere, J. Atmos. Sc., 20, 201–208, 1963.

Dentener, F. J., Carmichael, G. R., Zhang, Y., Lelieveld, J. and Crutzen, P. J.: Role of Mineral Aerosol as a Reactive Surface in the Global Troposphere, J. Geophys. Res., 101, 22869–22889, 1996.

Dong, Z., Wang, H., Liu, X. and Wang, X.: The blown sand flux over a sandy surface: a wind tunnel investigation on the fetch effect, Geomorphology, 57, 117–127, 2004.

Dong, Z., Wang, X. and Liu, L.: Wind erosion in semiarid China: an overview, J. Water Soil Cons., 55, 439–444, 2000.

Dorsey, J. R., Nemitz, E., Gallagher, M. W., Fowler, D., Williams, P. I., Bower, K. N. and Beswick, K. M.: Direct measurements and parameterisation of aerosol flux, concentration and emission velocity above a city, Atmos. Environ., 36, 791-800, 2002.

Dregne, H. E.: Desertification: Symptoms of a crisis, in Desertification, process, problems, perspectives, University of Arizona Press Publ., 1976.

Dregne, H. E.: Desertification control: a framework for action, Environ. Monit. Assess., 37, 111-122, 1995.

Duce, R. A.: Sources, distributions, and fluxes of mineral aerosols and their relationship to climate, in Dahlem Workshop on Aerosol Forcing of Climate, R. J. Charlson and J. Heintzenberg eds., John Wiley Publ., New York, 43–72, 1995.

Dunjo Denti, G.: Developing a Desertification Indicator System for a small mediterranean catchment: a case study from the Serra de Rodes, Alt Empordà, Cataluna, NE Spain, Ph.D. Thesis, University of Girona, Girona, 2004.

Durst, F., Milojevic, D. and Schonung, B.: Eulerian and Lagrangian prediction of particulate two-phase flows: a numerical study, Applied Mathematics Modelling, 8, 101-115, 1984.

El Beltagy, A.: Land degradation: a global and regional problem, http://www.unu.edu/millennium/el-beltagy.pdf, 2000.

Fao: Provisional methodology for assessment and mapping of desertification. Food and Agriculture Organization of the United Nations and United Nations Environment Programme, Rome, Italy, 1984.

Fècan, F., Marticorena, B. and Bergametti, G.: Parametrization of the increase of the aeolian erosion threshold wind friction velocity due to soil moisture for arid and semi arid areas, Ann. Geophysicae, 17, 149-157, 1999.

Feichter, J., Roeckner, E., Lohmann, U. and Liepert, B.: Nonlinear aspects of the climate response to greenhouse gas and aerosol forcing, J. Climate, 2384–2398, 2004.

Finlayson Pitts, B. J. and Pitts, J. N.: Chemistry of the upper and lower atmosphere. Theory, experiments and applications, Academic Press Publ., San Diego (CA, USA), 2000.

Fryrear, D. W.: A field dust sampler, J. Water Soil Cons., 41, 117-119, 1986.

Gardner, W. R.: Field measurement of soil water diffusivity, Soil Sci. Soc. Am. Proc., 34, 832-833, 1970.

Garrat, J. R.: Cold fronts and dust storms during the Australian summer 1982-1983, Wheater, 39, 98-103, 1984.

Garrat, J. R., Howells, P. A. C. and Kowalczyk, E.: The behaviour of dry cold fronts travelling along a coastline, Monthly Weather Reviews, 117(1208-1220), 1989.

Gash, J. H. and Culf, A. D.: Applying linear de-trend to eddy correlation data in real time, Bound-Lay. Meteorol., 79, 301-306, 1996.

Gillette, D. A.: A qualitative geophysical explanation for "hot spot" dust emitting source regions, Contrib. Atmos. Phys., 72, 67–77, 1999.

Gillette, D. A. and Passi, R.: Modelling dust emission caused by wind erosion, J. Geophys. Res., 93, 14233-14242, 1988.

Gillette, D. A. and Stockton, P. H.: The effect of non erodible particles on wind erosion at erodible surfaces, J. Geophys. Res., 94, 12885-12893, 1989.

Gillette, D. A. and Walker, T. R.: Characteristics of airborne particles produced by wind erosion of sandy soils, high plains of west Texas, Soil Sci., 123, 97-110, 1977.

Gomes, L., Bergametti, G., Dulac, F. and Ezat, U.: Assessing the actual size distribution of atmospheric aerosols collected with a cascade impactor, J. Aerosol Sci., 21, 47–59, 1990.

Goudie, A. S.: Dust storms in space and time, Prog. Phys. Geogr., 7, 502–530, 1983.

Goudie, A. S. and Middleton, N. J.: The changing frequency of dust storms through time, Climate Change, 20, 197–225, 1992.

Goulden, M. L., Munger, J. W., Fan, S. M., Daube, B. C. and Wofsy, S. C.: Measurements of carbon sequestration by long-term eddy covariance: methods a critical evaluation of accuracy, Glob. Change Biol., 2, 159-168, 1996.

Graßl, H.: Possible changes of planetary albedo due to aerosol particles, in Man's Impact on Climate, K. Bach, Pankrath ed., Elsevier Publ., Amsterdam, 1979.

Greeley, R. and Iversen, J. D.: Wind as a geological process on Earth, Mars, Venus and Titan, Cambridge Univ. Press Publ., New York, 1985.

Gregory, J. M. and Darwish, M. M.: Threshold friction velocity prediction considering water content, Proc. Am. Soc. Agric. Eng., New Orleans, Paper No. 90-2562, 1990.

Gregory, J. M. and Darwish, M. M.: Test results of TEAM (Texas Tech Erosion Analysis Model), International symposium on Soil Erosion Research for the 21th Century, St. Joseph (MI, USA), 2001.

Hagen, L. J.: Process of soil erosion by wind, Ann. Arid Zones, 40(3), 233-250, 2001.

Hansen, J., Sato, M. and Ruedy, R.: Radiative forcing and climate response, J. Geophys. Res., 102, 6831–6864, 1997.

Heintzenberger, J., Raes, F., Schwatrz, S. E. and Coauthors: Topospheric Aerosols, in Atmospheric Chemistry in a Changing World: An Integration and synthesis of a decade of tropospheric research, G. P. Brasseur, R. G. Prinn and A. A. P. Pszenny eds., Springer -Verlag Publ., Heidelberg, 125-156, 2003.

Hering, S., Elderling, A. and Seinfeld, J. H.: Bimodal character of accumulation mode aerosol mass distribution in Southern California, Atmos. Environ., 31, 1-11, 1997.

Holland, J. M.: The environmental consequences of adopting conservation tillage in Europe: reviewing the evidence, Agriculture, Ecosystems & Environment, 103, 1-25, 2004.

Houser, C. A. and Nickling, W. G.: The emission and vertical flux of particulate matter <10 μm from a disturbed clay-crusted surface, Sedimentology, 48, 255-267, 2001.

Hunt, J. C. R. and Weber, A. H.: A Lagrangian Statistical Analysis of Diffusion from a Ground Level Source in a Turbulent Boundary Layer, Quart. J. Roy. Meteor. Soc., 105, 423-443, 1979.

Husar, R. B., Prospero, J. M. and Stowe, L. L.: Characterization of tropospheric aerosols over the oceans with the NOAA advanced very high resolution radiometer optical thickness operational product, J. Geophys. Res., 102, 16889-16909, 1997.

Iso/Ts: 17892-3:2004 - Geotechnical investigation and testing, Laboratory testing of soil, Part 3: Determination of particle density - Pycnometer method, International Organization for Standardization, 7 pages, 2004.

Iversen, J. D., Greeley, R., Marshall, J. R. and Pollack, P. B.: Aeolian saltation threshold: the effect of density ratio, Sedimentology, 34, 699-706, 1987.

Iversen, J. D., Pollack, J. B., Greeley, R. and White, B. R.: Saltation treshold on Mars: the effect of interparticle force, surface roughness, and low atmospheric density, Icarus, 29, 318-383, 1976.

Iversen, J. D. and White, B. R.: Saltation threshold on Earth, Mars and Venus, Sedimentology, 29, 111-119, 1982.

Johansson, S. A. E. and Campbell, J. L.: PIXE: A novel technique for elemental analysis, John Wiley Publ., New York, 1988.

John, W., Wall, S. M., Ondo, J. L. and Winklmayr, W.: Modes in the sze distributions of atmospheric inorganic aerosols, Atmos. Environ., 24A, 2349-2359, 1990.

Kaimal, J. C. and Finnigan, J. J.: Atmospheric Boundary Layer Flows: Their Structure and Measurement, Oxford University Publ., Oxford, 1994.

Kim, D. S., Cho, G. H. and White, B. R.: A wind-tunnel study of atmospheric boundary-layer flow over vegetated surfaces to suppress PM10 emission on Owens (dry) lake, Bound-Lay. Meteorol., 97, 309–329, 2000.

Kolmogorov, A. N.: Local structure of turbulence in an incompressible fluid at large Reynolds numbers, Dokl. Akad. Nauk. SSSR, 1941.

Kristjansson, J. E.: Studies of the aerosol indirect effect from sulfate and black carbon aerosols J. Geophys. Res., 107, 2002.

Kundu, P. K.: Fluid Mechanics, Academic Press Inc. Publ., San Diego, 1990.

Lal, R.: Soil erosion and land degradation: the global risks, Adv. Soil. Sci., 11, 130-172, 1990.

Lal, R.: Potential of desertification control to sequester carbon and mitigate the greenhouse effect, Climate Change, 51, 35-72, 2001.

Lancaster, N.: Geomorphology of Desert Dunes, Routledge Publ., New York, 1995.

Levin, Z. and Yankofsky, S. A.: Contact versus immersion freezing of freely suspended droplets by bacterial ice nuclei, J. Climate App. Meteorol., 22, 1964–1966, 1983.

Leys, J. F. and Raupach, M. R.: Soil flux measurements using a portable wind erosion tunnel, Austr. J. of Soil Res., 29, 533-552, 1991.

Li, Z. P., Cheng, L. L., Xiong, L. X., Li, Z. P., Chenge, L. L. and Lin, X. X.: Studies on the Characteristics of Organic Matter in Degraded Red Soil and the Effect of Application of Organic Manure on It, Soils, 26, 70–76, 1994.

Liu, T. S.: Loess and the environment, China Ocean Press Publ., Beijing, 1985.

Lo Cascio, B., Casa, R. and Rossini, F.: Soil properties after 9 years of different tillage systems on continuous wheat in Central Italy, XIV I.S.T.R.O. Conference, “Agroecological and ecological aspects of soil tillage”. Fragmenta Agronomica 2A, 139-142, 1997.

Lo Cascio, B. and Cereti, C. F.: Interventi agronomici, sistemi di coltivazione e ambiente, Rivista di Agronomia, 3, 289-299, 1995.

Lohmann, U. and Feichter, J.: Global indirect aerosol effects: a review, Atmos. Chem. Phys. Disc., 4, 7561–7614, 2004.

Lohmann, U., Feichter, J., Penner, J. E. and Leaitch, W. R.: Indirect effect of sulfate and carbonaceous aerosols: A mechanistic treatment, J. Geophys. Res., 105, 12193–12206, 2000.

Lu, H.: An integrated wind erosion modelling system with emphasis on dust emission and transport, Ph.D. Thesis, The University of New South Wales, Sydney, Australia, 2000.

Lu, H. and Shao, Y.: A new model for dust emission by saltation bombardment, J. Geophys. Res., 104(16827-16842), 1999.

Macdonald, P. and Green, P.: User's guide to program MIX: an interactive program for fitting mixture of distributions, Ontario, Canada, I. D. Systems, 1988.

Mainguet, M. and Da Silva, G. G.: Desertification and drylands development: What can be done?, Land Degrad. Develop., 9, 375-382, 1998.

Martensson, E. M., Nilsson, E. D., Buzorius, G. and Johansson, C.: Eddy covariance measurements and parameterisation of traffic related particle emissions in an urban environment, Atmos. Chem. Phys., 6, 769–785, 2006.

Marticorena, B. and Bergametti, G.: Modelling the atmospheric dust cycle: 1. Design of a soil derived dust emission scheme, J. Geophys. Res., 100, 415-430, 1995.

Marticorena, B., Bergametti, G., Aumont, B., Callot, Y., N'doum´E, C. and Legrand, M.: Modeling the atmospheric dust cycle: 2. Simulation of Saharan dust sources, J. Geophys. Res., 102, 4387–4404, 1997.

Mcmeeking, G.: Size Distribution Measurements Of Wildfire Smoke-Influenced Aerosol At Yosemite National Park, MS Thesis, Colorado State University, 2004.

Middleton, N. J.: Climatic controls on the frequency, magnitude and distribution of dust storms: Examples from India/Pakistan, Mauritania and Mongolia, in Paleoclimatology and Paleometeorology: Modern and Past Patterns of Global Atmospheric Transport, M. Leinen and M. Sarnthein eds., Kluwer Acad. Publ., Norwell (MA,USA), 97-132, 1989.

Middleton, N. J., Goudie, A. S. and Wells, G. L.: The frequency and source areas of dust storms, in Aeolian Geomorphology, W. G. Nickling ed., Allen and Unwin Publ., New York, 237–259, 1986.

Middleton, N. J. and Thomas, D.: World Atlas of Desertification, Arnold Hodder Headline Group Publ., London, UK, 1997.

Mortimore, M.: Roots in the African Dust: Sustaining the Sub-Saharan Drylands, Cambridge Univ. Press Publ., New York, 1998.

Nemitz, E., Fowler, D., Dorsey, J. R., Theobald, M. R., Mcdonald, A. D., Bower, K. N., Beswick, K. M., Williams, P. I. and Gallagher, M. W.: Direct measurements of size-segregated particle fluxes above a city, J. Aerosol Sci., 31, 116-117, 2000.

Nicholson, S. E., Some, B. and Kone, B.: A note on recent rainfall conditions in West Africa, including the rainy season of the 1997 ENSO year, J. Climate, 13, 2628–2640, 2000.

Nicholson, S. E., Tucker, C. J. and Ba, M. B.: Desertification, drought and surface vegetation: An example from the West African Sahel, Bull. Am. Meteorol. Soc., 79, 815-829, 1998.

Nickling, W. G. and Gillies, J. A.: The stabilizing role of bonding agents on the entrainment of sediment by wind, Sedimentology, 31, 111-117, 1984.

Nickling, W. G. and Gillies, J. A.: Emission of fine-grained particulates from desert soils, in Paleoclimatology and Paleometeorology: Modern and Past Patterns of Global Atmospheric Transport M. Leinen and M. Sarnthein eds., 1989.

Nickling, W. G. and Gillies, J. A.: Dust emission and trasport in Mali, West Africa, Sedimentology, 40, 859-868, 1993.

Nie, L.: WinDust - Sino-Italian Cooperation Project, Internal Report for Phase I, Beijing Environmental Protection Foundation, Beijing, 2006.

Okin, G. S. and Gillette, D. A.: Modelling Wind Erosion and Dust Emission on Vegetated Surfaces, in Spatial Modelling of the Terrestrial Environment, ISBN: 0-470-84348-9, R. Kelly, N. Drake and S. Barr eds., John Wiley & Sons Ltd Publ., 2004

Ono, D., Weaver, S. and Richmond, K.: Quantifying Particulate Matter Emissions from Wind Blown Dust Using Real-time Sand Flux Measurements, Owens Emissions papers, paper-C, EPA, 2003.

Owen, P. R.: Saltation of uniform grains in air, J. Fluid Mech., 20, 225-242, 1964.

Peng, Y., Lohmann, U., Leaitch, R., Banic, C. and Couture, M.: The cloud albedo-cloud droplet effective radius relationship for clean and polluted clouds from RACE and FIRE.ACE, J. Geophys. Res., 107(doi:10.029/2000JD000281), 2002.

Penner, J. E., Andreae, M., Annegarn, H., Barrie, L., Feichter, J., Hegg, D., Jayaraman, A., Leaitch, R., Murphy, D., Nganga, J. and Pitari, G.: Aerosols, their Direct and Indirect Effects, in Climate Change 2001: the Scientific basis, Contribution of WorkingGroup 1 to the Third Assessment Report of Intergovernmental Panel on Climate Change, J. T. Houghton, Y. Ding, D. J. Griggs, M. Noguer, P. J. van der Linden, X. Dai, K. Maskell and C. A. Johnson eds., Cambridge Univ. press. Publ., Cambridge, UK and New York, NY USA, 881, 2001.

Pluhar, J. J., Knight, R. W. and Heitschmidt, R. K.: Infiltration rate and sediment production as influenced by grazing systems in the Texas rolling plains, J Range Manage, 40, 240–243, 1987.

Poesen, J. and Nearing, M.: Soil surface sealing and crusting, C. supplement eds., 24, Catena Verlag Publ., Germany, 1993.

Prospero, J. M.: The atmospheric transport of particles to the ocean, in Particle Flux in the Ocean, SCOPE Rep. 57, V. Ittekkott, S. Honjo and P. J. Depetris eds., John Wiley Publ., New York, 19-52, 1996a.

Prospero, J. M.: Saharan dust transport over the North Atlantic Ocean and Mediterranean: An overview, in The Impact of Desert Dust Across the Mediterranean, S. Guerzoni and R. Chester eds., Kluwer Acad. Publ., Norwell, 133–151, 1996b.

Prospero, J. M., Ginoux, P., Torres, O., Nicholson, S. E. and Gill, T. E.: Environmental characterization of global sources of atmospheric soil dust identified with the Nimbus 7 Total Ozone Mapping Spectrometer (TOMS) absorbing aerosol product, Rev. Geophys., 40(1), 1002, doi:10.1029/2000RG000095, 2002, 2002.

Prospero, J. M., Glacuum, R. A. and Nees, R. T.: Atmospheric transport of soil dust from Africa to South America, Nature, 289, 570-572, 1981.

Prospero, J. M. and Nees, R. T.: Dust concentration in the atmosphere of the equatorial North Atlantic: possible relationship to the Sahelian drought, Science, 196, 1196-1198, 1977.

Pye, K.: Aeolian Dust and Dust Deposits, Academic Press Publ., San Diego (CA, USA), 1987.

Pye, K.: Processes of fine particle formation, dust source regions and climatic changes, in Paleoclimatology and Paleometeorology: Modern and Past Patterns of Global Atmospheric Transport, M. Leinen and M. Sarnthein eds., Kluwer Acad. Publ., Norwell (MA, USA), 3-30, 1989.

Qian, W., Quan, L. and Shi, S.: Variations of the dust storm in China and its climatic control, J. Climate, 15, 1216-1229, 2002.

Quisefit, J., De Chateaubourg, P., Garivait, S. and Steiner, E.: Quantitative analyses of aerosol filters by wavelenght dispersive X-rayspectrometry from bulf reference samplers, X-Ray Spectrom., 23, 59-64, 1994.

Ramaswamy, V., Boucher, O., Haigh, J., Hauglustaine, D., Haywood, J., Myhre, G., Nakajima, T., Shi, G. Y. and Solomon, S.: Radiative Forcing of Climate Change, in Climate Change 2001: The Scientific Basis, Contribution of working group I to the

Third Assessment Report of the Intergovernmental Panel on Climate Change, 15, J. T. Houghton, Y. Ding, D. J. Griggs, M. Noguer, P. J. van der Linden, X. Dai, K. Maskell and C. A. Johnson eds., Cambridge Univ. Press Publ., New York, 349–416, 2001.

Raupach, M. R., Gillette, D. and Leys, J.: The effect of roughness elements on wind erosion threshold, J. Geophys. Res., 98, 3023-3029, 1993.

Ravi, S.: The effect of air humidity on soil susceptibility to wind erosion, Master Thesis, Agricultural University, Kerala, India, 2001.

Reheis, M. C. and Kihl, R.: Dust deposition in southern Nevada and California, 1984–1989: Relations to climate, source area, and source lithology, J. Geophys. Res., 100, 8893–8918, 1995.

Rice, M. A. and Mcewan, I. K.: Crust strength: A wind tunnel study of the effect of impact by saltating particles on cohesive surfaces, Earth Sur. Proc. Land., 26, 721-733, 2001.

Rice, M. A., Willetts, B. B. and Mcewan, I. K.: Observations of collisions of saltating grains with a granular bed from high-speed cine-film, Sedimentology, 43, 21-31, 1996.

Rosenfeld, D.: Suppression of rain and snow by urban and industrial air pollution, Science, 287, 1793–1796, 2000.

Rosenfeld, D., Rudich, Y. and Lahav, R.: Desert dust suppressing precipitation: possible desertification feedback loop, Proc. Natl. Acad. Sci. USA, 98, ,5975–5980, 2001.

Safriel, U., Adeel, Z. and Niemeijer: Dryland Systems, in Millennium Ecosystem Assessment, 623-662, 2000.

Saxton, K. E., Chandler, D., Stetler, L., Lamb, B., Claiborn, C. and Lee, B. H.: Wind erosion and figutive dust fluxes on agricultural lands in the Pacific Northwest, Transactions of the American Society of Agricultural Engineering, 43(3), 623-630, 2000.

Saxton, K. E., Rawls, W. J., Romberger, J. S. and Papendick, R. I.: Estimating generalized soil-water characteristics from texture, Soil Sci. Soc. Am. J., 50(4), 1031-1036, 1986.

Scholes, M. and Andreae, M. O.: Biogenic and pyrogenic emissions from Africa and their impact on the global atmosphere, Ambio, 29, 23-29, 2000.

Scott, W. D.: Measuring the erosivity of wind, Catena, 24, 163-175, 1995.

Shao, Y.: Physics and Modelling of Wind Erosion, Kluwer Academic Publ., 2000.

Shao, Y.: A model of mineral dust emission, J. Geophys. Res., 106(20239–20254), 2001.

Shao, Y., Jung, E. and Leslie, L. M.: Numerical prediction of northeast Asian dust storms using an integrated wind erosion modeling system, J. Geophys. Res., 107, 4814-4820, 2002.

Shao, Y. and Lu, H.: A simple expression for wind erosion threshold friction velocity, J. Geophys. Res., 2000.

Shao, Y. and Lu, H.: Toward quantitative prediction of dust storms: an integrated wind erosion modelling system and its applications, Environmental Modelling & Software, 16, 233-249, 2001.

Shao, Y., Raupach, M. and Leys, J.: A model for predicting Aeolian sand drift and dust entrainment on scales from paddock to region, Austr. J. of Soil Res., 34, 309-342, 1996.

Shao, Y. and Raupach, M. R.: The overshoot and equilibration of saltation, J. Geophys. Res., 97, 20559-20564, 1992.

Shao, Y., Raupach, M. R. and Findlater, P. A.: Effect of saltation bombardment on the entrainment of dust by wind, J. Geophys. Res., 98, 12719-12726, 1993.

Sheng, G. L. Y., H. , Takehisa, O., Ha, L. Z., Zong, Y. H. and Xue, L. C.: Grassland desertification by grazing and the resulting micrometeorological changes in Inner Mongolia, Agricult. For. Meterol., 2000.

Sozzi, R., Georgiadis, T. and Valentini, M.: Introduzione alla turbolenza atmosferica, Pitagora eds., Bologna, 2002.

Stockton, P. H. and Gillette, D. A.: Field measurement of the sheltering effects of vegetation on erodible land surfaces, Land Degrad. Rehabil., 2, 77-85 1990.

Stout, J. E.: Wind erosion within a simple field, Transactions of the American Society of Agricultural Engineering, 33, 1597–1600, 1990.

Stull, R. B.: An Introduction to Boundary Layer Meteorology, Kluwer Academic Publ., Dordrecht, 1988.

Su, Y. Z., Li, Y. L., Cui, J. Y. and Zhao, W. Z.: Influences of continuous grazing and livestock exclusion on soil properties in a degraded sandy grassland, Inner Mongolia, northern China, Catena, 59, 267-278, 2005.

Sun, J., Zhang, M. and Liu, T.: Spatial and temporal characteristics of dust storms in China and its surrounding regions, 1960–1999: relations to source area and climate, J. Geophys. Res., 106(D10), 10325–10333, 2001.

Taylor, J. R.: An introduction to error analysis, University science book Publ., Mill Valley, CA, 1982.

Tegen, I. and Fung, I.: Modeling of mineral dust in the atmopshere: Sources, transport, and optical thickness, J. Geophys. Res., 99D, 22897–22914, 1994.

Tegen, I. and Fung, I.: Contribution to the atmospheric mineral aerosol load from land surface modification, J. Geophys. Res., 100, 18707–18726, 1995.

Tsoar, H., Rasmussen, K. R., Sorensen, M. and Willetts, B. B.: Laboratory studies of flow over dunes, International Workshop of the Physics of Blown Sand, Dept. Theor. Statist., Aarhus University, Denmark, 1985.

Tu, Z., Li, M. and Luo, B.: China national report to implment the United Nation's Convention to Combat Desertification (UNCCD), 2002.

Twomey, S. A.: The Nuclei of Natural Cloud Formation, Part II: The Supersaturation in Natural Clouds and the Variation of Cloud Droplet Concentrations, Geophys. Pure Appl., 43, 227–242, 1959.

Twomey, S. A.: The influence of pollution on the shortwave albedo of clouds, J. Atmos. Sc., 34, 1149–1152, 1977.

Udden, J. A.: Mechanical composition of clastic sediments, Bull Geol. Soc. of Am., 25, 655-744, 1914.

Uncod: United Nations Conference on Desertification, 29 Aug. - 7 Sett. 1977. Round up, plan of action and resolutions. UNCOD-UNEP. New York, EUA, 43 pp., 1978.

Valentini, R., De Angelis, P., Matteucci, G., Monaco, G., Dore, S. and Scarascia Mugnozza, G. E.: Seasonal net carbon dioxide exchange of a beech forest with the atmosphere, Glob. Change Biol., 2, 199-207, 1996.

Van Dijk, A., Moene, A. F. and De Bruin, H. A. R.: The principles of surface flux physics: theory, practice and description of the ECPACK library, Internal Report 2004/1, Meteorology and Air Quality Group, Wageningen University, Wageningen, the Netherlands, 99 pp., 2004.

Wang, H. and Zhou, H.: A simulation study on the eco-environmental effects of 3N Shelterbelt in North China, Global and Planetary Change, 37, 231-246, 2003.

Wang, X., Dong, Z., Zhang, J. and Liu, L.: Modern dust storms in China: an overview, Journal of Arid Environments, 58, 559–574, 2004.

Wentworth, C. K.: The shape of beach pebbles, US Geol. Surv., Prof Pap. 131C, 1922.

Westphal, D. L., Toon, O. B. and Carlson, T. N.: A case study of mobilization and transport of Saharan dust, J. Atmos. Sc., 45, 2145 - 2175, 1988.

White, B. R., Cho, G. H. and Kim, D. S.: A Wind Tunnel Study to Determine Vegetation Cover Required to Suppress Sand Dust Transport at Owens (dry) Lake, California, Great Basin Unified Air Quality Control District, Interagency Agreement no. 9464, 1996.

White, B. R. and Schulz, J. C.: Magnus effect in saltation, J. Fluid Mech., 81, 497-512, 1977.

Wiggs, G. F. S., Livingstone, I., Thomas, D. S. G. and Bullard, J. E.: Effect of Vegetation Removal on Airflow Patterns and Dune Dynamics in the Southwest Kalahari Desert, Land Degrad. Rehabil., 5, 13–24, 1994.

Withby, K. T. and Sverdrup, G. M.: California aerosols: their physical and chemical characteristics, Adv. Environ. Sci. Technol., 8, 477-525, 1980.

Wolf, M. E. and Hidy, G. M.: Aerosols and climate: Anthropogenic emissions and trends for 50 years, J. Geophys. Res. Atmos., 102, 11113−11121, 1997.

Woodruff, N. P. and Siddoway, F. H.: A wind erosion equation, Proc. Soil Sci. Soc. Am., 29, 602-608, 1965.

Xuan, J., Sokolik, I. N., Hao, J., Guo, F., Mao, H. and Yang, G.: Identification and characterization of sources of atmospheric mineral dust in East Asia, Atmos. Environ., 38, 6239-6252, 2004.

Yudine, M. I.: Physical considerations on heavy-particle diffusion, Advances of Geophysics, 6, 185-191, 1959.

Zhang, X., Arimoto, R. and An, Z.: Dust emission from Chinese desert sources linked to variations in atmospheric circulation, J. Geophys. Res., 102(D23), 28041–28047, 1997.

Zhang, X. Y., Gong, S. L., Shen, Z. X., Mei, F. M., Xi, X. X., Liu, L. C., Zhou, Z. J., Wang, D., Wang, Y. Q. and Cheng, Y.: Characterization of soil dust aerosol in China and its transport and distribution during 2001 ACE-Asia: 1. Network observations, J. Geophys. Res., 108, doi:10.1029/2002JD002632, 2003.

Zobeck, T. M., Sterk, G., Funk, R., Rajot, J. L., Stout, J. E. and Van Pelt, R. S.: Measurement and data analysis methods for field-scale wind erosion studies and model validation, Earth Sur. Proc. Land., 28, 1163-1188, 2003.